Wayne State University
DigitalCommons@WayneState

Wayne State University Dissertations

1-1-2012

The Electrical Transport Study Of Graphene Nanoribbons And 2d Materials Beyond Graphene

Ming-Wei Lin
Wayne State University,

Follow this and additional works at: http://digitalcommons.wayne.edu/oa_dissertations

Recommended Citation
Lin, Ming-Wei, "The Electrical Transport Study Of Graphene Nanoribbons And 2d Materials Beyond Graphene" (2012). *Wayne State University Dissertations.* Paper 607.

This Open Access Dissertation is brought to you for free and open access by DigitalCommons@WayneState. It has been accepted for inclusion in Wayne State University Dissertations by an authorized administrator of DigitalCommons@WayneState.

THE ELECTRICAL TRANSPORT STUDY OF GRAPHENE NANORIBBONS AND 2D MATERIALS BEYOND GRAPHENE

by

MING-WEI LIN

DISSERTATION

Submitted to the Graduate School

of Wayne State University,

Detroit, Michigan

in partial fulfillment of requirements

for the degree of

DOCTOR OF PHILOSOPHY

2012

MAJOR: PHYSICS

Approved by:

____
Advisor Date

____

____

____

____

© COPYRIGHT BY

MING-WEI LIN

2012

All Rights Reserved

DEDICATION

“TO MY WIFE AND MY PARENTS”

ACKNOWLEDGEMENTS

I would like to thank Dr. Zhixian Zhou as my advisor for Doctorate research in the past years. We were closely working together during this unforgettable time period in my life. I don't even remember how many nights we were measuring devices until midnight and analyzing data the following mornings. His kindness, patience, and dedication to physics research always make me very impressive. I literally appreciate his help, advice and discussion as a friend in my research work. Thank Dr. Naik for being my committee member and always encouraging me, sharing the research stories with me. Also thank Dr. Nadgorny and Dr. Huang for their precious discussion. I am very grateful to Dr. Mark Cheng for his warmest talking and allowing me to use the facilities in his lab. Thank Dr. J. J. Chang for instructing me and giving me advice in my first year of Ph.D. program at Wayne State.

I particularly have to thank my wife, Kuei-Hui Chang, with all my heart for her sacrifice and companionship during the past two years. She even took on leave from work for accompanying me in my pursuit of Ph.D. degree. Not a word could express my truly gratitude and love to her. I would never complete my research work without her support and understanding. Also thank my two adorable sons, Andrew and Shiny, for staying with me for these two years. I was so happy we could still get together in my journey of graduate studies. Special thanks to my parents who have been always supporting me and giving me the courage to do what I wanted to do. I always thank them for teaching me how to be an educated person since I was little. This work would not have been possibly finished without their fully support. I also thank my parents-in-law for their support and taking care of the kids. I have to thank my sister and my sister-in-law for taking care of my family stuff while I was away, especially my sister's

passion and enthusiasm for caring kids even when she was ill. I am really grateful to her for that. Also thank my brother and brother-in-law for their support all the time.

During graduate research work, I would like to thank many generous people who always helped me out. Thank Dr. Caleb Ryder for kindly lending me textbooks and helpful discussion technically or non-technically. Thank Dr. Mei at CIF for allowing me to use the characterization facilities and helpful technical discussion. Thank Dr. Vaman Naik for teaching me how to use Raman spectrometer and Dr. Nazri for useful discussion regarding Li-ion batteries. Also thank Dr. Alan Sebastian for helping me set up SEM system when moving into Physics building, and Dr. Peter Chen for the help of installing software. Thank Mr. Dhinsa Kulwinder for Raman measurement, Mr. Cheng Ling, Mr. Lezhang Liu, Mr. Qing Lan and Mr. Chongyu Wang for being our lab members and helping me making the samples, and our new lab members Mr. Meeghage Perera, Mr. Bhim Chamlagain and Mr. Hsun-Jen Chuang as well. I appreciate Mr. Xuebin Tan and Mr. Peng Zeng from Dr. Mark Cheng's lab for helping me doing metal deposition and useful discussion. I would never have good devices to measure without their help. Thank Mr. Edward Kramkowski and Mr. Jason Esmacher from Dr. Hoffmann's group for helping me maintain the thermal evaporator, Mr. Bill Funk and Mr. Dan Durisin from ECE for the help in clean room. In addition, thank Mr. Rupam Mukherjee for being my office mate and lots of constructive discussion. Thanks also go to Dr. Pushkal Thapa, Dr. Debabrata Mishra, Mr. Hussein Farhat, Mr. Ehab Abd Elhamid, Mr. Humeshkar Nemala and Mr. Zhe Wu for their technical or non-technical discussion, making the research time more enjoyable.

Besides, I also would like to express sincere gratitude to my best friends, Dr. C. L. Chang and Mr. C. C. Chiang in Taiwan, for their constantly helpful discussion and encouragement. I

really appreciate the sharing of those feelings with each other all these years. Thank Dr. H. D. Yang, Dr. R. Guo and Dr. J. K. Wang from Taiwan for their advice and suggestion. Finally, I would like to have this work dedicated to my second son, Dodle, for his wisdom and worrier's spirits in his short period of life. He gave me the motivation and courage to accomplish the dream, even though this was not an easy job for me after working so many years. He deserves whatever I have done for him and I appreciate him for always reminding me of truly deliberating the meaning and significance of life as a human being.

TABLE OF CONTENTS

Dedication ii

Acknowledgements iii

List of Tables. xi

List of Figures xii

CHAPTER 1 GENERAL INTRODUCTION. 1

1.1 Graphene 1

1.2 Graphene nanoribbon (GNR) 5

1.3 2-D materials beyond graphene. 9

CHAPTER 2 INTRINSIC BANDGAP DETERMINATION AND SIMULATION OF GRAPHENE NANORIBBONS 12

2.1 Introduction. 12

2.2 Experimental details. 13

2.3 Results and discussions. 14

2.3.1 Resistance versus gate voltage 15

2.3.2 Mobility. 16

2.3.3 Bandgap determination 18

2.3.4 Transport gap. 21

2.3.5 Theoretic modeling of bandgap 24

2.3.6 Bandgap from coulomb diamond. 30

2.4 Summary. 31

CHAPTER 3 HIGH ON/OFF RATIO OF GRAPHENE NANORIBBONS . . 32

3.1 Introduction. 32

3.2 Experimental details. 33

3.3 Results and discussions. 35

3.3.1 Observation of large on/off ratio 36

3.3,2 Nano constriction. 38

3.3.3 Thermal and mechanical stability. 40

3.3.4 Theoretic explanation 43

3.3.5 Bandgap validation 46

3.4 Summary. 47

CHAPTER 4 GRAPHENE NANORIBBONS WITH GRAPHITE POWDER 49

4.1 Introduction. 49

4.2 Experimental details 50

4.3 Results and discussions 52

4.3.1 Raman spectroscopy measurement 52

4.3.2 AFM characterization 54

4.3.3 Electrical transport with polymer gate 57

4.4 Summary 63

CHAPTER 5 MONOLAYER MoS_2 TRANSISTORS WITH POLYMER ELECTROLYTE **64**

5.1 Introduction 64

5.2 Monolayer MoS_2 preparation and characterization 65

5.3 Results and discussions 67

5.3.1 Mobility enhancement and possible mechanism 67

5.3.2 MoS_2/metal contact barrier reduction 70

5.3.3 Gate efficiency improvement 74

5.4 Summary 75

CHAPTER 6 AMBIPOLAR FIELD EFFECT TRANSISTORS OF ATOMICALLY THIN MoS_2 WITH IONIC LIQUID **76**

6.1 Introduction 76

6.2 Experimental details 77

6.3 Results and discussions 79

6.3.1 Ambipolar behavior with ionic liquid 79

6.3.2 I_{ds} *vs.* V_{ds} characteristics 82

6.4 Summary 85

CHAPTER 7 CONCLUSION **86**

APPENDIX A **90**

A.1 Sample preparation 90

A.1.1 Graphene nanoribbons 91

A.1.2 MoS_2 monolayer/multilayer 92

A.1.3 CVD grown MoS_2 93

A.2 E-beam lithography 94

A.3 Metal deposition 99

A.4 Problems and issues 101

A.5 Etching and annealing processes 103

APPENDIX B **110**

B.1 AFM characterization 110

B.2 SEM/TEM characterization . . . 111

B.3 Electrical property measurement . . . 120

B.4 Raman spectroscopy measurement . . . 124

B.5 XRD measurement . . . 126

B.6 STM measurement . . . 127

Bibliography . . . 129

Abstract . . . 150

Autobiographical Statement . . . 153

LIST OF TABLES

Table 1.1 The engineered gap size of graphene related materials with different approaches . . . 9

Table A.1 The testing results of 2% concentration HSQ with different doses for line and area. 98

Table A.2 It shows the survived rate around 50% after harsh processes such as etching and annealing in our GNRs devices. 107

LIST OF FIGURES

Figure 1.1 Single layer graphene provides the building block to form 0D fullerence, 1D nanotube and 3D graphite [2]. 2

Figure 1.2 (a) The single layer graphene on Si/SiO_2 substrate through mechanical cleavage using adhesive tape. (b) The ambipolar behavior of single layer graphene indicates the change of Fermi level with the change of gate voltage [2]. 3

Figure 1.3 (a) SEM image shows the GNR devices with different ribbon widths using electron beam lithography with HSQ mask. (b) Conductance of GNRs *vs* gate voltage measured at different temperatures [16] 6

Figure 1.4 The high quality GNRs obtained from unzipping CNTs in solution using sonication and centrifuge to have 10~30 nm wide ribbons [23]. 7

Figure 1.5 The schematic picture of MoS_2 shows the similar structure to graphene [5, 108] . . 10

Figure 2.1 Resistance versus gate voltage for:(a) sample A (lower-disorder), and (b) sample B, measured at various temperatures. The solid lines are the model fitting. The two samples belong to a single GNR with uniform width (W~ 20 nm) and thickness (d ~1.4 nm), and both have the same length L ~ 600 nm. Insets: schematic illustration of a GNR-FET consisting of a suspended GNR (right) and the contact electrodes, and AFM image of a GNR suspended by Au electrodes (left). 15

Figure 2.2 Mobility as a function of temperature for samples A and B. The solid squares and solid circles are the mobility extracted from the model fitting in Fig. 1; the hollow squares are the field effect mobility. The dashed lines are a guide to the eye 17

Figure 2.3 (a) Temperature dependence of the minimum conductance for samples A, B and C. (b) Temperature dependence of the residual carrier density extracted from the model fitting in Figure 2.1 for samples A, B and C. The solid lines are fits to the simple activated behavior 20

Figure 2.4 (a) Conductance versus gate voltage measured at various temperatures for

sample A. (b) *I-V* characteristics measured at different gate voltages and at $T = 4.3$K for sample A. 23

Figure 2.5 (a) Unrolled projection of a (n, m)-CNT of minimum circumference ($|\overrightarrow{OB}|$). The chiral angle θ is determined by the translational vector $\overrightarrow{OA} = (n, m) = (3,2) = 3\overrightarrow{a_1} + 2\overrightarrow{a_2}$. (b) Cross-section of a (3,2)-GNR with ~20nm width. The periodic unit-cell used in the calculation is shown shaded in green. The zoom-in regions show the spatial distribution of spin-up (cyan) and spin-down (red) magnetization. The magnitude of the magnetization is given by the radius size, with the largest radius corresponding to spin magnetization $0.13\mu_B$. 25

Figure 2.6 (a) Electronic band structure, and (b) density of states of a (3,2)-GNR; results in the absence ($U = 0$ eV) and presence ($U = 6.4$ eV) of electron-electron correlation are shown in red and blue, respectively. (c) Calculated bandgaps (black) and maximum spin magnetization (red) for GNRs of (n, m)-type (6,0), (7,1), (5,1), (4,2), (3,2), and (3,3), corresponding to chiral angles θ in ascending order. 27

Figure 2.7 The AC measurement at the temperature 4.2K for GNR reveals the gap size around 100 meV, which is quite consistent with the energy gap calculated from thermal activation energy and theoretical prediction 30

Figure 3.1 AFM images of typical FET devices consisting of a GNR contacted by Au electrodes before (a) and after (b) suspending the GNR. (c) Line profile of the top section of the suspended GNR 35

Figure 3.2 Electrical transport properties of a representative suspended GNR FET device measured at room temperature, where the suspended GNR is 21±3 nm wide, ~1.4 nm thick and ~600 nm long. (a) Transfer characteristic of the device after current annealing to a predefined bias voltage set-point of 2.9 V. (b) I-V characteristics of the device measured at various gate voltages ranging from -15 to 15 V. (c) Transfer characteristic measured after various degrees of current

annealing. (d) Current versus gate voltage (V_g) measured at different bias voltages after the final stage of current annealing (annealed to 3.05 V) 37

Figure 3.3 (a) Temperature dependence of the minimum current at the charge neutrality point measured at V_{ds} = 100 mV for the suspended GNR device in Figure 2. (b)Top part: AFM image of the same GNR in (a); bottom part: another section of the suspended GNR. (c-d) Higher resolution AFM images of the top and bottom sections of the GNR in (b), respectively 40

Figure 3.4 (a-c) Transfer characteristics of a second suspended GNR FET device measured at room temperature; the suspended GNR is 45±3 nm wide, ~1.6 nm thick and ~450 nm long. (a) Transfer characteristic measured after various degrees of annealing. (b) Conductance versus gate voltage measured at room temperature after the final current annealing stage and after different number of thermal cycles; #1, #2, and #3 next to the corresponding G(V_g) curves represent measurements after 1, 2 and 3 thermal cycles, respectively. (c) Gate dependent conductance data in (b) plotted as a function of V_g-$V_{G\text{-}min}$. (d) Room temperature transfer characteristics of a third suspended GNR device (19±3 nm wide, ~1.2 nm thick, and ~300 nm long) measured before (blue solid squires) and after (red solid dots) *ex situ* annealing at 600 ^{O}C for 10 minutes in a vacuum furnace. 42

Figure 3.5 Schematic density of states (DOS) for GNRs. (a) and (c) represent two infinite GNRs of different widths; the corresponding energy bandgaps, observed in the DOS panels (d) and (f), follow the known inverse relation with ribbon width. (b) GNR with a constriction. (e) DOS projected on the region of the constriction; the quantized energy levels of quantum dots QD_1 and QD_2 are shown in red and the states of region GNR_1 are shown in blue. 45

Figure 3.6 Conductance versus gate voltage of the GNR device in Fig. 4d measured at 77,

150, and 295 K 46

Figure 3.7 The coulomb diamond plotted from the DC measurement data of *I-V* curve varying with gate voltage at 200K, leading to the gap size around 700 meV. 47

Figure 4.1 Raman Spectra of solution exfoliated graphene and starting graphite powder. The intensity in each spectrum is normalized to its G-band intensity. 53

Figure 4.2 GNRs produced from sonicating graphite power in DCE solution of PmPV. (a - d) AFM images of GNRs deposited on SiO_2 surface. (b and d) Zoomed images of the marked areas in (a) and (c), respectively: the width of the GNR in (b) is 6 ~8 nm; the width of the GNR in (d) is 23 ~ 26 nm. (e and f) Line profiles of the two GNRs in (b) and (d), respectively. 55

Figure 4.3 Histograms of topographic heights (a) and lengths (b) of over 100 GNRs imaged by AFM on SiO_2 surface: graphene samples narrower than 100 nm with a length to width ratios large than 3 are included. GNRs with length- to-width ratio > 10 are routinely observed. 56

Figure 4.4 Electrical properties of a GNR-FET device. (a) Drain-source current versus drain-source voltage measured at various back-gate voltages. (b) Room Conductance versus back-gate voltage measured at 297 K before and after current annealing. Inset: AFM of the measured GNR-FET devices with two Au electrodes contacting an individual GNR. 58

Figure 4.5 (a) Comparison between back gating without the polymer electrolyte (A), and polymer top gating (B) on the same GNR-FET device. (b) Resistance versus polymer top-gate voltage for the same device. The solid lines in (b) are the model fitting. Inset: optical micrograph of the device with polymer electrolyte gate 61

Figure 5.1 (a) AFM image of a monolayer MoS_2 sample deposited on SiO_2 surface. (b) Line profile of the MoS_2 sample in (a). (c) A Raman spectrum of the same MoS_2 sample 66

Figure 5.2 (a) An optical micrograph of a typical MoS_2 FET device with schematically sketched PE. (b) Conductivity of a representative MoS_2 FET (device A) measured in the Si-back gate configuration before and after adding the PEO/$LiClO_4$ PE. 68

Figure 5.3 (a) Current-voltage characteristics of device A measured at various gate voltages before adding the PEO/$LiClO_4$ PE. (b) Resistance of FET devices fabricated on the same Monolayer MoS_2 (where device A was fabricated) as an function of channel length measured at different back gate voltages. (c) Conductivity as a function of back gate voltage of device B measured at temperatures below and above the freezing temperature of the ions in the PE. (d) Drain-source current versus PE-gate voltage of a MoS_2 FET device (device C) measured at V_{ds} = 100 mV and various back gate voltages. The inset in (a) is the low-bias linear region of (a); and the inset in (b) is the Resistance of device A as a function of back gate voltage after adding the PEO/$LiClO_4$ PE. 72

Figure 5.4 (a) A schematic illustration of the working principle of PE-gated MoS_2 FETs. (b) Drain-source current versus PE-gate voltage of a Monolayer MoS_2 FET device (device B) measured at different drain-source voltages. The inset shows the current-voltage characteristics at different PE gate voltages. 75

Figure 6.1 IL-gated MoS_2 FETs. (a) Optical micrograph of an actual device. The contour of the IL drop covering the MoS_2 channel and the in-plane gate-electrode is marked by white dotted lines. The white scale bar is 20 µm. (b) A schematic illustration of the working principle of IL-gated MoS_2 FETs. 78

Figure 6.2 Transfer characteristics of a bilayer MoS_2 IL-gated FET (W= 1.6 µm and L = 1 µm). (a) Logarithmic plot of drain-source current versus IL-gate voltage measured at various drain-source voltages and T= 230 K. (b) Linear plot of the scaled drain

-source as a function gate voltage for $V_{ds} = 1$ V. 81

Figure 6.3 Comparison of the output characteristics of the same bilayer MoS_2 device in Figure 6.2 before and after depositing IL. (a) I_{ds} vs. V_{ds} with back-gate voltage stepped from 40 to -20 V before depositing the IL drop. (b) I_{ds} vs. V_{ds} by stepping the IL-gate voltage from 1 to 0 V. 84

Figure A.1 The left pictures indicate the chemical solution of GNRs after sonication and centrifuge. On the right are the AFM images illustrating the GNRs on Si/SiO_2 substrate. 92

Figure A.2 (a) The micrograph shows MoS_2 flake is identified by optical microscope with light blue color. (b), (c) AFM scanning further verifies the dimensions of this flake with the thickness ~0.8 nm as monolayer of MoS_2 93

Figure A.3 The configuration of SEM (left) together with NPGS software (right) is used in this work, providing the standard e-beam lithography. 95

Figure A.4 The electrodes pattern after developing process for (a) GNR and (b) MoS_2 under 1K magnification of optical microscope 97

Figure A.5 The setup of metal thermal evaporator includes chamber, diffusion pump and thickness monitor of crystal 99

Figure A.6 The schematic diagrams show the integrated processes with electron beam lithography and metal deposition. (a) Starting the coating of PMMA to lift-off process. (b) The schematic top view shows the metal contacts with GNRs. (c) The actual electrodes picture ready for electrical measurement. 100

Figure A.7 The comparison between clear (left) and unclear (right) patterns produced by electron beam lithography. 102

Figure A.8 AFM images show the performance of electron beam writing before and after

SEM moving. Left image illustrates clear wheel pattern before moving. Middle image indicates the interference wiggling lines after moving, and zoom in image on the right shows obvious interference from the middle image. 103

Figure A.9 (left) Schematic illustration of a GNR-FET consisting of a suspended GNR and the contact electrodes. (right) AFM image shows a GNR suspended by Au electrodes. (down) Line-profile of the AFM image in (right) reveals that the GNR is suspended ~150 nm above the substrate 104

Figure A.10 The pictures show the situation before and after critical point drying. (Left) has clean surface before critical point drying. (Right) has oily material around the electrodes and spots in the center area. 105

Figure A.11 The annealing tool (Ulvac Mila-5000) with program setting was used to remove the impurities and improve the contact resistance after GNRs suspension. 109

Figure B.1 The configuration of AFM (park XE-70) is used in this study, consisting of the software (left) and the optical mocrscope and X-Y scanner as the main body (right). 111

Figure B.2 The SEM (JOEL 7600F)-left and TEM (JOEL 2010)-right were used for characterizing the nano structure and chemical elements of materials. 112

Figure B.3 The SEM images (25K~100K) show the dimension of measured device around 28 nm in width. 113

Figure B.4 The GNRs images were taken from ZEISS-MERLIN with magnification up to 1000K, indicating the width of GNRs ~20 nm. 114

Figure B.5 The large electrodes were fabricated by standard E-beam lithography on the left and Cu grid was attached on the top by dropping some PMMA on the corner shown on the right. 115

Figure B.6 Most of the large electrodes were peeled off on the left, and the pattern in the middle did not transfer to Cu grid completely shown on the right. 116

Figure B.7 The pattern does not completely adhere on PMMA and this approach seems not promising 117

Figure B.8 There were some electrodes suspended and survived using TMAH and HF etching, giving the possibility for TEM observation. 118

Figure B.9 The EDS spectrum shows the composition of TiS_2 film 118

Figure B.10 The HRTEM image (a) and diffraction pattern using SAD (b) for 2-D material TiS_2, showing the lattice constant 3.397Å after calculation 119

Figure B.11 The high vacuum probe station (Lakeshore Crygenics)-(left) and Keithley 4200 semiconductor parameter analyzer-(right) are used in this work. 120

Figure B.12 (a)The gate dependence measurement V_g versus Conductance for GNR, and (b) the gate dependence measurement V_g versus drain current for MoS_2 121

Figure B.13 The AC measurement setup includes lock-in amplifier, current pre-amplifier, volt and current meters together with Labview software to control the system . . 123

Figure B.14 The Raman spectroscopy was used in this study, including Jobin–Yvon Horiba Triax 550 spectrometer, a liquid-nitrogen cooled charge-coupled device (CCD) detector, an Olympus model BX41 microscope with a 100 × objective, and a Modu-Laser (Stellar-Pro-L) Argon-ion laser operating at 514.5 nm. 125

Figure B.15 The characteristic peaks of Raman spetra for (a) MoS_2 and (b) CVD grown graphene, indicating the crystal structure and impurity level for these two materials, respectively. 125

Figure B.16 The XRD spectrum of 2D material TiS_2 using diffractometer indicates the pure TiS_2 characterisitc peaks together with little oxidation of TiO_2 peak. 127

CHAPTER 1

GENERAL INTRODUCTION

1.1 Graphene

Graphene, a single atomic layer of graphite, has attracted a great deal of attention and research in the world since 2004, when Geim and his co-workers at Manchester University obtained this film by mechanical exfoliation of highly oriented pyrolytic graphite [1]. Its two-dimensional (2D) honeycomb lattice with π bond provides the building block to form 0D fullerence, 1D nanotube, and even 3D graphite. Although graphite has been known and used as conducting material for hundreds of years, the mono layer of graphite is now a rising star and draws a myriad of interests for scientists worldwide based on its unusual electronic properties [2, 3, 4]. Back to 70 years ago, scientists considered 2D materials would not exist without 3D base due to thermally unstable until single layer graphene and other 2D free standing materials came out recently [1, 2]. The 2D films grown by molecular beam epitaxy (MBE) are possibly stable on a supporting substrate [2, 4]. Therefore, 2D single layer from exfoliating 3D material offers a simple way to explore new physics and potential applications based on this new finding. Figure 1.1 shows the schematic graph of graphene, indicating the carbon-based family originated from this mono layer 2D material.

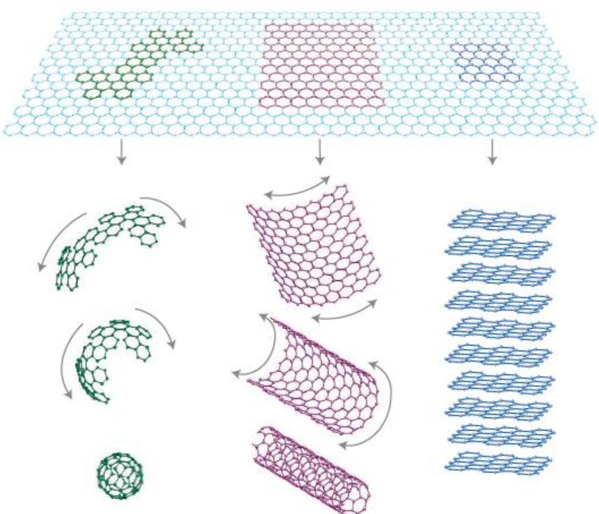

Figure 1.1 Single layer graphene provides the building block to form 0D fullerence, 1D nanotube and 3D graphite [2].

Actually, the flakes including single or multi-layer graphene produced by repeated peeling graphite using adhesive tape first time appeared in the world from Geim's group, which required a great deal of patience. Fortunately, the high quality mono layer graphene would be successfully deposited on Si/SiO_2 with practices through van der Waals attraction force. There are several ways to characterize the thickness of those flakes such as atomic force microscope (AFM), Raman spectroscopy, scanning tunneling microscope (STM), and so on. However, these tools do not have high throughput to identify the graphene quickly. Optical microscope (OM) is still the convenient tool with high efficiency to visualize the spots of single layer of graphene, which Geim's group took the advantage of interference effect of certain thickness of SiO_2 (300 nm) on Si substrate. More than 5% difference of SiO_2 thickness would cause the single layer graphene invisible [2, 4]. Figure 1.2(a) illustrates the single layer of graphene on Si/SiO_2 substrate through mechanical exfoliation using adhesive tape [2].

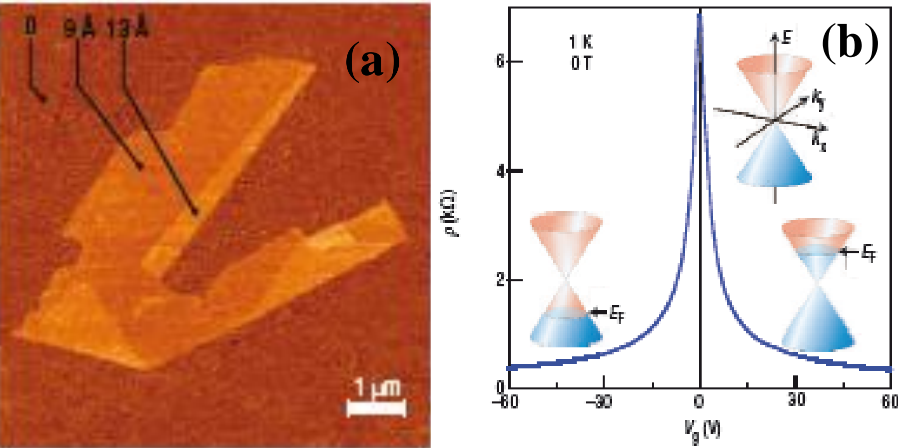

Figure 1.2 (a) The single layer graphene on Si/SiO_2 substrate through mechanical cleavage using adhesive tape. (b) The ambipolar behavior of single layer graphene indicates the change of Fermi level with the change of gate voltage [2].

The studies of graphene have revealed its exceptional electronic properties based on the unique band structure including the observation of ambipolar behavior shown in Figure 1.2(b), high mobility and quantum Hall effect [1, 2]. The charge carriers in graphene can be described as relativistic particles called Dirac fermions by Dirac equation rather than Schrödinger equation for this 2D crystal, providing a way to explore quantum electrodynamics (QED). The mobility of graphene can exceed 15000cm^2 V^{-1} s^{-1} at room temperature with ballistic transport, making potential applications to some certain electronic devices with high speed in need. The graphene also offers a good carrier to probe standard quantum Hall effect or half-integer quantum Hall effect with two spectacular phenomena categorized as minimum quantum conductivity ($4e^2/h$) and strong suppression of quantum interference effects, where e and h are the electron charge and Planck constant, respectively [1, 2].

Other than mechanical exfoliation to make single layer graphene, there are several approaches to improve the throughput and scaling-up for producing the single layer crystal in

recent research. Basically, three techniques have been developed in recent studies including solution-based graphene, epitaxial technique and substrate-based with chemical vapor deposition (CVD) grown graphene [4]. In 2006, Ruoff's group demonstrated the first time to make the single layer graphene using graphite oxide in solution. Yet some of researchers tried to use organic solution to synthesize this 2D single layer crystal. In addition, De Heer at Georgia Institute of Technology pioneered the epitaxial technique using high temperature 1000^0C in high vacuum to detach silicon from silicon carbide (SiC) and left the graphited carbon. While groups from MIT and Korea developed the process of CVD grown graphene on Ni substrates using hydrocarbon gas at high temperature and a single layer of graphene precipitated on the transition metal [4, 54]. Although the electrical performance of graphene using above approaches is not good as that of using mechanical exfoliation, it provides the feasibility to integrate this material with the current semiconductor technology for industrialization.

Therefore, graphene literally exhibits exceptionally high carrier-mobility, offering the tantalizing possibility of all-carbon electronics [63, 131], including spintronics [133, 134], chemical and biological sensing [135-138], nanoelectromechanical systems (NEMS) [139], and energy storage [140]. The electrical transport study of graphene by Geim's group demonstrated that charge carriers in graphene can mimic relativistic particles and their mobility can even reach up to 100,000$cm^2v^{-1}s^{-1}$ at room temperature with less impurity scattering [2]. These unique properties of charge carriers in graphene and their high mobility stimulated numerous studies worldwide [141-149]. The high carrier mobility and planar structure make graphene a promising candidate for many electronic applications. However, the band structure of graphene consists of conduction and valence bands touching each other at the charge neutrality level, leading to a zero

band gap. As an infinite two-dimensional solid, graphene is a zero-gap semiconductor with finite minimum conductivity, which poses a major problem for conventional digital logic applications.

1.2 Graphene Nanoribbon (GNR)

To overcome this bottleneck, many theoretical and experimental studies had focused on engineering an energy gap in graphene because of its advantages mentioned in section 1.1. A tunable band gap up to 250 meV can be induced by a perpendicular electric field in bilayer graphene [11]. A band gap can also be created by strain [12] or by chemical modification of graphene [13]. More generally, a band gap can be created by spatial confinement and edge effects [14]. Louie *et al.* [15] showed theoretically that graphene nanoribbons (GNRs) with pure armchair or zigzag shaped edges always have a nonzero and direct bandgap, the value of which depends on the ribbon crystallographic orientation and edge structure. These remarkable predicted properties of GNRs make them very attractive candidates for key functions in all-carbon devices, but their experimental realization in near-perfect geometries remains elusive. That is also intriguing the motivation to do the research of graphene nanoribbons associated with their intrinsic properties of bandgap and edge effect.

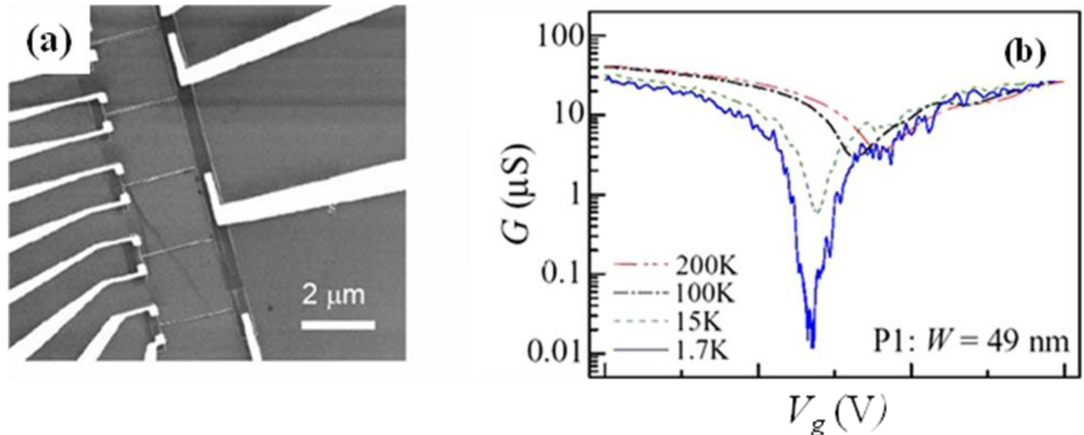

Figure 1.3 (a) SEM image shows the GNR devices with different ribbon widths using electron beam lithography with HSQ mask. (b) Conductance of GNRs *vs* gate voltage measured at different temperatures [16].

Basically, there are two approaches to engineer the gap of graphene with respect to spatial confinement except the methods mentioned above, which are top down (electron beam lithography) and bottom up (chemical solution) ways, respectively. Kim's group at Columbia University has done a series of lithographical patterns using electron beam lithography (EBL) with negative resist, hydrogen silsesquioxane (HSQ) as a mask, showing the gap size of graphene nanoribbons (GNRs) to be as high as 200 meV with ribbon width ~15nm. Figure 1.3 shows the lithographical GNR patterns done by Kim's group with SEM image and minimum conductance versus gate voltage [16]. In lithographically patterned GNRs with varying widths and crystallographic orientations, electrical transport studies established the presence of a width-dependent transport gap [16, 17]. The experimentally determined transport gap increases strongly as the width decreases, consistent with theoretical predictions [15]. However, the observed transport gap is considerably larger than the theoretically predicted bandgap and is independent of the crystallographic direction of GNR edges. Several possible mechanisms have been proposed to explain the transport gap observed in GNR-based field-effect transistors(GNR-

FETs), including re-normalized lateral confinement due to localized edge states [16, 17], percolation driven metal-insulator-transition caused by charged impurities [18], quasi-one-dimensional Anderson localization [19], and Coulomb blockade due to edge-roughness [20]. More recent experimental studies on disordered GNRs further indicate that charge transport in the conduction gap of GNRs is likely dominated by hopping through localized states [21] or isolated charge puddles acting as quantum dots [22]. While surface impurities and edge-roughness are commonly considered as two of the major sources of disorder in GNRs [21, 22], the relative importance of these two sources of disorder in influencing the electronic and transport properties of GNRs is unknown. More recently, significant increase of mobility has been observed in high-quality GNRs with nearly atomically smooth edges partially due to reduced edge scattering [23], but there is still a large discrepancy between the bandgap extracted from these high-quality GNRs and that observed in other reports [24], even though the GNRs were synthesized using a similar approach.

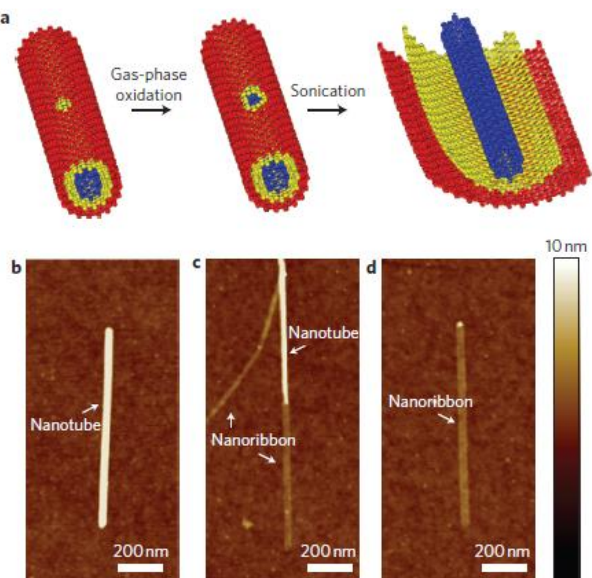

Figure 1.4 The high quality GNRs obtained from unzipping CNTs in solution using sonication and centrifuge to have 10~30 nm wide ribbons [23].

This discrepancy may be attributed to different edge structures, but could also be due to extrinsic conduction through defects and impurity states within the bandgap [11, 25]. What is needed to elucidate the intrinsic electronic properties of GNRs is a systematic and thorough electrical transport study of GNRs with nearly atomically smooth edges and varying degrees of surface impurities. So, the chemically derived GNRs were introduced to have ultrasmooth edge structures [55] instead of rough edges generated by electrons and plasma bombardment. The atomically smooth edges of GNRs derived from unzipping carbon nanotubes (CNTs) in 1,2-dichloroethane (DCE) and poly(m-phenylenevinylene-co 2, 5-diy octocy- p-phenylenevinglene) (PmPV) solution using sonication developed by Dai's group was demonstrated in Figure 1.4 [23]. In this work, most of ultraclean GNRs with smooth edges follow this approach to have 10~50 nm wide ribbons. In order to remove the impurities remained on the surface of GNRs through subsequent processes for making devices, etching has to be conducted using hydrofluoric acid (HF) to get rid of the substrate effect. Besides, thermal annealing and current annealing in vacuum are needed to remove all the impurities and residues, making the GNR devices ultralow disorder for further electrical measurements. The following Table 1.1 is the summary of maximum engineered gap size from graphene related materials by different approaches currently.

Approaches	Max. engineered gap size	Related graphene materials
Strain	Small gap size	Graphene
Applied electrical field	~0.25 eV	Bi-layer graphene
Chemical modification	~3.5 eV	Graphene fluoride
E-beam lithography	~0.35 eV	Graphene, Nanoribbon *w*~15 nm
Sonication in solvent	~0.4 eV	GO, nanoribbon *w*~5 nm
Sonication in solvent	~0.015 eV	MCNT, nanoribbon *w*~14 nm
Chemical with H_2 annealing	~0.05 eV	MCNT, nanoribbon *w*~100 nm

Table 1.1 The engineered gap size of graphene related materials with different approaches.

Most of our GNRs produced in this work follow the method developed by Dai's group and the performance of these ultralow disorder GNR field effect transistors (GNR-FETs) will be described in detail in the following chapter 2-3. In addition, the top gate configuration by adding PEO/$LiClO_4$ polymer electrolyte on the top of GNR devices for improving the mobility will also be shown in chapter 4.

1.3 2-D Materials beyond Graphene

As stated in the previous section, a certain gap size has been opened up for graphene nanoribbons, however, the gap size might not be large enough to practically make the digit electronics realized. While a great deal of processes conducted to engineer the certain gap size for graphene nanoribbons, researchers have started in parallel considering any potential candidates rather than graphene and graphene nanoribbon but similar to them. Actually, there were several candidates combined with transition metals (Mo, W, Ti) and chalcogenide elements (S, Se, Te) studied in the past having the similar structures as graphene, but most of research

focused on the bulk or thin film properties. What about the electrical properties of single layer of these materials? Thanks to the prosperous development of nanosicence and nanotechnology, these 2D materials beyond graphene now have been raising many interests to scientists worldwide.

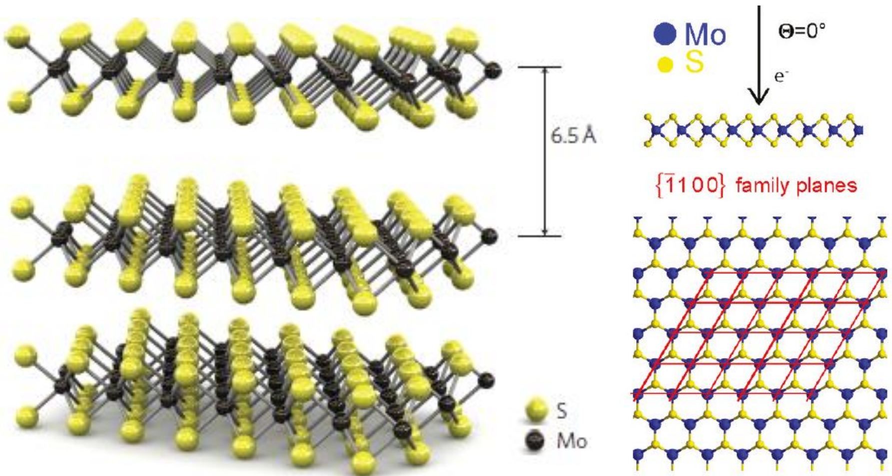

Figure 1.5 The schematic picture of MoS_2 shows the similar structure to graphene [5, 108].

As a semiconducting analogue of graphene, single-layer molybdenum disulfide (MoS_2) has a direct bandgap of ~1.8 eV, which makes it a suitable channel material for low power digital electronics [103]. Similar to graphene, atomic layers of covalently bonded S-Mo-S unites can be extracted from bulk MoS_2 crystals by a mechanical cleavage technique due to relatively weak van der Waals interactions between the layers. The schematic structure of MoS_2 is depicted in Figure 1.5 showing the similarity as graphene [5, 108]. However, the carrier mobility in monolayer and few-layer MoS_2 field-effect transistors (FETs) fabricated on Si/SiO_2 substrates are typically in the range of 0.1 -10 $cm^2V^{-1}s^{-1}$, which is not only orders of magnitude lower than that of graphene but also substantially lower than the phonon-scattering-limited mobility in bulk MoS_2 (which is on the order of 100 $cm^2V^{-1}s^{-1}$) [104-107] Radisavljevic *et al.* have recently

shown that the mobility of monolayer MoS_2 FETs can be improved to at least 200 $cm^2V^{-1}s^{-1}$ by depositing a thin layer of HfO_2 high-κ gate dielectric on top of MoS_2 devices, where the significant mobility enhancement was attributed to the suppression of Coulomb scattering due to the high-κ environment and modification of phonon dispersion [108]. However, it is not clear to what extent the observed mobility increase can be attributed to the screening of charged impurities and phonon dispersion modification. On the one hand, a temperature-dependent electrical transport study of monolayer and few-layer MoS_2 FETs by Ghatak *et al*. suggests that the relatively low mobility in MoS_2 FET devices fabricated on Si/SiO_2 substrate is a channel effect, largely limited by the charge-impurity-induced electron localization [105]. On the other hand, Lee *et al.* showed that the mobility in MoS_2 FETs fabricated on Si/SiO_2 substrate can be largely underestimated due to the Schottky barriers at the MoS_2/metal contacts [109]. Which parameter actually dominating the mobility of MoS_2 single layer is intriguing and needs to be further studied.

In this work, the top gate configuration was also used to improve the mobility of mono layer MoS_2 by placing a drop of PEO/$LiClO_4$ polymer electrolyte on the electrodes of drain-source and gate. The electrical performance of this design will be described in chapter 5. In addition, the performance of the same electrodes design for MoS_2 devices by replacing PE with ionic liquid will be elucidated in chapter 6. Other than MoS_2 crystal, several 2D materials beyond graphene such as titanium disulfide (TiS_2) or molybdenum diselenide ($MoSe_2$) will possibly be intriguing to many scientists for their fundamental physics and potential future applications.

CHAPTER 2

INTRINSIC BANDGAP DETERMINATION AND SIMULATION OF GRAPHENE NANORIBBONS

2.1 Introduction

As an infinite two-dimensional solid, graphene is a zero-gap semiconductor with finite minimum conductivity, which poses a major problem for conventional digital logic applications. To overcome this bottleneck, many theoretical and experimental studies have focused on engineering an energy gap in graphene. In this study, the first variable-temperature electrical-transport study of suspended ultra-low-disorder GNRs with nearly atomically smooth edges is reported. Suspension of the GNRs not only removes the substrate influence but also allows a thorough removal of impurities, including those trapped at the interface between the GNR and the substrate, leading to a substantial increase of the carrier mobility. We observe high mobility values exceeding 3000 $cm^2\ V^{-1}\ s^{-1}$ in GNRs of width~20 nm, the highest mobility value reported to date on GNRs of similar dimensions. Furthermore, we demonstrate that the activation gap extracted from the simple activation behavior of the minimum conductance and residual carrier density at the charge neutrality point approaches the intrinsic bandgap in ultra-low-disorder GNRs. In contrast to the results reported here, in typical transport measurements in GNRs the presence of non-negligible amount of disorder obscures the observation of the intrinsic bandgap. Moreover, the size of the bandgap derived from the transport measurements is in *quantitative* agreement with the results of our complementary tight-binding calculations for a wide range of

chiral angles characterizing the GNR structure, supporting our proposed explanation, namely that the underlying electronic origin of bandgap enhancement is the magnetic nature of electronic states associated with zigzag edges.

2.2 Experimental details

The GNRs were produced by sonicating mildly-oxidized multiwall carbon nanotubes (MWNT) in a 1,2-dichloroethane (DCE) solution of poly(m-phenylenevinylene-co 2, 5-diy octocy- p-phenylenevinglene) (PmPV), where the PmPV is used as a surfactant to stabilize the unzipped GNRs in solution [23]. The solution was then centrifuged at 15000 rpm (Fisher Scientific Marathon 26kmr centrifuge) for 1 hr to remove aggregates and some of the remaining MWNTs, and a supernatant containing nanoribbons and remaining MWCTs was obtained. Next, the GNR samples from the supernatant were deposited on degenerately doped Si subtracts with 290 nm of thermal oxide. Non-contact mode AFM (Park System XE-70) measurements were used to locate individual GNRs with respect to the prefabricated Au alignment marks and to characterize their thickness, width and length. The GNRs produced from this method mostly consist of 1-3 layers. To determine the width, we have taken into account the AFM tip dilation effect (leading to artificial width increase) based on the estimated tip radius provided by the tip manufacturer.

FET devices consisting of individual GNRs are fabricated on Si substrates with 290 nm of thermal oxide using standard electron beam lithography and thermal deposition of 0.5 nm of Cr and 50 nm of Au, where the Si substrate is used as a back gate. Suspension of the GNRs in FET devices is achieved by placing a small drop of 1:6 buffered hydrofluoric acid (HF) on top of

the GNR device for 90 s to etch way approximately 150 nm of the SiO_2 underneath the ribbons [26, 27]. The devices are annealed in vacuum at 600°C for 10 minutes to clean the suspended ribbons and improve the electrical contacts before transferred to a Lakeshore Cryogenics vacuum probe station for further removing adsorbed impurities by current annealing and subsequent transport measurements in high vacuum (~10^{-6} torr). The residual impurities on GNRs are gradually removed by repeatedly passing a large current through the ribbon; the final amount of impurities of the GNRs depends both on initial amount and the degree of current annealing.

A semiconductor parameter analyzer (Keithley 4200) was used to apply the annealing current and to measure the device characteristics for $4.3 < T < 300$ K. We repeatedly applied gradually increasing annealing current and subsequently carry out the electrical measurements *in situ* after every consecutive step. The degenerately doped Si substrate was used as a back gate. To avoid possible collapsing of the suspended GNRs, the back-gate voltage V_g was limited to the range $-15\text{ V} < V_g < +15\text{ V}$ during the electrical measurements.

2.3 Results and discussions

We have fabricated over 20 suspended GNR-FET devices from GNRs synthesized by unzipping high quality multiwall carbon nanotubes [23]. A schematic diagram and an atomic force microscopy (AFM) image of a typical suspended GNR device are shown in the right and left insets of Figure 2.1, respectively. As most of the devices were eventually damaged during the *in situ* current annealing (likely caused by structural reconstruction at the defect sites), we report detailed electrical transport results on three high quality samples (samples A, C and D)

characterized by extremely low disorder and compare them with those of a sample that contains a non-negligible amount of defects (sample B).

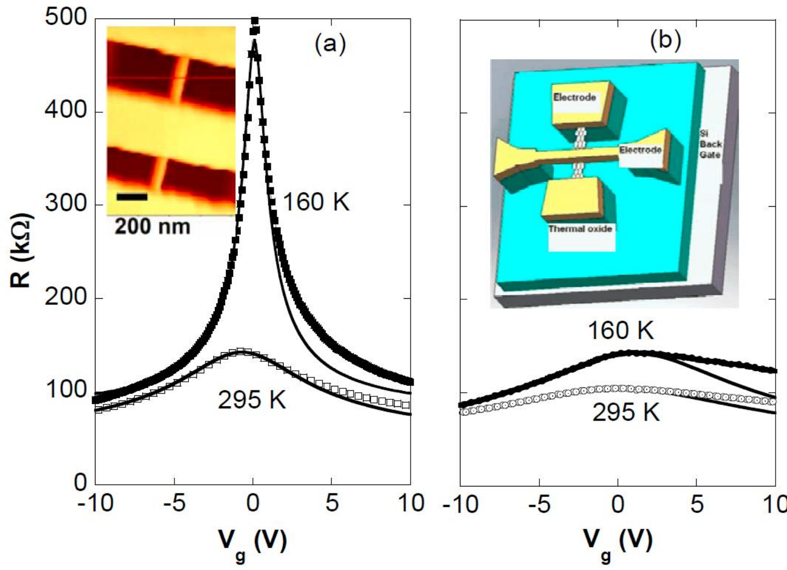

Figure 2.1 Resistance versus gate voltage for: (a) sample A (lower-disorder), and (b) sample B, measured at various temperatures. The solid lines are the model fitting. The two samples belong to a single GNR with uniform width (*W*~ 20 nm) and thickness (*d* ~1.4 nm), and both have the same length *L* ~ 600 nm. Insets: schematic illustration of a GNR-FET consisting of a suspended GNR (right) and the contact electrodes, and AFM image of a GNR suspended by Au electrodes (left).

2.3.1 Resistance versus gate voltage

In Figure 2.1, we show the resistance (*R*) as a function of gate voltage (V_g) at different temperatures for two devices fabricated from a single uniform GNR. The GNR channels in these two devices have similar length (~600 nm), and nearly identical width (~20 nm) and thickness (1.4 nm corresponding to about 2layers [23]) as determined by AFM before suspension [28]. Although both devices show characteristic ambipolar behavior arising from the electron-hole symmetry of graphene, they also exhibit remarkable differences. First, the resistance peaks at the charge neutrality point (CNP) in sample A are substantially sharper [Figure 2.1(a)] than in

sample B [Figure 2.1(b)]. The full-width at half-maximum (FWHM) for sample A is more than an order of magnitude smaller than that for sample B at 160 K. Second, the maximum resistance at the CNP in sample A increases more rapidly with decreasing temperature than in sample B. These differences can be attributed to lower degree of disorder in sample A than in sample B. Defects, such as adsorbed charged impurities and structural imperfection, are expected to generate random potential fluctuations in the GNRs, which induce electron-hole puddles close to the CNP [26, 27]. As a result, the effect of gate voltage near the CNP is largely limited to the redistribution of charge carriers between electrons and holes without changing the overall carrier density. Therefore, a higher tunability of charge carriers near the CNP (and hence a much sharper resistance peak) is expected in samples with lower disorder. Similarly, the effect of thermally excited electron-hole pairs is also significantly enhanced with lower disorder, leading to a stronger temperature dependence of the maximum resistance.

2.3.2 Mobility

We next focus on the influence of disorder on the carrier mobility and bandgap of GNRs. To extract accurate values for these quantities, we subtract the contact resistance from the total resistance using the following model to fit the $R(V_g)$ data:

$$R_{total} = R_{contact} + R_{channel} = R_{contact} + \frac{L/W}{ne\mu} \quad (2.1)$$

Here, $R_{contact}$ and $R_{channel}$ are the metal/GNR contact resistance and GNR channel resistance, respectively [29]; L and W are the channel length and width, respectively; μ is the carrier mobility, and the carrier concentration n, can in turn be determined by the expression,

$$n = \sqrt{n_o^2 + \left[\frac{C_g(V_g - V_{CNP})}{e}\right]^2}, \tag{2.2}$$

with n_o being the residual carrier concentration at the maximum resistance, C_g the back-gate capacitance (estimated to be ~ 3×10^{-8} F/cm^2 based on the capacitance of GNR-FET devices with similar ribbon width and taking into account the reduced dielectric constant due to the removal of ~150 nm of thermal oxide underneath the ribbon [30, 31]), and V_{CNP} is the gate voltage at the charge neutrality point [29, 32]. As shown in Figure 2.1, this model fits our experimental data reasonably well, especially in the hole-branch (V_g<V_{CNP}). The slightly lower conductance and minor deviation from the fitting at the electron side is likely due to the residual surface impurities and/or electrode metal doping [27, 30, 33]. From the fitting, a contact resistance of 30 ~ 70 kΩ is extracted, which is comparable to the value determined by 4-terminal measurements of similar GNRs devices (data not shown). Although this model assumes a gate-independent contact resistance, we believe this is a reasonable assumption for our devices given the nearly ohmic contact (except at low temperatures and near the CNP) and reasonably good fit of the data to the model, which is also consistent with the findings of Russo *et al.* [34].

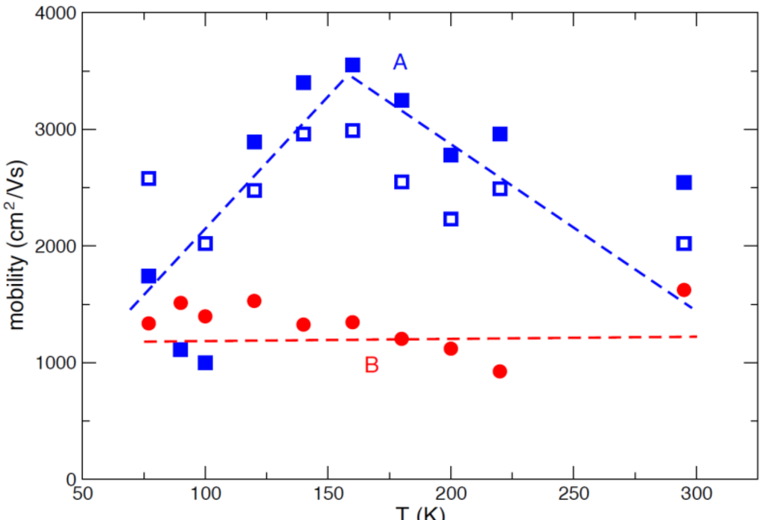

Figure 2.2 Mobility as a function of temperature for samples A and B. The solid squares and solid circles are the mobility extracted from the model fitting in Fig. 1; the hollow squares are the field effect mobility. The dashed lines are a guide to the eye.

Figure 2.2 shows the mobility values derived from the fit as a function of temperature for samples A and B. The mobility of sample B has relatively weak temperature dependence and reaches ~ 1500 $cm^2 V^{-1} s^{-1}$, in excellent agreement with that derived from substrate-supported GNRs synthesized using the same method [23]. Remarkably, the mobility of sample A increases from ~ 2000 $cm^2 V^{-1} s^{-1}$ to over 3000 $cm^2 V^{-1} s^{-1}$ as the temperature is lowered from 295 K to 150 K, suggesting that the mobility in this temperature range is largely limited by acoustic phonon scattering [35]. The peak mobility in sample A is the highest reported to date for GNRs of comparable widths [23], which can be attributed to the nearly atomically smooth edges and extremely low disorder. Below 150K, the mobility decreases with decreasing temperature, suggesting that the presence of a small amount of remaining disorder can play an increasingly important role at low carrier density (see detailed discussion below). Equally high mobility is also observed in sample C (data not shown). From the transfer characteristics, the field effect mobility of sample A in the hole region can be estimated as:

$$\mu = [\Delta G \times (L/W)]/(C_g \Delta V_g), \qquad (2.3)$$

where G is the low-bias conductance of the sample [36] and the other parameters are defined in Eqs.(2.1) and (2.2). The field-effect hole mobility as a function of temperature for sample A is shown as “hollow squares” in Figure 2.2, in reasonable agreement with the mobility values derived from the other method.

2.3.3 Bandgap determination

In an ideal intrinsic semiconductor without impurities, the conductance at the CNP, G_{min} is expected to be dominated by thermally activated carriers and to vary with temperature as $G_{\min} \propto \exp(-E_g/2k_BT)$, where k_B is the Boltzmann constant and E_g is the activation energy for electron excitation that corresponds to the bandgap. However, other mechanisms such as one-dimensional (1D) nearest neighbor hoping (NNH) through localized states in disordered GNRs may also lead to simple activated behavior of G_{min} [21]. To confirm that the activation energy derived from the temperature dependence of G_{min} is indeed the intrinsic bandgap, it is necessary to show the same simple activation temperature dependence of the minimum carrier density (n_0) at the CNP (to first order approximation): $n_0 \propto \exp(-E_g/2k_BT)$. As shown in the Arrhenius plots in Figure 2.3 (a) and (b), the G_{min} and n_0 data from samples A and C (the latter being yet another low-disorder sample with W ~37 nm, d ~ 2 nm, and L ~ 700 nm) fit the simple activation model fairly well with a consistent activation energy gap of E_g (A) = ~ 99 meV (from G_{min}) and ~106 meV (from n_0) for sample A, and $E_g(C)$= ~ 55 meV (from n_0) and ~ 58 meV (from G_{min}) for sample C, respectively. Simple activation behavior is also observed in the residual carrier density of sample D (W ~ 23 nm and d ~ 1.6 nm), yielding a gap of 96 meV (data not shown). Furthermore, comparison of the E_g values of samples A, C, and D demonstrates that the bandgap in our ultra-low-disorder samples is approximately inversely proportional to the ribbon width, consistent with theoretical predictions [15]. These consistent results on multiple ultra-low-disorder GNR-FET devices strongly suggest that the intrinsic bandgap is approached.

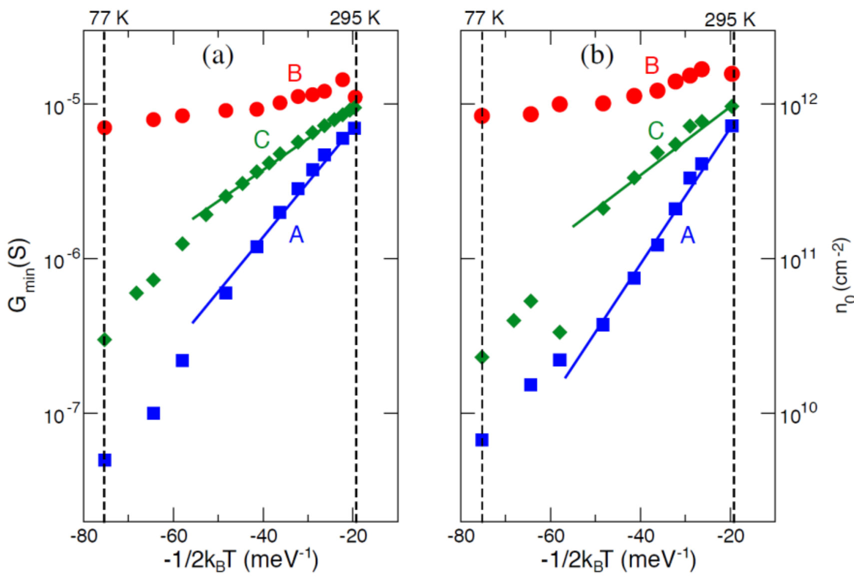

Figure 2.3 (a) Temperature dependence of the minimum conductance for samples A, B and C. (b) Temperature dependence of the residual carrier density extracted from the model fitting in Figure 2.1 for samples A, B and C. The solid lines are fits to the simple activated behavior.

On the other hand, $G_{\min}$ and n_0 in sample B exhibit a much weaker temperature dependence than in samples A or C; forcing the simple activation law fit through the data of sample B yields a much smaller activation energy and corresponding bandgap of $E_g \sim 10$ meV from both the $G_{\min}$ and n_0 data. The large discrepancy between samples A and B is quite puzzling, since they are simply two different regions of the same GNR with highly uniform width and thickness and likely having the same nominal edge structure. The primary known difference between them is that sample A has lower disorder than sample B due to the spatial variation of disorder (such as remaining adsorbed impurities and structural defects which could be inherent in the original carbon nanotubes and/or introduced during the conversion from carbon nanotubes to GNRs). Given the small dimensions of the devices, even a small amount of disorder may play a significant role in their transport properties. Additionally, Au-contact doping may also vary from device to device. However, electrode doping is unlikely to be the

dominant mechanism given that samples A and B not only have nominally identical contact structure and layout but also share a common electrode. Therefore, the weaker temperature dependence of G_{min} and n_0 observed in sample B is likely to be due to extrinsic conduction through defects and carrier doping from charged impurities, similar to the bilayer graphene [11, 25]. An alternative explanation is that the presence of disorder weakens the on-site Coulomb interaction, which is largely responsible for the opening of a gap in the band structure of GNRs with zigzag edges [37]. Zigzag edges have indeed been observed by scanning tunneling microscopy (STM) in GNRs synthesized using the same method [38]; the smaller values of the bandgap found in these studies can be attributed to the reduced on-site Coulomb repulsion due to screening from the gold substrate [38]. It is also worth noting that the data for samples A, C (Figure 2.3) and D (data not shown) start to deviate from the simple activation behavior below 100 K and the fit eventually breaks down below 77 K. The break-down of the simple activated behavior at low temperatures can be attributed to the extremely low residual carrier density: the value $n_0 \sim 7\times10^9$ cm^{-2} at 77 K observed in sample A corresponds to only “one electron” in the device channel. Therefore, the residual carrier density (thus also the minimum conductivity) below 77 K is no longer determined by thermal activation.

2.3.4 Transport gap

In order to further verify that the simple activation gap observed in our ultraclean GNRs is the intrinsic bandgap (due to the extended states carrying current via thermal activation across the intrinsic bandgap), we compare the activation gap energy with the energy associated with the

transport gap (ΔV_g). The transport gap is correlated to an energy gap in the single particle spectrum given by:

$$\Delta_m = \frac{h}{2\pi} v_F \sqrt{\frac{2\pi C_g \Delta V_g}{e}}, \tag{2.4}$$

where $v_F = 10^6$ m/s is the Fermi velocity of graphene and C_g is the capacitive coupling of the GNR to the back gate. In disordered GNRs, where the electrical transport is dominated by the hopping between localized states, Δ_m is expected to be substantially larger than E_g [21]. In contrast, in highly ordered GNRs with very low impurity concentration Δ_m should be comparable to the intrinsic bandgap [24]. ΔV_g in this study is defined as the width of the back gate voltage region determined by a sudden increase of the slop in the $G(V_g)$ curve close to the CNP. As shown in Figure 2.4(a), the $G(V_g)$ curve for sample A measured at 30 K yields a ΔV_g ~ 1.6 V and hence Δ_m ~ 90meV, in reasonable agreement with the values of E_g obtained from G_{min} and n_0, indicating that the transport gap is associated with the large intrinsic bandgap. The linear dependence of G on gate voltage V_g at high temperatures [Figure 2.4 (a), where the contact resistance is excluded] suggest that the field-effect mobility remains nearly constant as the carrier density changes and that the charge transport is limited by long-range scattering [39].

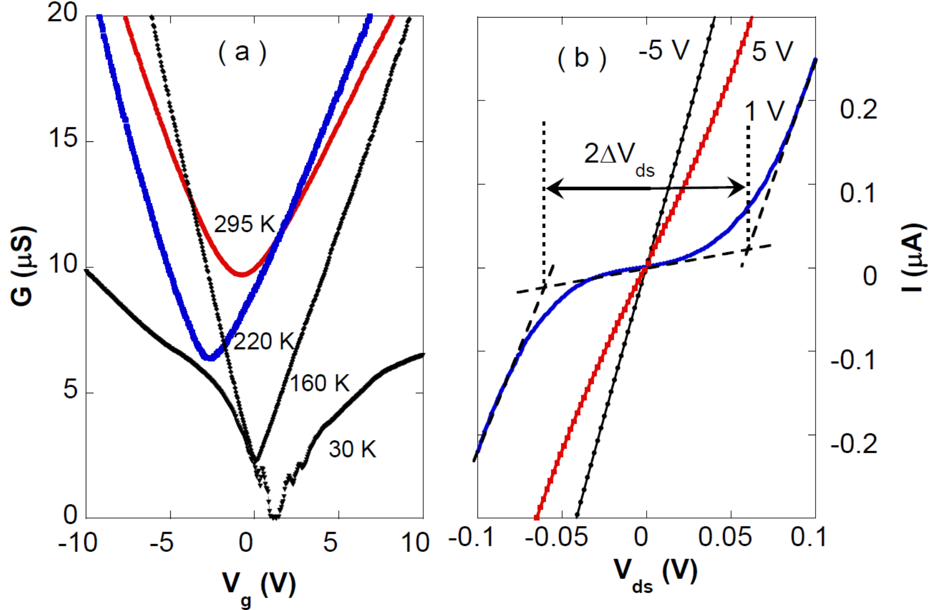

Figure 2.4 (a) Conductance versus gate voltage measured at various temperatures for sample A. (b) *I*-*V* characteristics measured at different gate voltages and at $T = 4.3$K for sample A.

The transport gap can be alternatively probed by measuring the current-voltage (*I*-*V*) characteristics at various gate voltages. Figure 2.4(b) shows representative *I*-*V* curves of sample A measured at 4.3 K. At gate voltages away from the CNP, the *I*-*V* curves are essentially linear. Near the CNP (V_g = 1V), however, the *I*-*V* characteristic becomes strongly non-linear when the chemical potential of the GNR is within the transport gap. A nonlinear gap can be defined by the distances between two interception points made by fitting straight lines to both the low conductance region at low bias voltage and the high conductance region at high bias voltage, as shown in Figure 2.4(b). The nonlinear gap ($e\Delta V_{ds}$) for sample A is approximately 60 meV, slightly smaller than the activation gap or the energy associated with the transport gap, which can be attributed to the fact that the gate voltage at which the nonlinear gap is measured slightly differs from the exact CNP. Unlike in highly disordered GNRs, where the presence of localized

states and the formation of isolated charge puddles (which act as quantum dots) complicates the interpretation of the nonlinear gap in their *I-V* characteristics [21, 22], the nonlinear gap in our low-disorder GNRs may be approximated as the intrinsic bandgap for $V_g = V_{CNP}$ [16].

2.3.5 Theoretic modeling of bandgap

In order to elucidate the underlying electronic origin of the high bandgap value in ultra-low-disorder GNRs, we carried out tight-binding (TB) calculations in model GNRs of comparable width (~20nm). Ultraclean GNRs with ultrasmooth edges are expected to be highly crystallographic and the measured intrinsic bandgap should be comparable to the theoretical values that assume periodicity. Because of the lack of information on the chirality (n, m) of our ribbons, we calculated GNRs of a wide range of chiral angles(θ), varied from $\theta = 0°$ (zigzag GNR) to $\theta = 30°$ (armchair GNR) as shown in Figure 2.5(a); GNRs with intermediate chirality exhibit mixed edges (zigzag/armchair) with dominant zigzag or armchair character as $\theta \to 0°$ or $\theta \to 30°$, respectively.

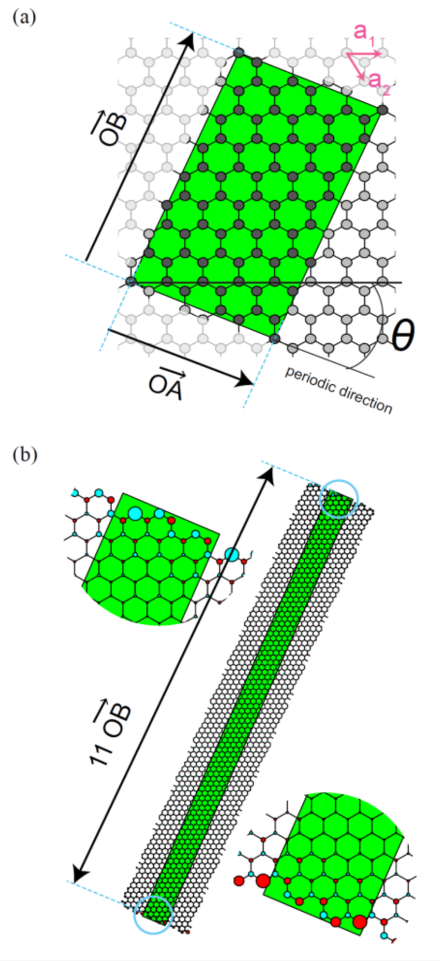

Figure 2.5 (a) Unrolled projection of a (n,m)-CNT of minimum circumference ($|\overrightarrow{OB}|$). The chiral angle θ is determined by the translational vector $\overrightarrow{OA} = (n,m) = (3,2) = 3\overrightarrow{a_1} + 2\overrightarrow{a_2}$. (b) Cross-section of a (3,2)-GNR with ~20nm width. The periodic unit-cell used in the calculation is shown shaded in green. The zoom-in regions show the spatial distribution of spin-up (cyan) and spin-down (red) magnetization. The magnitude of the magnetization is given by the radius size, with the largest radius corresponding to spin magnetization $0.13\mu_B$.

As seen in Figure 2.5(a), the GNRs structures used in the calculations are derived from unzipping a CNT along the chiral unit-cell translational vector $\overrightarrow{OA} = (n,m)$ that determines the chiral angle θ. The translational vector in turn restricts the width of the ribbons to discrete values that are the multiples of $|\overrightarrow{OB}|$, which is the minimum circumference of a (n,m)-type CNT. The electronic-structure calculations employ the single-band Hubbard model:

$$\hat{H} = -t\sum_{\langle i,j\rangle,\sigma}\left(\hat{c}_{i\sigma}^{\dagger}\hat{c}_{j\sigma} + h.c.\right) + U\sum_{i}\hat{n}_{i\uparrow}\hat{n}_{i\downarrow} \qquad (2.5)$$

treated within the mean-field approximation. Here, t is the hopping matrix element between nearest-neighbor sites *i* and *j*, $\hat{n}_{i\sigma} = \hat{c}_{i\sigma}^{\dagger}\hat{c}_{i\sigma}$ is the number operator on atom *i* with spin $\sigma = \uparrow, \downarrow$, and *U* is the on-site Coulomb interaction. The choice of the t and *U* parameters is crucial to making comparisons between experimental and theoretical values for the bandgap which is proportional to $({}^{U}/_{t})$. Furthermore, the values of *U* and t depend on the choice of the exchange-correlation functional used in the density functional theory (DFT) calculations. We have used the *ab-initio* parameters (t= 3.2 eV and *U* = 2t) reported by Pisani*et al.* [40], derived from fitting the antiferromagnetic band structure of zigzag GNRs using the fully-nonlocal "hybrid" functional (B3LYP) of DFT calculations, which includes a contribution of Hartree-Fock exchange that compensates for the electronic self-interaction. Previous studies have shown that B3LYP is better suited than local, nonlocal or even other hybrid functionals to account for molecular magnetism [41]. These values are somewhat larger than those commonly employed in literature [42, 43], which are derived from DFT calculations employing local or nonlocal functionals. These values are also more appropriate to our suspended GNR samples that interact neither with a metallic substrate [38], which reduces *U* through screening with the conduction electrons, nor with oxide substrates (SiO_2), which have much higher dielectric constant than air.

In the absence of electron-electron correlations (*U* = 0 eV in Eq. (2.5)) the systems are non-magnetic. Interestingly, we find that the carbon atoms in the zigzag chains in the mixed-edge GNRs (even a single one per unit-cell in the limit when$\theta \longrightarrow 30°$) introduce non-bonding states whose origin is topological frustration [44]. These non-bonding states form dispersionless "flat" bands at the Fermi level and render the systems gapless or metallic. For *U* =0 eV, the band

structure and density of states for all our systems follow the same pattern as for the (n,m)= (4,2) GNR shown in Figures 2.6(a) and 2.6(b) (red curves). This is analogous to the predicted presence of non-bonding states in randomly shaped 0-D graphene dots that contain combined zigzag/armchair edges [45]. Therefore, only "pure" armchair ribbons could sustain an energy bandgap which is not of magnetic origin. When electron-electron correlations are introduced (U> 0eV) local magnetism arises along the edges of the ribbon, as seen in Figure 2.5(b). Noticeably, the magnetization is predominantly higher on the zigzag sites than on armchair sites, where magnetism is quenched; this trend for mixed-edge GNRs has been corroborated using ab-initio calculations (with the local-density-approximation (LDA)) [46]. Also, the flat bands split, opening an energy gap at the Fermi level (blue curves in Figure 2.6).

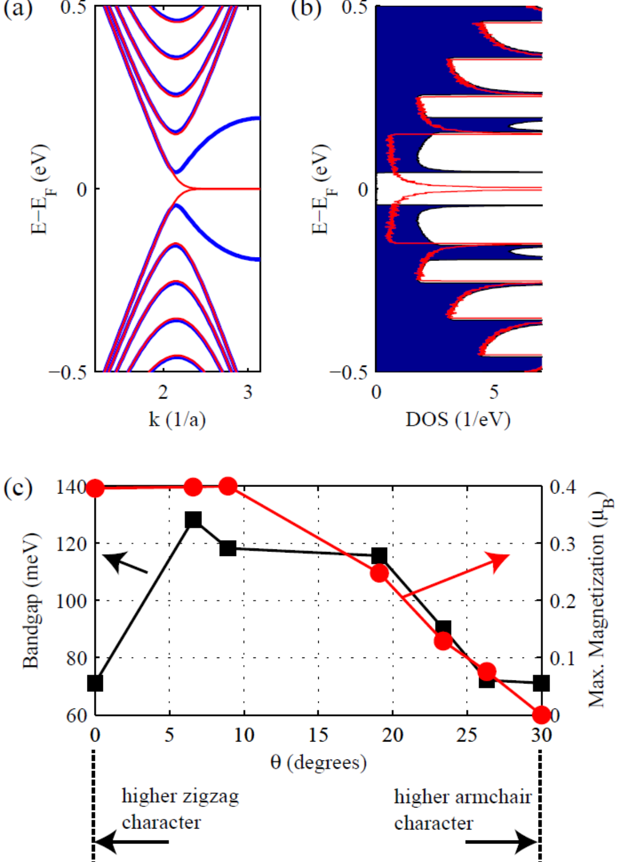

Figure 2.6 (a) Electronic band structure, and (b) density of states of a (3,2)-GNR; results in the absence (U = 0 eV) and presence (U = 6.4 eV) of electron-electron correlation are shown in red and blue, respectively. (c) Calculated bandgaps (black) and maximum spin magnetization (red) for GNRs of (n, m)-type (6,0), (7,1), (5,1), (4,2), (3,2), and (3,3), corresponding to chiral angles θ in ascending order.

Figure 2.6(c) shows the energy bandgap and maximum spin magnetization for~20nm-wide GNRs with crystallographic orientations given by θ= 0°, 6.59°, 8.95°, 19.11°, 23.41°, 30°, corresponding to (n, m) = (6,0), (7,1), (5,1), (4,2), (3,2), (3,3), respectively. Magnetic pure zigzag and non-magnetic pure armchair GNRs exhibit similar bandgaps of ~71meV. Interestingly, for all the mixed-edge GNRs (with $0° < \theta < 30°$), the bandgap varies between 71meV and 128 meV, in agreement with the experimentally determined bandgap for sample A, suggesting that the origin of the bandgap for mixed-edge GNRs is associated with the magnetism of the zigzag edges. The increase of bandgap in the zigzag-rich region ($\theta \sim 0°$) of Figure 2.6(c) is consistent with an increasing insulating character caused by gradually breaking the zigzag π-network as the crystallographic orientation departs from$\theta = 0°$. As the chirality approaches the armchair-rich region ($\theta \sim 30°$) the spin magnetization quenches monotonically and the splitting induced by the second term of Eq. (2.5) becomes weaker, leading to a decreasing bandgap.

To compare our experimental and tight-binding results with existing theoretical results, bandgap values from *ab initio* DFT calculations of narrow spin-polarized zigzag ribbons reported in the literature are extrapolated, when possible, to the widths of our samples. For instance, LDA predicts a gap of 44 meV [15, 47] for a ~20 nm wide GNR. Furthermore, the accurate screened-exchanged hybrid functional (s-X LDA), which corrects the lack of nonlocal exchange responsible for the typical 50-75% gap underestimations of LDA for narrow GNRs [48], predicts a gap of 116 meV for a ~20 nm wide GNR, in good agreement with our experiments. Moreover,

the highly accurate quasiparticle GW method yields a larger bandgap for zigzag GNRs compared to the values employing the s-X LDA [48, 49], although a direct extrapolation is lacking. These *ab initio* results corroborate our relatively large experimental bandgap.

For the armchair case, extrapolated LDA results predict a maximum bandgap of 80 meV [49] while the screened-exchange hybrid functional {Heyd-Scuseria-Ernzerhof (HSE) [50]} and GW predict gaps of 14 meV [51] and 22 meV [49], respectively, for a ~20 nm wide GNR. Although these values are smaller than our armchair tight-binding results, they support our primary hypothesis that a measured bandgap of ~ 100 meV for a ~20 nm wide GNR is likely due to the presence of spin-polarized zigzag edges and not due to the semiconducting nature (finite gap) of armchair edges.

Our calculations were performed on single layer GNRs while the GNRs used in our experiment may consist of more than one layer. Nevertheless, the experimental and the theoretical bandgaps are still in good quantitative agreement. A likely scenario is that the experimentally derived bandgap is an average of the contributions from individual layers that have comparable bandgap values, which can be attributed to the combined effects of the relatively weak interlayer-interactions between non-AB (Bernal)-stacked layers [52] and the weak chirality dependence of the bandgap. Furthermore, moderate tensile strain may be present in our suspended GRNs as indicated by the lack of sagging (Figure 2.1 inset), which is expected to slightly modify the size of the bandgap [53]. For the case of zigzag GNRs, a moderate strain leads to slight increase of the edge spin polarization, thus increasing the bandgap [53]. Therefore, the bandgap in our suspended chiral GNRs may be further enhanced by tensile strain.

2.3.6 Bandgap from coulomb diamond

In order to further verify the bandgap of our ultralow disorder GNRs calculated from different methods described in the previous sections to be the intrinsic bandgap, the coulomb diamond measurement [16] was carried out using AC configuration to directly obtain the bandgap at 4.2K. Figure 2.7 shows the coulomb diamond with comparable GNR width~ 20nm, indicating the gap size around 100 meV from extrapolating the lines on four edges, which is quite consistent with the theoretical prediction and the value calculated from thermal activation energy of ultralow disorder GNRs. The graph does not seem as symmetric as a diamond, possibly caused by the asymmetry of quantum dot or remaining impurities on the GNR.

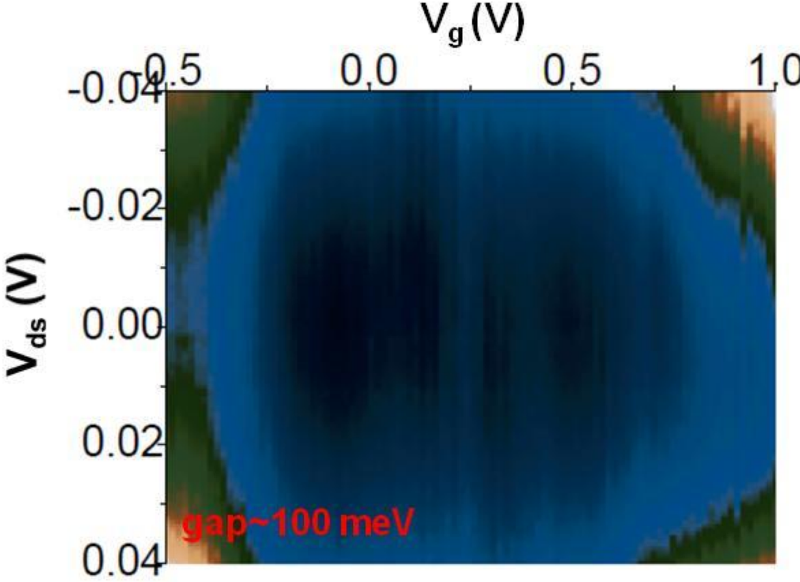

Figure 2.7 The AC measurement at the temperature 4.2K for GNR reveals the gap size around 100 meV, which is quite consistent with the energy gap calculated from thermal activation energy and theoretical prediction.

2.4 Summary

We have fabricated GNRs with very low disorder by: (i) unzipping high quality CNTs with very low concentration of structural defects known to produce GNRs with nearly atomically smooth edges [23]; (ii) suspending the GNR from the substrate; and (iii) removing the remaining impurities by *in situ* current annealing. These ultraclean and ultra-smooth-edged GNRs not only exhibit high mobility exceeding 3000 $cm^2 V^{-1} s^{-1}$, but also reveal the intrinsic electronic structure (bandgap) of GNRs. The good *quantitative* agreement between the experiment and theory suggests that the underlying mechanism responsible for the large bandgap in ultraclean suspended GNRs is most likely the magnetism associated with the zigzag edge components, which is strongly enhanced by the absence of either metallic or insulating substrates. The possible strain in the suspended GNRs may further augment the bandgap. Additional studies are underway to explore the tuning of the electronic and magnetic properties of such ultraclean GNRs via external electric and magnetic fields.

CHAPTER 3

HIGH ON/OFF RATIO GRAPHENE NANORIBBONS

3.1 Introduction

As mentioned in the chapter 2, graphene exhibits exceptionally high carrier-mobility and high stiffness properties providing the possibility of carbon-based electronics [6]. However, graphene is a zero gap semiconductor with finite minimum conductivity, which poses a major problem for mainstream logic applications. One way to circumvent this problem is to slice graphene into nanometer-scale ribbons, where a band gap can be created by spatial confinement and edge-effects [15]. Electron-beam lithography was first used to pattern graphene nanoribbons (GNR) down to width <~20 nm for field-effect transistor (FET) applications; and a width-dependent transport gap was observed in these devices [16-17, 54]. However, GNRs fabricated by electron beam lithography and subsequent oxygen plasma etching have relatively rough edges (on the order of few nanometers) limited by the resolution of electron beam lithography, which may degrade their electrical properties. Subsequently, several alternative methods have been developed to produce GNRs, including chemical sonication of exfoliated expandable graphite or chemically derived graphene sheets [55, 56], controlled nano-cutting with either metal particles or scanning probe tips [57-59], etching with physical masks (e.g. nanowires) [60], and longitudinal unzipping of multiwall carbon nanotubes [23, 61-62]. Particularly, sub-10 nm GNRs with ultrasmooth edges have been produced by sonicating thermally exfoliated expandable graphite in solution [55, 63]. FET devices based on these GNRs have demonstrated an on/off ratio as high as 10^7 at room temperature, representing a significant breakthrough in the

field of graphene-based electronics [55, 63]. High on/off ratio has also been achieved in dual-gate bilayer graphene FETs, where a bandgap is created by applying a perpendicular electric field [64].

In this study, we present an alternative method to fabricate GNR-FETs that exhibit the characteristic ambipolar behavior and on/off ratio exceeding 10^4. We fabricated FET devices consisting of a GNR suspended ~150 nm above the underneath Si substrate (which is used as the back gate). Subsequently, we used controlled current annealing to create a narrow constriction in the suspended GNR to open a confinement gap, thus to afford a high on/off ratio at room temperature. Atomic force microscopy (AFM) was used to confirm the formation of a narrow constriction in the GNRs. Room temperature high on/off ratio graphene transistors have also been previously realized by creating nanometer size quantum dots (QD) using electron-beam lithography and plasma over-etching [65]. However, these lithographically defined graphene QDs have an on-state conductance at least two orders of magnitude lower than that of our devices, and do not exhibit ambipolar behavior, presumably due to the substantial disorder induced by the adsorbed impurities and/or edge roughness [65].

3.2 Experimental details

The GNRs were produced by sonicating mildly-oxidized multiwall carbon nanotubes (MWNT) in a 1,2-dichloroethane (DCE) solution of poly(m-phenylenevinylene-co 2, 5-diy octocy- p-phenyleneving lene) (PmPV), where the PmPV is used as a surfactant to stabilize the unzipped GNRs in solution [23]. The solution was then centrifuged at 15000 rpm (Fisher Scientific Marathon 26kmr centrifuge) for 1 hr to remove aggregates and some of the remaining

MWNTs; and a supernatant containing nanoribbons and remaining MWCTs was obtained. Next, the GNR samples from the supernatant were deposited on degenerately doped Si subtracts with 290 nm of thermal oxide, and subsequently non-contact mode AFM (Park System XE-70) was used to locate individual GNRs with respect to the prefabricated Au alignment marks and to characterize their thickness, width and length. The GNRs produced from this method mostly consist of 1-3 layers [23]. The AFM tip dilation effect (leading to artificial width increase) is accounted for based on the estimated tip radius provided by the tip manufacturer [28]. Standard electron-beam lithography (EBL) was used to pattern electrodes on selected GNRs followed by thermal metal deposition (a 0.5 nm Cr adhesion layer and 50 nm of Au) and lift-off in acetone. Suspension of the GNRs in FET devices was achieved by placing a small drop of 1:6 buffered hydrofluoric acid (HF) on top of the GNR device for 90 s to etch way approximately 150 nm of the SiO_2 underneath the ribbons [26, 27]. After wet etching, the device was transferred to hot isopropyl alcohol (which has low surface tension) and led try on a 120^0 C hot plate. Finally, the device was annealed in vacuum at 600^0 C to clean the ribbon surfaces and improve electrical contacts. In some of the studied devices, an additional EBL step was used to open a window in the electron-beam resist serving as etching mask for selectively etching the SiO_2 in the active device area. Both methods yielded similar results, with or without an additional EBL step. Surprisingly, about 50% of the over 30 devices with the suspended portion of the ribbon shorter than 800 nm survived the rather harsh fabrication processes.

The electrical transport properties of the suspended GNR devices were measured in high vacuum (10^{-6} torr in a Lakeshore Cryogenics vacuum probe station) and at room temperature unless stated otherwise. A semiconductor parameter analyzer (Keithley 4200) was used to apply

the annealing current and to measure the device characteristics. The degenerately doped Si substrate was used as a back gate. We repeatedly applied gradually increasing annealing current and subsequently carry out the electrical measurements *in situ* after every consecutive step. To avoid the possible collapse of the suspended GNRs, the back-gate voltage was limited to $-20 < V_g < +20$ V during the electrical measurements.

3.3 Results and discussions

We have studied over a dozen suspended few layer GNRs (1-2 nm thick) with a width between 15 and 50 nm. The length of the suspended GNR ranges from 100 nm to 800 nm. Figure 3.1(a) and (b) show atomic force microscopy (AFM) images of typical devices before and after etching, respectively. Line profile of the suspended GNR (Figure 3.1c.) indicates that the ribbon is suspended ~150 nm above the surface of the remaining SiO_2 without substantial slacking (sagging).

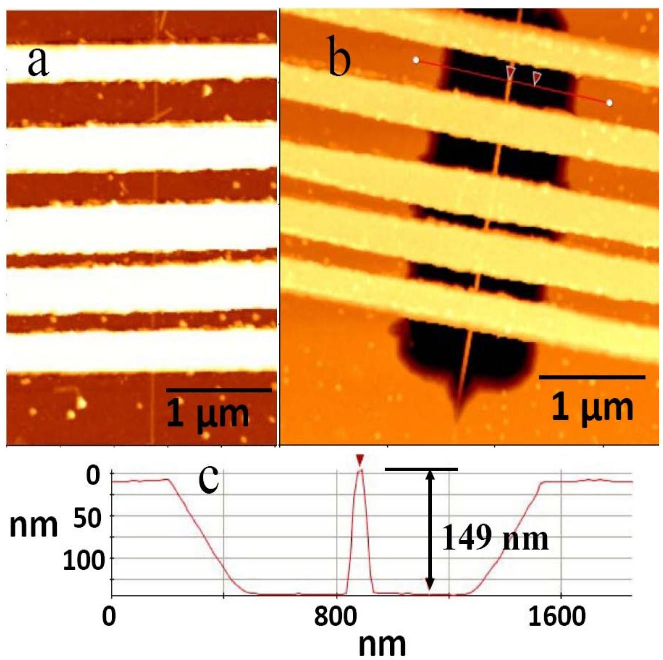

Figure 3.1 AFM images of typical FET devices consisting of a GNR contacted by Au electrodes before (a) and after (b) suspending the GNR. (c) Line profile of the top section of the suspended GNR.

3.3.1 Observation of large on/off ratio

Most of the suspended GNR devices used in this study showed ambipolar transfer characteristics with a charge neutrality point within a few volts from $V_g = 0$ after sufficient current annealing in vacuum (at a current density ~ 10^8 A/cm^2). No obvious layer number dependence was observed in the transfer characteristics of our few layer (1-3 layers) GNRs likely due to the none AB (Bernal) stacking in these GNRs [52]. Upon further increasing the annealing current, about 30% of the suspended GNRs showed dramatic increase of the on/off ratio in conductance (or drain-source current) as defined by the value measured at V_g = -15 divided by the value at the charge neutrality point, while the rest of the GNRs were destroyed during the annealing processes likely due to localized overheating or electromigration [66]. Figure 3.2 a shows the room-temperature conductance (G) versus gate voltage (V_g) for a representative suspended GNR device after sweeping the annealing bias-voltage from 0 to a predefined set-point of 2.9 V, and then decreasing the voltage back to 0 V, demonstrating the characteristic ambipolar behavior arising from the electron-hole symmetry of graphene. Figure 3.2 b shows that the current versus bias-voltage (I-V) of the device is linear at low bias voltages, indicating near Ohmic electrical contacts. Further current annealing (by slightly raising the predefined voltage set-point) dramatically reduces the minimum conductance, while the on-state conductance is essentially unchanged (within a factor of two) as shown in Figure 3.2 c. After the device is current annealed to 3.05 V, the on/off conductance ratio measured at V_{ds} = 10 mV

approaches 10^6. Figure 3.2 d shows the current versus gate voltage (I vs. V_g) of the same device measured at different bias voltages after current annealing to 3.05 V, revealing an on/off ratio > 10^4 for 10 mV ≤ V_{ds} ≤ 200 mV and 10^3 ~10^4 for V_{ds} = 500 mV. Such high on/off ratios at room temperature have been previously observed in sub-10 nm GNRs, which were attributed to the opening of an effective band-gap at the order of hundreds meV primarily due to the confinement effect [55]. Since the band-gap decreases as the ribbon width increases and our ribbon is approximately 20 nm wide, the confinement-induced band-gap in our ribbon is expected to be of the order of ~10 meV [17, 30, 67].

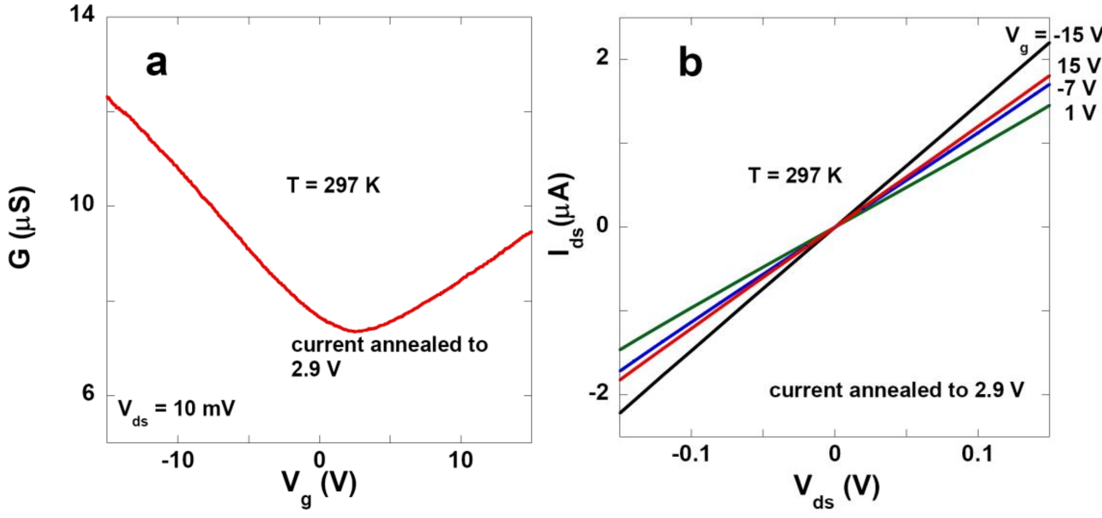

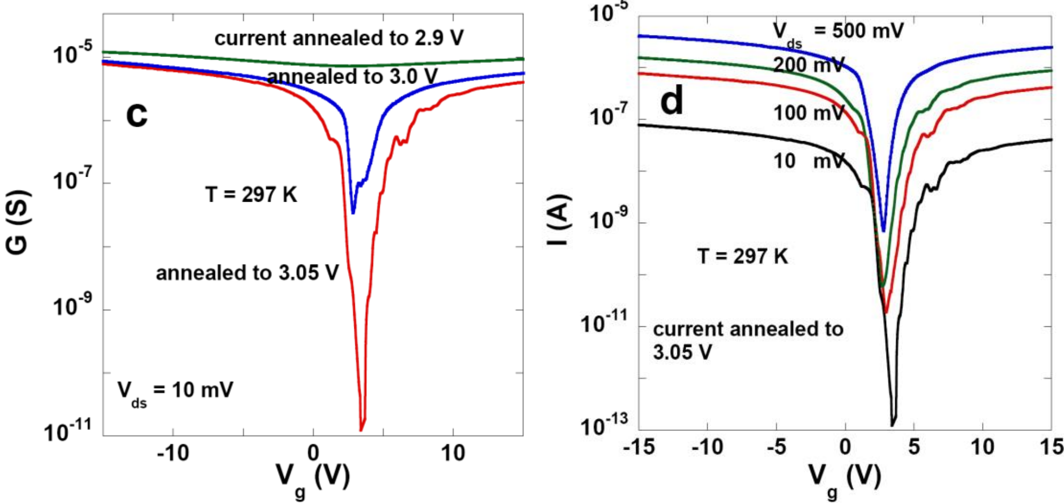

Figure 3.2 Electrical transport properties of a representative suspended GNR FET device measured at room temperature, where the suspended GNR is 21±3 nm wide, ~1.4 nm thick and ~600 nm long. (a) Transfer characteristic of the device after current annealing to a predefined bias voltage set-point of 2.9 V. (b) I-V characteristics of the device measured at various gate voltages ranging from -15 to 15 V. (c) Transfer characteristic measured after various degrees of current annealing. (d) Current versus gate voltage (V_g) measured at different bias voltages after the final stage of current annealing (annealed to 3.05 V).

3.3.2 Nano constriction

To elucidate the origin of the large on/ off ratio, we measured the G versus V_g curve of the suspended GNR device in Figure 3.2 at various temperatures (T) after it was annealed to 3.05 V. Figure 3.3 a shows a semi-logarithmic plot of the minimum current (I_{min}) at the charge neutrality point versus 1/T, of the device. The data fit well to the thermal activation law: $G_{min} \sim \exp(-E_g/2k_BT)$ (where k_B is the Boltzmann's constant), yielding a band-gap of $E_g \approx 0.6$ eV. A likely cause for such a large value of the band-gap and the consequent high on/off ratio is that further annealing beyond 2.9 V may have caused structural changes in the ribbon, such as creating a sub-10 nm constriction in the ribbon. In our suspended GNR devices, Joule annealing

removes the impurities on the ribbon surfaces [31], leading to the ambipolar behavior with the charge neutrality point occurring at Vg ≈ 0 V (Figure 3.2 a). Further annealing (increasing the pre-defined voltage set-point) facilitates structural reconstruction in the suspended ribbon, especially near the edges [68]. To confirm that annealing beyond 2.9 V created a narrow constriction in the ribbon, it is necessary to characterize the structure of the suspended GNRs especially at the end of the current annealing. Raman spectroscopy has proven to be a powerful and noninvasive tool to characterize the structures of graphene [69-72], however it lacks the spatial resolution that is needed to confirm the formation of a nanoscale constriction. While high resolution transmission electron microscopy (TEM) is capable of visualizing individual carbon atoms [73], it is difficult to directly characterize the structure of our GNR devices using TEM as they are fabricated on Si/SiO_2 substrates. In this study, we used AFM to characterize the suspended GNR device along with another suspended GNR device fabricated from an adjacent section of the same ribbon as shown in Figure 3.3 b. The two suspended sections are thus expected to have the same width, thickness and comparable length; except that no further current annealing was carried out in the lower section as soon as the characteristic ambipolar behavior with a low on/off ratio (< 10) was observed. Figure 3.3 c and d show the high resolution AFM images of two sections of the same ribbon with high and low on/off ratios, respectively, clearly indicating that i) both sections of the GNR are suspended without sagging (bowing); and ii) there is a notch near the middle of the section of the ribbon with high on/off ratio (Figure 3.3 c) while the GNR section with low on/off ratio is highly uniform (Figure 3.3 d). The notch in the AFM image is a clear indication that current annealing beyond 2.9 V created a narrow constriction in the suspended GNR, resulting in the large on/off ratio. It is also worth pointing out that the AFM

images in Figure 3.3 were taken after electrical measurements with a gate voltage swept between -15 and 15V and several thermal cycles between a cryogenic temperature (4.3 K or 77 K) and room temperature, demonstrating that our suspended GNRs are thermally and mechanically stable (even that GNR with a narrow constriction).

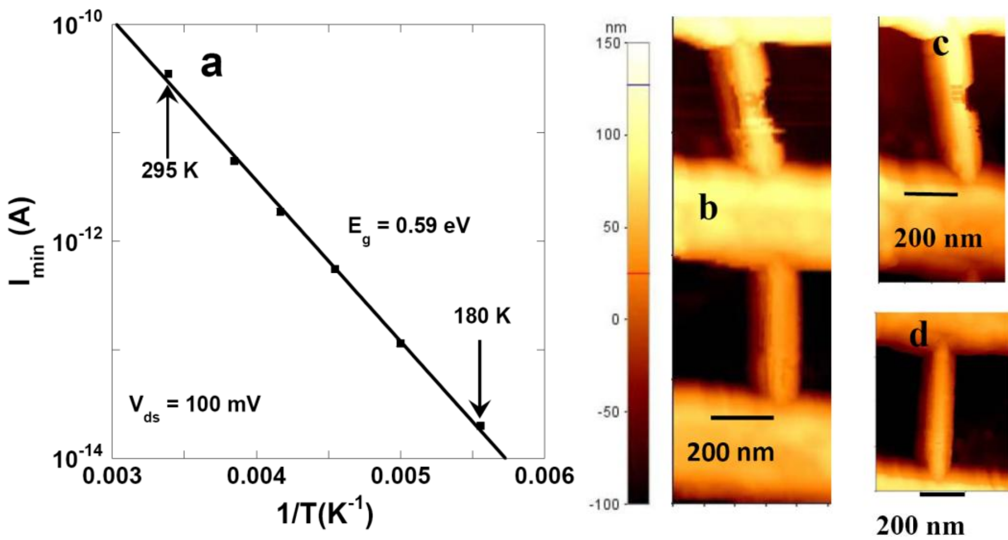

Figure 3.3 (a) Temperature dependence of the minimum current at the charge neutrality point measured at V_{ds} = 100 mV for the suspended GNR device in Figure 2. (b) Top part: AFM image of the same GNR in (a); bottom part: another section of the suspended GNR. (c-d) Higher resolution AFM images of the top and bottom sections of the GNR in (b), respectively.

3.3.3 Thermal and mechanical stability

Similar transfer characteristics and high on/off ratios have been observed in three other suspended GNR devices with varying width, length and thickness. Figure 3.4a shows the transfer characteristics of a device consisting of a suspended GNR ~450 nm long, ~45 nm wide, and ~1.6 nm thick. We note that before current annealing the suspended ribbon was p-doped with a charge neutrality point beyond +15 V, which can be partially attributed to the adsorption

of air or water molecules, or PMMA residue [74, 75]. After intermediate current annealing, the GNR exhibits ambipolar behavior with the minimum conductance associated with the charge neutrality point shifting to $V_g \approx 0$ V, indicating that the adsorbed charge impurities have been largely removed by current annealing. Further annealing decreases the minimum conductance by three orders of magnitude, while the overall transfer characteristics and the on-state conductance remain essentially unchanged. Figure 3.4 b shows that the transfer characteristics of the device remains virtually the same after number of thermal cycles, although the unintentional doping level changes after each thermal cycle as indicated by the shift of the minimum conductance along the horizontal axis. When the conductance G is plotted versus (V_g-$V_{G\text{-}min}$) in Figure 3.4 c, all the three curves collapse into a single one, indicating again that the electrical properties of our devices are robust. To further demonstrate the good thermal and mechanical stability of our high on/off ration devices, we measured the electrical properties of a third device (consisting of a GNR ~ 19 nm wide and ~1.2 nm thick) before and after an additional *ex situ* annealing step at 600 ^{O}C in a vacuum furnace. Figure 3.4 d shows that the transfer characteristic of the device remains essentially the same after the additional *ex situ* annealing step.

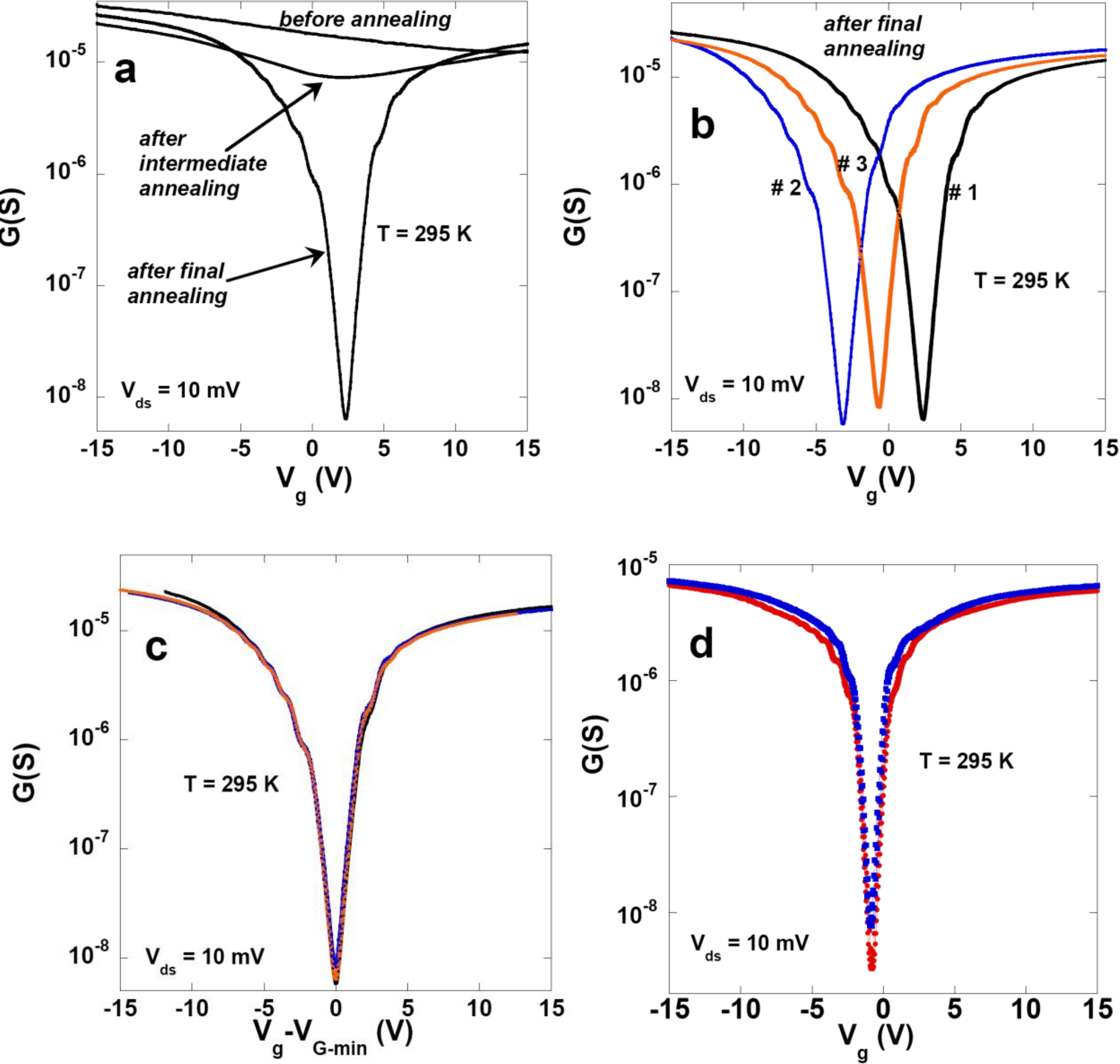

Figure 3.4 (a-c) Transfer characteristics of a second suspended GNR FET device measured at room temperature; the suspended GNR is 45±3 nm wide, ~1.6 nm thick and ~450 nm long. (a) Transfer characteristic measured after various degrees of annealing. (b) Conductance versus gate voltage measured at room temperature after the final current annealing stage and after different number of thermal cycles; # 1, #2, and #3 next to the corresponding $G(V_g)$ curves represent measurements after 1, 2 and 3 thermal cycles, respectively. (c) Gate dependent conductance data in (b) plotted as a function of V_g-$V_{G\text{-}min}$. (d) Room temperature transfer characteristics of a third suspended GNR device (19±3 nm wide, ~1.2 nm thick, and ~300 nm long) measured before (blue solid squires) and after (red solid dots) *ex situ* annealing at 600 ^{O}C for 10 minutes in a vacuum furnace.

High on/off ratios have been observed in GNRs of comparable width (tens of nanometers wide) but usually at cryogenic temperatures and have been attributed to the opening of a transport gap [17, 18, 21, 76-77]. Several possible mechanisms have been proposed to explain the large transport gap observed in GNR-FETs at low temperatures, ranging from re-normalized lateral confinement due to localized edge states [17, 18], to percolation driven metal-insulator-transition caused by charged impurities [21], to quasi-one-dimensional Anderson localization [20], and to Coulomb blockade due to edge-roughness [78]. More recent experimental studies on disordered GNRs further indicate that charge transport in the conduction gap of GNRs is likely dominated by localized states [76] and/or isolated charge puddles acting as quantum dots [77]. These mechanisms may partially contribute to the high on/off ratio in our devices. However, they are unlikely the primary cause, since the over 10^4 on/off ratio in our devices was observed at room temperature and only after sufficient current annealing. For instance, when the device in Figure 3.2 is current annealed up to 2.9 V, the on/off ratio is less than 2. The large on/off ratio in the device was obtained only after it was current annealed by applying a bias voltage beyond 2.9 V.

3.3.4 Theoretic explanation

Based on the results of AFM characterization of the suspended GNRs (Figure 3.3), we suggest that the formation of a constriction, at the critical annealing current, as the most likely origin of the high on/off ratio. Figure 3.5 a-c schematically shows a relatively wide uniform GNR (GNR_0), the same GNR with a narrow constriction, which effectively forms a finite ribbon (GNR_1), and a narrow uniform GNR (GNR_2) with a descending width ($GNR_0 > GNR_1 > GNR_2$).

Because of the stronger confinement in the narrow constriction (GNR_1) compared to the uniform wide GNR (GNR_0), the bandgap for GNR_1 (Figure 3.5 e) is expected to be larger than that for GNR_0 (Figure 3.5 d). In the same fashion, the bandgap of GNR_2 (Figure 3.5 f) is larger than that of GNR_0 (Figure 3.5 d) due to its narrower width [16-17, 54]. In addition to the lateral confinement, region GNR_1 is also longitudinally confined by regions QD_1 and QD_2. The longitudinal confinement further increases the bandgap of the otherwise infinite ribbon GNR_1 to a value that can be possibly larger than that for the narrower ribbon GNR_2, thus resulting in higher on/off ratios. Therefore, the double-confinement picture seems to be responsible for the high on/off ratios which are comparable to those of possibly much narrower (sub-5nm) ribbons [24]. More quantitative understanding of the large bandgap requires detailed information on the dimensions and even the edge structures of the nano-constrictions, which is beyond the scope of this work. Recently, bandgaps of ~ 50 meV have been observed in relatively wide (~ 100 nm) annealed nanotube-derived GNRs [79], indicating that it is possible to obtain a bandgap ~ 500 meV in GNRs of ~ 10 nm wide. However, the bandgap of these GNRs was substantially larger than that of much narrower GNRs synthesized using a similar approach; and the difference in edge structures was suggested as the primary cause of the discrepancy [23, 79]. Unfortunately, the lack of edge information on these GNRs prevents the definitive identification of the true origin of the discrepancy.

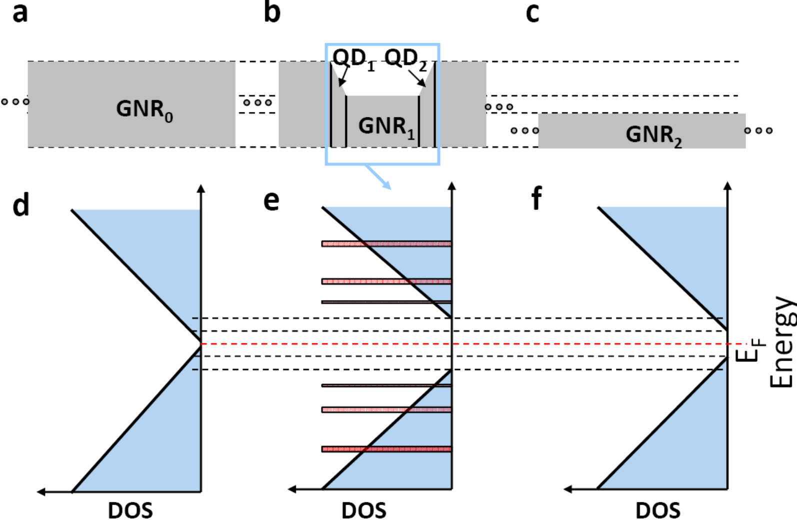

Figure 3.5 Schematic density of states (DOS) for GNRs. (a) and (c) represent two infinite GNRs of different widths; the corresponding energy bandgaps, observed in the DOS panels (d) and (f), follow the known inverse relation with ribbon width. (b) GNR with a constriction. (e) DOS projected on the region of the constriction; the quantized energy levels of quantum dots QD_1 and QD_2 are shown in red and the states of region GNR_1 are shown in blue.

Discrete conductance peaks, superimposed on the main G-vs-V_g curve, were observed at low temperatures in some annealed samples (Figure 3.6). These conductance oscillations can be attributed to the quantized energy levels of regions QD_1 and QD_2 in Figure 3.5 b, which because of lack of any periodicity or quasi-periodicity act as two quantum dots in series. Therefore, these conductance peaks are due to resonant tunneling through the quantized levels of the dots (shown in red in Figure 3.5 e) tuned by the applied gate voltage. The spacing and periodicity of such peaks depend on the size and symmetry of the quantum dots. Asymmetry between the discrete energy levels of QD_1 and QD_2 leads to lack of resonance and random cancellation of the transmission through some levels [65].

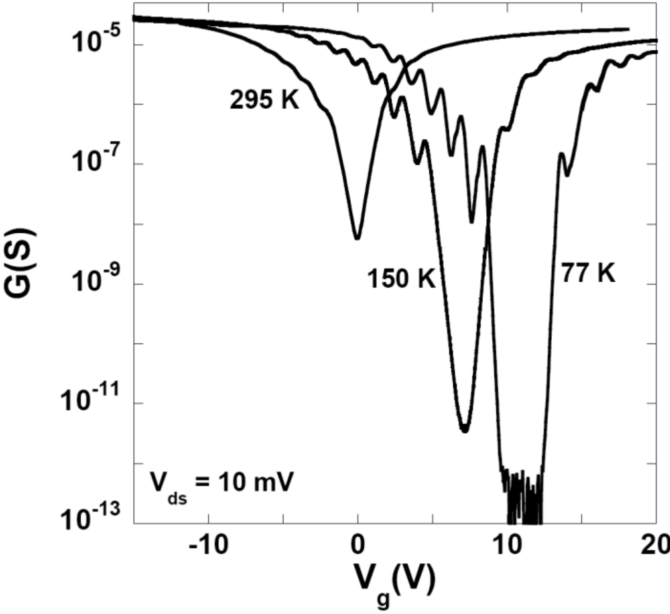

Figure 3.6 Conductance versus gate voltage of the GNR device in Fig. 4d measured at 77, 150, and 295 K.

During the course of this work, we became aware that room-temperature high on/off ratios were also observed in graphene nano-constrictions created by first forming a constriction in the gold etch mask covering the graphene channel (using electromigration) and subsequent plasma etching of the underneath graphene [79]. However, the nano-constrictions presented in this work are created without a mask, which may lead to much cleaner graphene nano-constrictions with substantially lower disorder.

3.3.5 Bandgap validation

The coulomb diamond [16] associated with the narrow constriction caused by current annealing was measured as well using DC measurement to get as many as *I-V* curves. Figure 3.7 shows the measurement of the coulomb diamond at 200K, leading to the bandgap around 700

meV consistent with the value calculated from thermal energy gap. This is also the direct evidence showing that a gap further opens up when narrowing down the dimensions of graphene nanoribbons using current annealing.

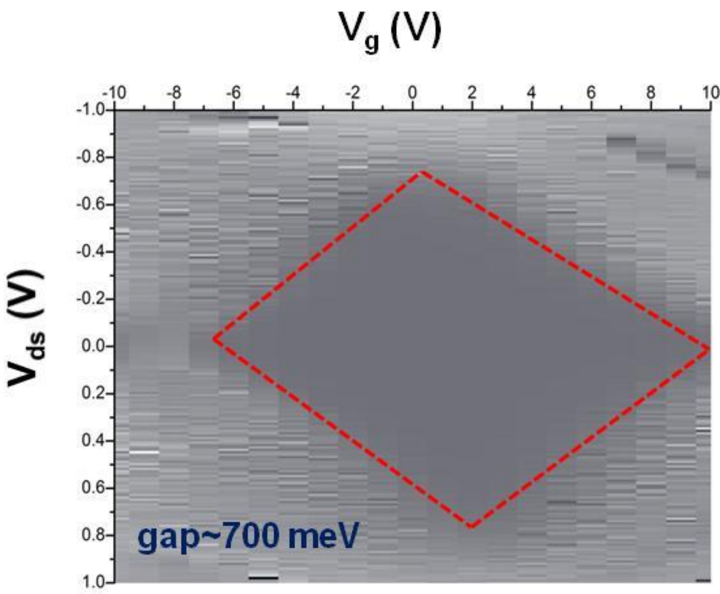

Figure 3.7 The coulomb diamond plotted from the DC measurement data of *I-V* curve varying with gate voltage at 200K, leading to the gap size around 700 meV.

3.4 Summary

The suspended GNR-FET devices from GNRs derived from high quality MWNTs have been fabricated. By controlled current-annealing of the suspended GNRs, a large band gap at the order of hundreds meV can be created in GNRs with varying width and thickness, leading to orders of magnitude increase of on/off ratio at room temperature. The formation of such a large band gap can be largely attributed to the creation of a narrow constriction in the suspended GNR as confirmed by AFM. Furthermore, the suspended GNRs and their narrow constrictions are

structurally robust, and the electrical properties of the devices remain unchanged after number of thermal cycles. The mask-free fabrication method presented in this study also creates opportunities for studying ultraclean graphene quantum dots.

CHAPTER 4

GRAPHENE NANORIBBONS WITH GRAPHITE POWDER

4.1 Introduction

There have been many research works increasing recently related to graphene and graphene nanoribbon no matter in fundamental research or practical applications [2]. Several different methods have been developed to produce graphene, including mechanical cleavage [1], chemical vapor deposition, epitaxial growth [54], and exfoliation of graphite (as well as its derivatives and intercalation compounds) in solution [80, 81] as mentioned in chapter 1. The solution method is not only scalable but also well-suited for chemical functionalization, creating opportunities for a wide range of applications [82]. Graphene oxide can be easily exfoliated in solution and subsequently reduced to graphene. However, the harsh oxidation process used to synthesize graphite oxide leaves functional groups on graphene; and removing such oxygen containing groups through chemical or thermal reduction simultaneously produces structural defects [83-85], which unavoidably degrade the electrical properties of the graphene. Coleman's group has recently demonstrated that large quantity of high-quality unoxidized graphene could be produced and dispersed in various organic solvents [81, 86, 87]. However, the electrical transport properties of graphene produced from the exfoliation of unoxidized graphite in solution remain largely unexplored, in spite of their relevance to various electronic applications. A reported transport study of individual few-layer graphene produced by exfoliating graphite in

organic solvent showed no gate-voltage dependence of the conductance, while gate tunability is an essential characteristic of high quality graphene [88]. The lack of gate tunability in these dielectrophoretically assembled individual graphene devices was attributed to the relatively small gate voltage window [88]. Therefore, further electrical transport studies of solution-produced graphene are necessary for understanding their charge transport mechanism and exploring their potential for various electronic applications.

In this work, a simple one-stage synthesis method other than using nanotubes was demonstrated to produce grapheme nanoribbons (GNRs) with large length-to-width ratios and straight edges by sonicating graphite powder directly in organic solution, without any prior chemical treatment of the graphite. To understand the transport mechanism and shed light on the nature of the remaining disorder in our GNRs, we fabricated field effect transistor (FET) devices consisting of individual few-layer GNRs and measured their transport properties in both the back-gate and polymer-electrolyte top-gate configurations. An order of magnitude mobility increase is observed in the latter configuration than in the former configuration (without the polymer electrolyte) due to the ionic-screening effect of the polymer electrolyte, suggesting that the charge transport in these GNRs is largely limited by charged impurity scattering.

4.2 Experimental details

Sieved graphite powder (10mg, Sigma Aldrich) was dispersed in a solution of 10 ml 1,2-dichloroethane (DCE) and 2 mg poly(m-phenylenevinylene-co 2, 5-diy octocy-pphenylenevinglene) (PmPV) by bath sonication (Branson 3510 ultrasonic cleaner) for 1 hr. After sonication, we obtained a homogeneous black suspension of graphene sheets and a large

amount of macroscopic aggregates. The dispersion was then briefly centrifuged (5 minutes) at 15000 rpm (Fisher Scientific Marathon 26kmr centrifuge) to remove aggregates and larger graphene sheets; and a supernatant containing thin graphene sheets and nanoribbons was obtained. Raman spectroscopy and non-contact mode atomic force microscopy (AFM, Park System XE-70) were used to characterize the graphene samples deposited on Si/SiO_2 substrates from the supernatant. Raman Spectra were collected using a Jobin–Yvon Horiba Triax 550 spectrometer, a liquid-nitrogen cooled charge-coupled device (CCD) detector, an Olympus model BX41 microscope with a 100 × objective, and a Modu-Laser (Stellar-Pro-L) Argon-ion laser operating at 514.5 nm. The laser spot size was a few micros and the laser power at the sample was maintained at low level (~ 2 mW) to avoid any heating effect. To determine the ribbon width, the artifical width increment (ΔW) due to tip dilation as determined by both the ribbon thickness (h) and tip radius (R):$\Delta W = 2[h(2R - h)]^{1/2}$ is subtracted from the apparent widths in the AFM images using the measured ribbon thickness and estimated tip radius provided by the tip manufacturer [28].

To characterize the electrical transport properties of GNRs, we fabricated FET devices of individual GNRs deposited on degenerately doped Si substrates with 285 nm of thermal SiO_2, where the Si substrate was used as the back gate. To remove the PmPV and solvent residue, the substrates were heated in air at 375^0C for 15 minutes and annealed at 600^0C for 10 minutes with flow of forming gas to further clean the samples and substrate [55]. Subsequently, non-contact mode AFM was used to locate and characterize GNRs with respect to prefabricated Au alignment marks. Electrodes were fabricated on selected GNRs using standard electron beam lithography followed by electron beam assisted deposition of a 1 nm Cr adhesion layer and 50

nm of Au. The devices are annealed in vacuum at 600^0C for 10 minutes to clean the ribbons and improve the electrical contacts before transferred to a Lakeshore Cryogenics vacuum probe station for electrical transport measurements. Additional current annealing was carried out on some devices to further remove adsorbed impurities prior to transport measurements in high vacuum (~ 10^{-6} torr).

To further elucidate the nature of the remaining disorder in the GNRs, we fabricated an additional top-gate with solid polymer electrolyte consisting of lithium perchlorate (LiClO4) and poly(ethylene oxide) (PEO) in the 1:8 weigh ratio. The top-gate electrodes were simultaneously patterned on the substrate along with the drain and source electrodes. Electrical properties of the devices were measured by a semiconductor parameter analyzer (Keithley 4200) in vacuum (1×10^{-6} torr).

4.3 Results and discussions

4.3.1 Raman spectroscopy measurement

To globally characterize the extent of exfoliation and the quality of the solution exfoliated graphene, we deposited the graphene on a Si substrate and performed Raman Spectroscopy measurements at several randomly selected locations. Nearly identical Raman spectra were obtained at all locations. Figure 4.1 shows a representative Raman spectrum exhibiting three bands: the D band (~ 1354 cm^{-1}), G band (~ 1582 cm^{-1}) and 2D band (~ 2712 cm^{-1}). For comparison, a Raman spectrum obtained on the starting graphite powder is also included in Figure 4.1. The shape of the 2D band for the solution exfoliated graphene clearly

differs from that for the graphite powder, indicating that the majority of the exfoliated graphene flakes consist of few layers (< 5 layers). In addition, the D-to-G-band intensity ratio (I_D/I_G) for the solution exfoliated graphene (~0.5) is significantly higher than that in the starting graphite powder (~ 0). The presence of a D peak is usually attributed to edges and/or topological defects in the basal plane; and the I_D/I_G increases with the overall structural disorder. Since the average size of the solution-exfoliated graphene flakes (typically hundreds of nanometers as discussed below in detail) is much smaller than the laser spot size (~ a few microns), the increased I_D/I_G in the exfoliated graphene in comparison with the starting graphite can be largely attributed to the edges of the solution produced graphene [86]. On the other hand, the I_D/I_G in our solution exfoliated graphene is still substantially smaller than that in chemically reduced graphene [89], suggesting that our solution produced graphene flake contains lower disorder than that in reduced graphene.

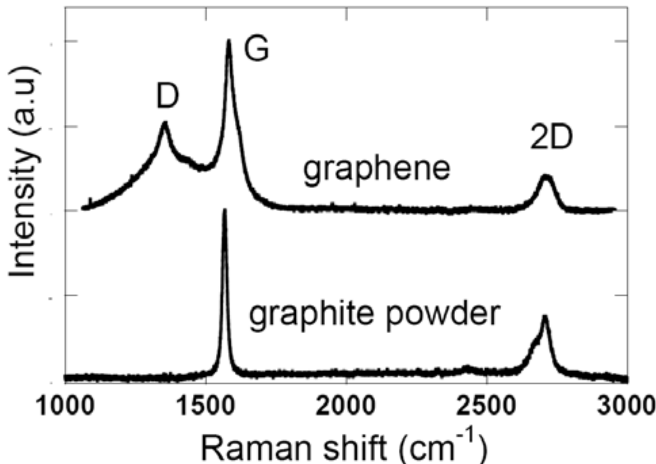

Figure 4.1 Raman Spectra of solution exfoliated graphene and starting graphite powder. The intensity in each spectrum is normalized to its G-band intensity.

4.3.2 AFM characterization

Next, AFM was used to characterize a large number of the solution exfoliated graphene samples deposited on a Si substrate. In addition to irregular-shaped graphene flakes, narrow ribbons of single-layer or few-layer graphene with relatively high aspect ratios (sub-10 nm to tens of nm wide and hundreds of nm to 1 μm long) were also routinely observed. Figure 4.2(a) and (c) show representative AFM images of a substrate surface deposited with graphene sheets and nanoribbons. Figure 4.2(b) and (d) are zoomed images of the two GNRs from the marked areas in Figure 4.2(a) and (c), respectively. Their widths are 6~8 nm and 23~26 nm, respectively [28]. From their line scans [Figure 4.2(e) and (f)], we estimate that the GNR in Figure 4.2(b) is ~1 nm thick; and the GNR in Figure 4.2(d) is ~ 2 nm thick. Based on the previously reported AFM results of graphene sheets and nanoribbons [1, 55], they are likely to contain one and few monolayers (3- 4 layers), respectively. A few GNRs with widths less than 100 nm were observed in each randomly selected 10 μm × 10 μm area on the Si/SiO_2 substrates soaked in the GNR solution for 1 hr. Figure 4.3(a) and (b) show the topographic height and length distributions of over 100 GNRs with widths less than 100 nm as characterized by AFM. The minimum topographic height is 0.8 nm, and the heights of most GNRs fall into the range between 1 nm to 3 nm, suggesting that the GNRs are mostly few layers and consistent with the Raman spectroscopy data. The lengths for most of the GRNs range from 300 nm to 1 um, which allows us to fabricate FET devices on individual GNRs.

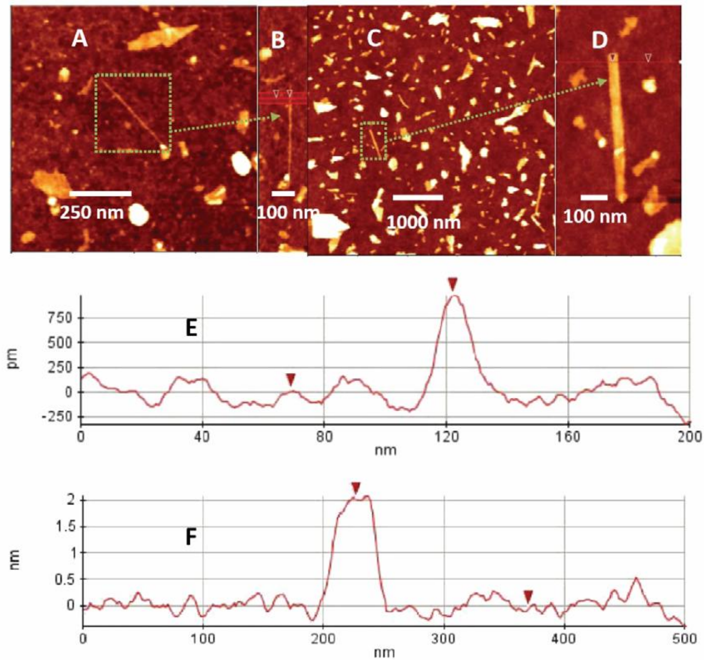

Figure 4.2 GNRs produced from sonicating graphite power in DCE solution of PmPV. (a - d) AFM images of GNRs deposited on SiO_2 surface. (b and d) Zoomed images of the marked areas in (a) and (c), respectively: the width of the GNR in (b) is 6 ~8 nm; the width of the GNR in (d) is 23 ~ 26 nm. (e and f) Line profiles of the two GNRs in (b) and (d), respectively.

We emphasize that the use of PmPV polymer and humidity are two factors critical to producing GNRs with high aspect ratios. We were unable to produce GNRs without PmPV under the otherwise nominally identical conditions, consistent with the finding of Li *et al* in their study of GNRs produced from expandable graphite [55]. Similar to polyvinylpyeeolidone (PVP), which has been shown to help decrease the possibility of cutting long GNRs into shorter pieces [56], suggesting that the PmPV conjugated polymer known to non-covalently attach to graphene not only stabilizes the exfoliated graphene in solution but also reinforces the structural integrity of GNRs in the solutions, protecting them from breaking down to smaller particle-like structures. Furthermore, we have found that the yield of graphene ribbons or sheets significantly

decreases when samples were prepared in dry laboratory air (relative humidity ≤ 15%) using dry graphite powder (exposed to only dry nitrogen or dry laboratory air) and anhydrous DEC solutions of PmPV. Increasing sonication time alone does not substantially increase the yield of thin graphene sheets and nanoribbons. Instead, excessive sonication (>2hr) only breaks graphite flakes into smaller particulates (tens of nanometers in lateral dimensions as well as in thickness). The yield of graphene ribbons and sheets noticeably increased when the graphite powder was exposed to relatively humid air (relative humidity > 25%) before mixing with DCE solutions of PmPV. While more detailed investigation of parameters affecting the exfoliation efficiency is needed, we tentatively attribute our experimental observation to water-molecule induced reduction of friction between adjacent graphene layers in graphite [90], which in turn facilitates more efficient exfoliation of grapheme through sonication. A likely scenario is that the dangling bonds at the edge sites of graphite need to be saturated by molecules such as water molecules in order to maintain the low-friction behaviors [91, 92].

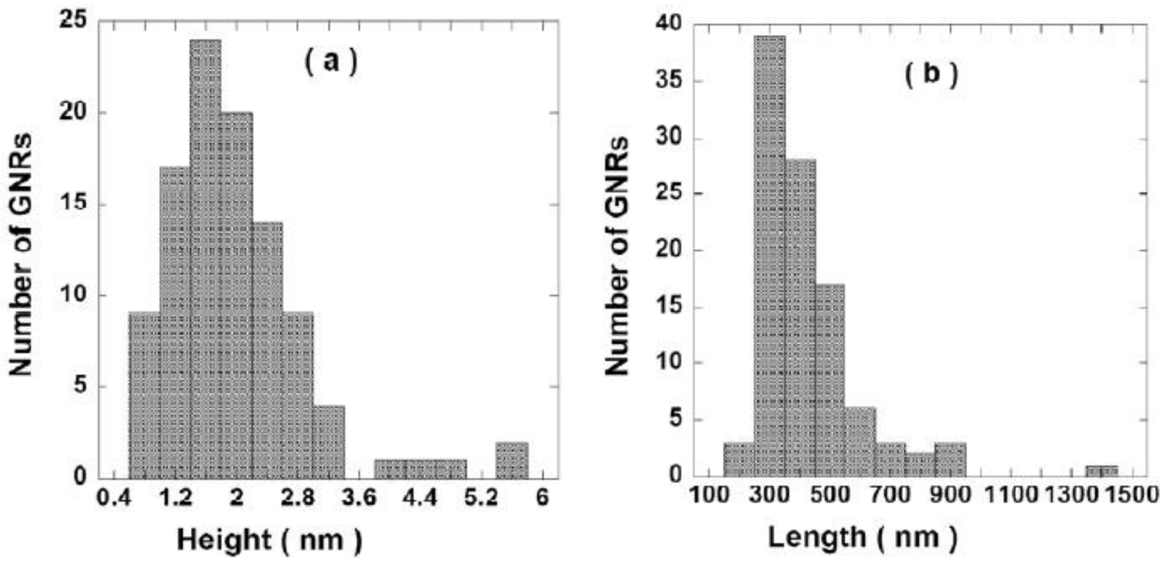

Figure 4.3 Histograms of topographic heights (a) and lengths (b) of over 100 GNRs imaged by AFM on SiO_2 surface: graphene samples narrower than 100 nm with a length to width ratios large than 3 are included. GNRs with length- to-width ratio > 10 are routinely observed.

4.3.3 Electrical transport with polymer gate

To characterize the electrical transport properties of individual GNRs, field-effect transistor devices consisting of individual GNRs were fabricated. Figure 4.4 shows the electrical transport characteristics of a typical GNR device (L ~ 280 nm, W ~ 33 nm, and d~2 nm corresponding to about 3 layers). The AFM image of the device is depicted in the inset. The lowbias current-voltage (I-V) characteristics of the device are linear at all measured gate voltages [see Figure 4.4(a)], indicating near Ohmic electrical contacts. As shown in Figure 4.4(b), the transfer characteristic of the GNR device was p-doped with a charge neutrality point (CNP) beyond + 80 V before current annealing, which can be partially attributed to the adsorption of air or water molecules, or PMMA residue [74, 75]. After current annealing, the GNR exhibits ambipolar behavior with the minimum conductance associated with the CNP shifting to Vg ~ 18 V, indicating that the adsorbed charge impurities have been partially removed. In addition, the overall conductance decreases after current annealing, which can be attributed to the lower carrier density due to the reduced impurity doping upon the removal of adsorbed impurities. From the transfer characteristics, the field effect mobility can be estimated as the following, similar to Eq. (2.3):

$$\mu = [\Delta G \times (L/W)]/(C_{bg}\Delta V_g) \qquad (4.1)$$

Here G is the low-bias conductance of the sample [35]; L and W are the channel length and width, respectively; and C_{bg} is the back-gate capacitance (estimated to be ~ 6×10^{-8} F/cm^2 based on the capacitance of GNR-FET devices with similar ribbon width [30]). The hole mobility (both before and after current annealing) is ~20 cm^2/V s, and the electron mobility (after current annealing) is about ~ 5 cm^2/V. Similar mobility values are observed in three other few layer GNRs with the ribbon width ranging from 20 nm to 100 nm. These mobility values are over an order of magnitude higher than those reported for chemically reduced graphene oxide [93], suggesting lower disorder in our GNRs than in reduced graphene. However, they are still noticeably lower than the mobility values of GNRs produced from some other methods [23, 63, 94], suggesting that our GNRs still contain a substantial amount of disorder.

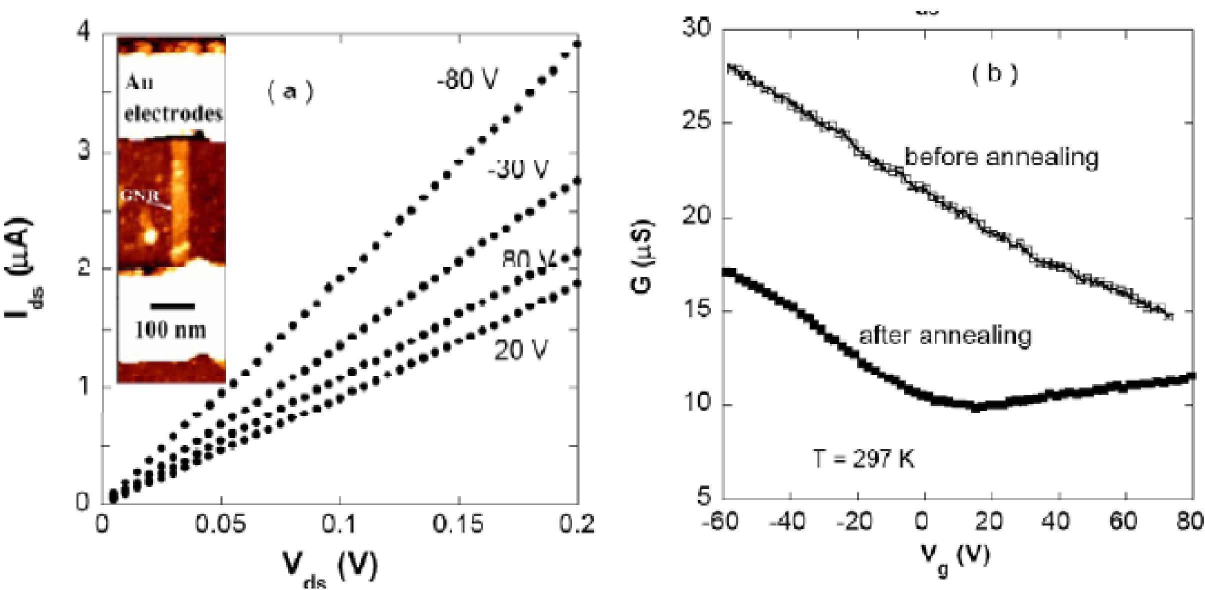

Figure 4.4 Electrical properties of a GNR-FET device. (a) Drain-source current versus drain-source voltage measured at various back-gate voltages. (b) Room Conductance versus back-gate voltage measured at 297 K before and after current annealing. Inset: AFM of the measured GNR-FET devices with two Au electrodes contacting an individual GNR.

Carrier mobility in GNRs is largely determined by the phonon scattering, charged impurities on the GNR surfaces and in the SiO_2 substrate, structural defects in the basal plane, and edge-disorder [35]. Since our GNRs are formed by the tearing effect of bursting ultrasonic hot gas bubbles, we expect them to have smoother edges and lower edge disorder than lithographically defined GNRs [55, 63]. To further elucidate the nature of the remaining disorder in the GNRs, the temperature dependence of the transfer characteristics on some devices was measured. Subsequently, an additional polymer-electrolyte top-gate was fabricated and measured their electrical transport characteristics under the top-gate configuration. An optical micrograph of a representative polymer-electrolyte top-gated GNR device is shown the inset of Figure 4.5(b). Substantial performance improvement has been previously demonstrated in carbon nanotube FETs in the polymer-electrolyte top-gate configuration than in the back-gate configuration due to the enhanced gate-channel coupling [95]. Figure 4.5(a) shows the comparison of the transfer characteristics of another GNR (~ 200 nm long, ~ 50 nm wide and ~ 1.5 nm thick corresponding to 2 layers) operating in the back-gate configuration without polymer electrolyte and operating with a polymer electrolyte top-gate. Without the polymer electrolyte, i) the GNR was p-doped with a CNP beyond the measured back-gate voltage range; and ii) the transfer characteristics of the device are nearly temperature independence for $4.3 < T < 297$ K, in sharp contrast with the over 3 orders of magnitude conductance decrease in chemically reduced graphene upon cooling from room temperature to 4 K [89]. The nearly temperature independent transfer characteristics suggest that our solution exfoliated GNRs contain much lower structural disorder than chemically reduced graphene. The low-temperature on-off ratio of our GNRs is much smaller than that of typical lithographically-defined GNRs with comparable widths [16,

17, 22]. The high on-off ratio observed at low temperatures in the latter can be attributed to the opening of a transport gap near the CNP due the combined effects of a small confinement gap and disorder induced potential fluctuations [22]. However, our GNRs are strongly p-doped and away from the CNP for the entire measured back-gate voltage range. The conductance versus polymerelectrolyte top-gate of the same device exhibits highly symmetric ambipolar behaviors. Moreover, the field effect hole-mobility increases from ~ 11 $cm^2/V{\cdot}s$ in the back gate configuration (prior to adding the polymer electrolyte) to ~ 120 $cm^2/V{\cdot}s$ in the polymer electrolyte top gate configuration (the top-gate capacitance used to derive the field effect mobility is estimated to be ~ 1μF/cm^2 [96]; and the leak current remains below 500 pA within the top-gate voltage range examined). The highly symmetric transfer characteristic of the GNRs measured in the polymer-electrolyte top-gate configuration also enables a more accurate estimation of the carrier mobility by excluding the contact resistance contribution using the following model same as Eq. (2.1):

$$R_{total} = R_{contact} + R_{channel} = R_{contact} + \frac{L/W}{ne\mu} \quad (4.2)$$

Here, $R_{contact}$ and $R_{channel}$ are the metal/GNR contact resistance and GNR channel resistance, respectively [29]; L and W are the channel length and width, respectively; μ is the carrier mobility, and the carrier concentration n, can in turn be determined by the similar expression described as Eq. (2.2):

$$n = \sqrt{n_o^2 + C_{tg}(V_{tg} - V_{CNP})^2} \quad (4.3)$$

Here, n_o is the residual carrier concentration at the maximum resistance, C_{tg} is the polymer electrolyte top-gate capacitance (~ 1×10^{-6} F/cm^2) [96], and V_{CNP} is the gate voltage at the CNP [29, 97]. Besides the contact resistance, scattering mechanisms such as point defects and phonons may also contribute to the gate-independent resistance [98, 99]. However, these scattering mechanisms become significant only in high mobility graphene samples; and are expected to give very minor contributions to the gate-independent resistance in our GNRs with relatively low mobility (see detailed discussions below). As shown in Figure 4.5(b), this model fits our experimental data reasonably well, yielding a mobility value of 180cm^2/V·s in reasonable agreement with the field effect mobility (~120 cm^2/V·s). This mobility value is also comparable to the mobility of lithographically and chemically derived GNRs of similar widths [17, 63]. The slightly larger mobility value from the model fitting compared to the field effect mobility is largely due to the exclusion of the contact resistance. Although this model assumes a gate independent contact resistance, we believe this is a reasonable assumption for our devices given the nearly ohmic contact and reasonably good fit of the data to the model, which is also consistent with the findings of Russo *et al.* [34].

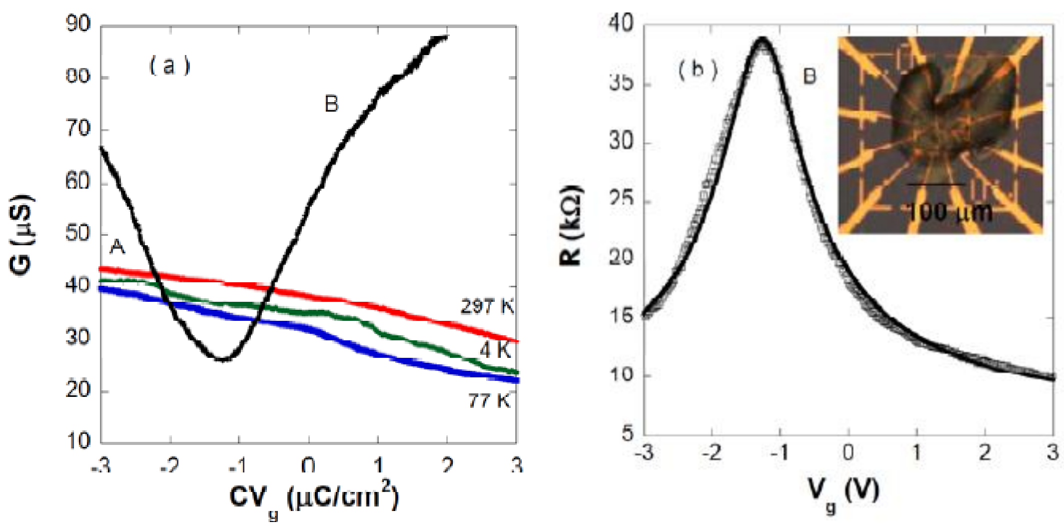

Figure 4.5 (a) Comparison between back gating without the polymer electrolyte (A), and polymer top gating (B) on the same GNR-FET device. (b) Resistance versus polymer top-gate voltage for the same device. The solid lines in (b) are the model fitting. Inset: optical micrograph of the device with polymer electrolyte gate.

On the one hand, the polymer electrolyte adds extra charged impurities to the GNRs, which is expected to reduce the mobility in the GNRs [100]. On the other hand, counter-ions in the polymer electrolyte accumulate on the GNR to neutralize the effects of charged impurities [101]. Two orders of magnitude increase of mobility has been previously observed in graphene FET devices immersed in ionic solutions, which was attributed to the ionic screening of charged impurity scattering in graphene [101]. The order of magnitude mobility increase in our GNR devices upon the application of a polymer-electrolyte top-gate along with the nearly linear gate dependence of the conductance indicates that the ionic screening effect dominates in our samples. This in turn suggests that the charge transport in our GNRs is largely limited by charged impurity scattering. The screening-induced mobility enhancement was also observed in the back-gate configuration (with polymer electrolyte) although at a lesser degree. The reduced screening effect in the back-gate configuration may be due to the electrostatic shielding of the top-layer in few layer (2-3 layer) GNRs, while the electrolyte top-gate directly tunes the carrier density in the top layer [52]. A likely source of charged impurities is the metallic impurities in the starting graphite powder. Charged impurities could also be introduced in the GNR synthesis and device fabrication processes. It is also worth noting that ion-screening is more effective than current annealing in reducing the charged impurity scattering in our substrate supported GNRs with initially relatively low mobility. While current annealing only partially removes impurities on the top surface of the GNRs, the counter ions in the polymer electrolyte are able to neutralize

charged impurities not only on the top surface but also trapped beneath the ribbon. Due to the freezing of the ions in the polymer electrolyte at low temperatures, we were unable to measure the temperature dependence of the transport characteristics in the top-gate configuration.

4.4 Summary

We have developed a simple solution method to produce GNRs from graphite powder without any prior chemical treatment of the graphite. Single layer and few layer GNRs as narrow as sub-10 nm were observed by AFM. The main advantages of this method include 1) simplicity in production; and 2) free of covalent functionalization of GNRs. To characterize the electrical properties of the GNRs, we fabricated FET devices consisting of individual GNRs using electron beam lithography followed by the deposition of Cr/Au. The transfer characteristics of the devices show p-doping behavior, and the mobility of the devices is estimated to be at order of 10 $cm^2/V\cdot s$. Transport measurements of the same devices in the polymer-electrolyte top-gate configuration shows an order of magnitude mobility increase, which can be attributed to ionic screening of charged impurity scattering. We expect that higher mobility is achievable in these GNRs by further reducing the disorder induced by charged impurities.

CHAPTER 5

MONOLAYER MoS_2 TRANSISTORS WITH POLYMER ELECTROLYTE

5.1 Introduction

Although graphene opened the possibility of "post-silicon" high performance electronics because of its one atomic-layer thickness and extraordinarily high carrier mobility [26, 27, 31, 102], the lack of an appreciable bandgap in graphene gives a major problem for conventional digital applications. MoS_2 is a semiconductor with the direct bandgap~ 1.8 eV, which makes it a suitable channel material for low power digital electronics [103]. Similar to graphene, this material can be mechanically exfoliated using adhesive tape to have single or multi-layers.

In this study, we report a simple method to fabricate high mobility (~10^2 $cm^2V^{-1}s^{-1}$) MoS_2 FETs by covering the devices with a thin layer of polymer electrolyte (PE) consisting of poly(ethylene oxide) (PEO) and lithium perchlorate ($LiClO_4$). The estimated room-temperature field-effect mobility of the monolayer MoS_2 FETs increases by up to three orders of magnitude upon adding the PE. To study the respective influence of the MoS_2/metal contacts and MoS_2 channel on the device characteristics, we fabricated multiple devices with different channel lengths on a single ribbon of monolayer MoS_2 with uniform width. Electrical characterization of these devices reveals that the PE-induced mobility enhancement can be attributed partially to the drastic reduction of contact resistance and partially to the increase of the channel mobility. The improvement of the channel mobility is likely due to the neutralization of the uncorrelated

charged impurities on or near the MoS_2 channel by the counter ions in the PE [35, 101, 110]. Furthermore, we demonstrate for the first time that near ideal gate-channel coupling can be achieved in our PE gated MoS_2 FETs with the subthreshold swing approaching the theoretical limit of 60 mV dec^{-1} at room temperature for metal–oxide–semiconductor field-effect transistors (MOSFETs).

5.2 Monolayer MoS_2 preparation and characterization

Monolayer MoS_2 flakes were produced by repeated splitting of MoS_2 crystals by a mechanical cleavage method, and subsequently transferred to degenerately doped silicon substrates covered with a 290 nm-thick thermal oxide layer [1, 104]. An optical microscope was used to identify monolayer (and few-layer) MoS_2 samples, which were further characterized by non-contact mode atomic force microscopy (AFM) and Raman spectroscopy. Figure 5.1a shows an atomic force microscopy (AFM) image of a typical monolayer MoS_2. From a line scan of the AFM image (Figure 5.1b), we estimate that the MoS_2 sample is ~ 0.7 nm thick, corresponding to a single layer [106, 108]. Raman Spectra were collected using a Jobin–Yvon Horiba Triax 550 spectrometer, a liquid-nitrogen cooled charge-coupled device (CCD) detector, an Olympus model BX41 microscope with a 100 × objective, and a Modu-Laser (Stellar-Pro-L) Argon-ion laser operating at 514.5 nm. The laser spot size was ~ 1 μm in diameter and the laser power at the sample was maintained at low level (~ 200 μW) to avoid any heating effect. The Raman spectrum of the sample shows two peaks at 383.5 cm^{-1} and 403 cm^{-1} (figure 1c), which can be associated with the in-plane E^1_{2g} and out-of-plane A_{1g} vibrations of a monolayer MoS_2, respectively [111].

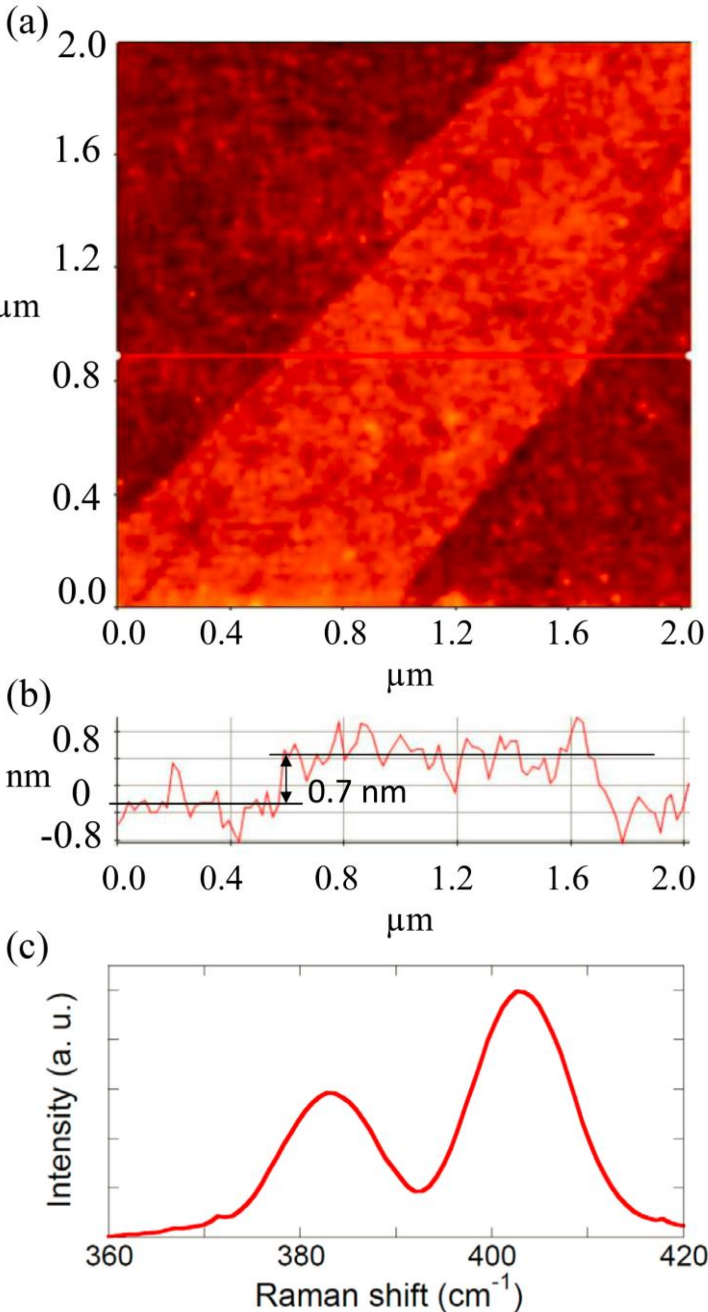

Figure 5.1 (a) AFM image of a monolayer MoS_2 sample deposited on SiO_2 surface. (b) Line profile of the MoS_2 sample in (a). (c) A Raman spectrum of the same MoS_2 sample.

FET devices of monolayer MoS_2 were fabricated using standard electron beam lithography and electron beam deposition of 5 nm of Ti and 50 nm of Au [7]. A PE was

prepared in air by dissolving PEO and $LiClO_4$ in the 8:1 weight ratio in de-ionized water, and then drop casted onto the MoS_2 devices, where the PE gate electrodes were simultaneously patterned on the substrate along with the drain and source electrodes [9]. The PE-electrode was kept very close to the device channel; and the coverage of the PE was also limited to within an area of less than 100 μm around the channel and PE-electrode. Figure 5.2a shows a micrograph of a typical MoS_2 device with schematically illustrated PE. Electrical properties of the devices were measured by a Keithley 4200 semiconductor parameter analyzer in vacuum (~1 $\times 10^{-6}$ Torr) and at room temperature (unless otherwise specified) both before and after adding the PE. The electrical measurements were conducted in both the Si back gate (with or without PE) and PE-gate configurations. As schematically shown in Figure 5.4a, when a positive (negative) voltage is applied to a PE-gate-electrode near the device channel, negative(positive) and positive (negative) ions in the PE accumulate on the gate electrode and channel, respectively, forming electric double layers (EDL) at their interfaces with the electrolyte [112].

5.3 Results and discussions

5.3.1 Mobility enhancement and possible mechanism

We first measured the electrical properties of several monolayer MoS_2 FET devices without PE and found a consistently low mobility between 0.1 and 1.5 $cm^2V^{-1}S^{-1}$, which is in agreement with the values reported in the literature [104, 105, 113]. Upon adding the PE, a significant mobility increase is observed in all devices. Figure 5.2b shows the low-bias linear conductivity defined as $\sigma = L/W \times I_{ds}/V_{ds}$ versus back gate voltage in a typical monolayer MoS_2 device (device A) before and after adding the PE layer. Here L, W, I_{ds}, and V_{ds} are the channel

length (5.9 μm), channel width (0.6 μm), drain-source current, and drain-source voltage, respectively. The field-effect mobility estimated from the linear region of the transfer characteristics of the device using the formula $\mu = \Delta\sigma/(C_{bg}\Delta V_g)$ before and after adding the PE is ~0.1 $cm^2V^{-1}s^{-1}$ and ~ 150 $cm^2V^{-1}s^{-1}$, respectively. Here $C_{bg} = 1.2 \times 10^{-8}$ F cm^{-2} is the capacitance between the channel and the back gate per unit area ($C_{bg} = \varepsilon_0 \varepsilon_r/d$; $\varepsilon_r = 3.9$; d = 290 nm). Similar mobility improvement has been observed in monolayer MoS_2 FETs by Radisavljevic *et al.* upon depositing a thin layer of HfO_2 on top, which was attributed to the suppression of the Coulomb scattering due the high-κ dielectric environment and modification of phonon dispersion in MoS_2 monolayer [108]. However, the dielectric constant of the PE ($\varepsilon = 5$) used in this study is much lower than that of HfO_2 [100]. Moreover, the mobility of the devices drops drastically upon cooling below the freezing temperature of the ions in the PE, ruling out dielectric screening as the dominant mechanism responsible for the mobility enhancement in our devices (see Figure 5.3c and detailed discussion below).

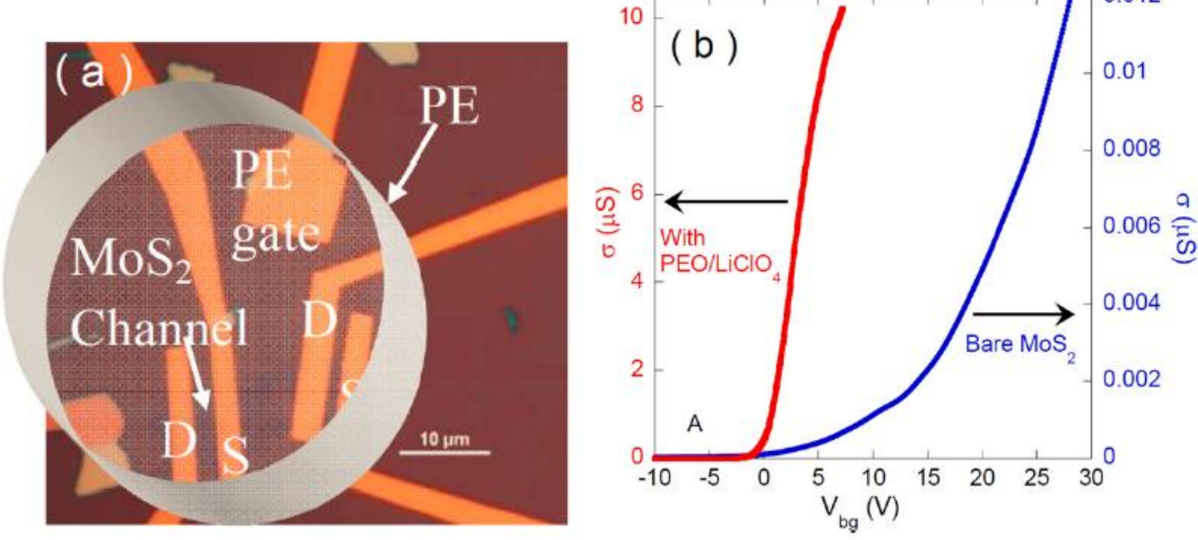

Figure 5.2 (a) An optical micrograph of a typical MoS_2 FET device with schematically sketched PE. (b) Conductivity of a representative MoS_2 FET (device A) measured in the Si-back gate configuration before and after adding the PEO/$LiClO_4$ PE.

A possible mechanism for the field-effect mobility improvement in our devices is the ionic screening effect. At any given back gate voltage, the free counter ions in the PE accumulate on the graphene surface to neutralize the uncorrelated charged impurities [35, 101, 110]. Two orders of magnitude increase of mobility has been previously observed in graphene FETs immersed in ionic solutions, which was attributed to the ionic screening of charged impurity scattering in graphene [101, 110]. Although the PE is expected to introduce additional charged impurities, studies on PE gated carbon nanotube and graphene FETs show that the mobility of these devices remains high (on the order of 10^3 $cm^2V^{-1}s^{-1}$) upon adding PEO/$LiClO_4$ PE [26, 95, 106, 112,]. One likely scenario is that the Li^+ and ClO_4^- ions accumulated on the channel surfaces are correlated in contrast to the uncorrelated initial charged impurities near or on the channel surfaces. Even modest correlations in the position of charged impurities has been shown to substantially increase the mobility in graphene [114]. Therefore, the neutralization of the uncorrelated charged impurities on or near the MoS_2 surface by the counter ions from the PE is likely, at least partially, responsible for the orders of magnitude increase of the mobility upon addition of PE.

A second possibility is that the mobility of our MoS_2 devices without PE is substantially underestimated due to the presence of Schottky barriers at the MoS_2/metal contacts (the contact resistance was not excluded in calculating the mobility). Figure 3a shows the drain-source current (I_{ds}) versus bias voltage (V_{ds}) measured at different back gate voltages for the same MoS_2 device (device A) before depositing the PE. Although the device exhibits linear and symmetric

I_{ds} -V_{ds} dependence at low V_{ds} (Figure 3a inset), the I_{ds} -V_{ds} behavior is non-linear and asymmetric at high bias-voltages. When the drain and source electrode connections are physically exchanged, the I_{ds} -V_{ds} characteristics also change suggesting the presence of asymmetry and possibly non-negligible Schottky barriers at the contacts. It has been recently reported that the current flow in MoS_2 can be largely limited by the contact barriers leading to a significant underestimate of the mobility [109]. Modeling the I_{ds} -V_{ds} characteristics of individual MoS_2 flakes with proper consideration of the contact barriers yields mobility values comparable to the estimated field-effect mobility in our PE-covered monolayer MoS_2 devices as well as that reported in HfO_2-covered MoS_2 devices [108]. Liu *et al.* have further demonstrated that the field-effect mobility of multilayer (~ 20 monolayer) MoS_2 FETs exceeds 500 $cm^2/V{\cdot}s$ due to the smaller bandgap (thus smaller Schottky barrier) compared to monolayer MoS_2 [115]. Therefore, a substantial reduction of the contact barriers is also likely to significantly increase the slope of the transfer characteristics ($d\sigma/dV_g$), leading to a higher estimated field-effect mobility.

5.3.2 MoS_2/metal contact barrier reduction

To shed more light on the origin of the PE-induced mobility enhancement in our MoS_2 FET devices, it is necessary to investigate the respective contributions of the MoS_2/metal contacts and the MoS_2 channel to the total resistance of the device at various gate voltages before and after adding the PE. In Figure 5.3b, we plot the resistances of multiple FETs fabricated on the same monolayer MoS_2 ribbon with uniform width as a function of the channel length before adding the PE, where each resistance value is calculated from the slope of the I_{ds}-V_{ds}

characteristics in the low- bias linear regime as shown in the inset of Figure 5.3a. It is obvious that the resistance increases nearly linearly with the channel length, from which the contact resistance is estimated to be 40 MΩ and 150 MΩ at V_{bg} = 40 and 30 V, respectively. The scattering of data at V_{bg} = 30 V may be due to the contact resistance variation among different devices. The channel resistance for the device with L = 5.9 μm (device A) is several times larger than its contact resistance at all gate voltages, suggesting that the field-effect behavior in our long channel devices is dominated by the channel instead of the contacts. This finding is consistent with that of Radisavljevic *et al* [108]. Upon applying the PE, the low-bias resistance of the device decreases to below 2 MΩ for $V_{bg} > 3$ V as shown in the Figure 3b inset. In the linear region of the transfer characteristics (from which the field-effect mobility is estimated), the total resistance of the device (device A) with PE remains below 7 MΩ, which is significantly lower than either the contact resistance or the channel resistance alone without the PE. This finding shows that covering our single layer MoS_2 FETs with PE not only reduces the channel resistance but also lowers the contact barriers, both of which are critical to improving the field-effect mobility of the MoS_2 FETs. While the improvement of the channel mobility can be attributed to the neutralization of uncorrelated charged impurities, the reduction of the contact barriers could be due to the modification of the metal work function at the contacts by the PE. It has been shown that the adsorption of certain molecules on electrode-metal surfaces can induce a strong decrease in the work function [116]. As our MoS_2 devices are *n*-type, reducing the work function lowers the Schottky barriers at the contacts [109]. Due to the interplay of the variations in the channel mobility enhancement and contact barrier reduction, the resistance of the devices

does not follow the linear dependence on the channel length, making it difficult to accurately extract the contact resistance in MoS_2 devices with PE.

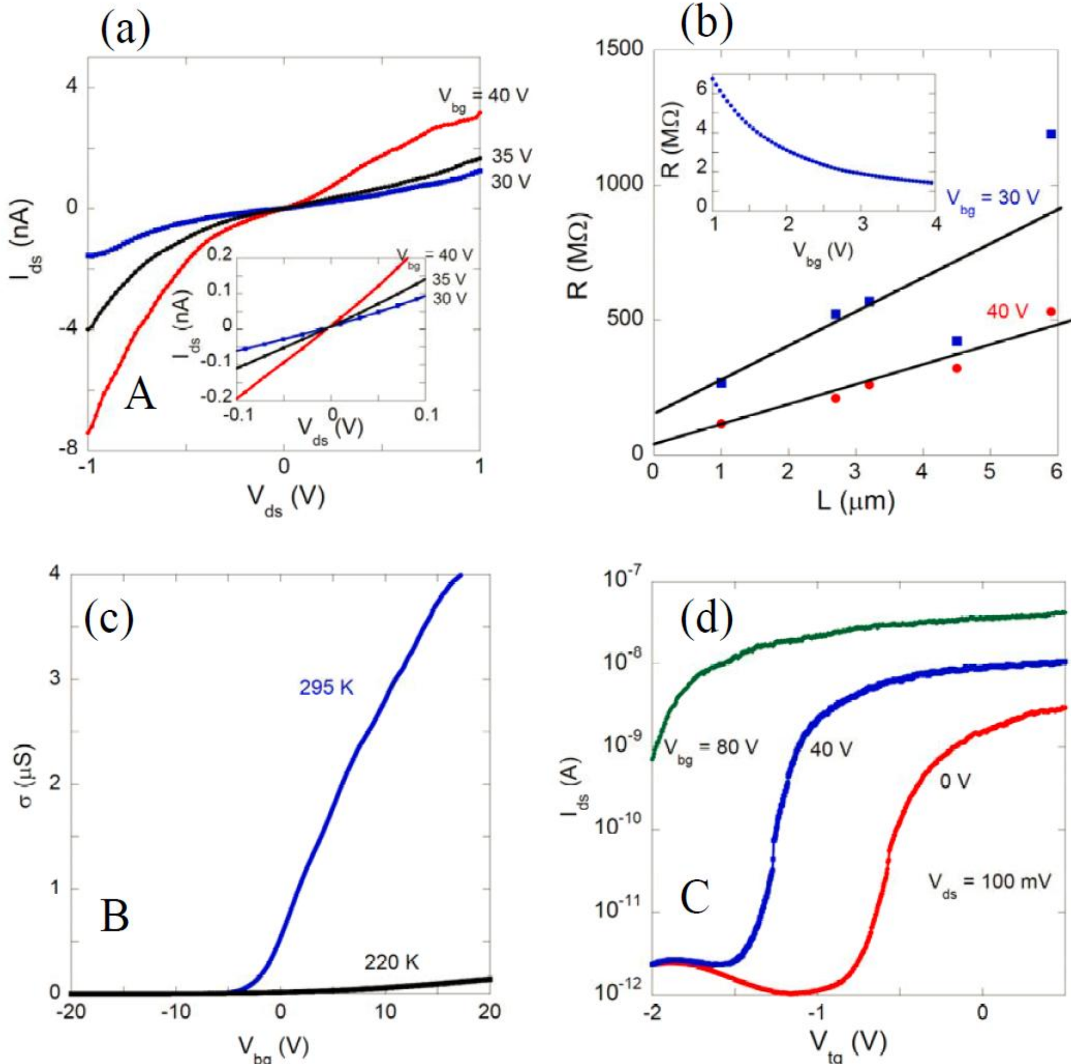

Figure 5.3 (a) Current-voltage characteristics of device A measured at various gate voltages before adding the PEO/$LiClO_4$ PE. (b) Resistance of FET devices fabricated on the same Monolayer MoS_2 (where device A was fabricated) as an function of channel length measured at different back gate voltages. (c) Conductivity as a function of back gate voltage of device B measured at temperatures below and above the freezing temperature of the ions in the PE. (d) Drain-source current versus PE-gate voltage of a MoS_2 FET device (device C) measured at V_{ds} = 100 mV and various back gate voltages. The inset in (a) is the low-bias linear region of (a); and the inset in (b) is the Resistance of device A as a function of back gate voltage after adding the PEO/$LiClO_4$ PE.

Addition of a top dielectric medium has also been shown to increase the back gate capacitance by up to two orders of magnitude in graphene FETs, leading to an overestimation of the mobility when this dramatic capacitance increase was not accounted for [117, 118]. In order to rule out this possibility and further verify that the increase of $d\sigma/dV_g$ upon applying the PE was indeed due to the combined effects of contact resistance reduction and channel mobility increase, we show in Figure 5.3c the transfer characteristics of another monolayer MoS_2 device (device B) measured below and above the freezing temperature of the Li^+ and ClO_4^- ions. The nearly two orders of magnitude lower $d\sigma/dV_g$ (which is proportional to the mobility) at 220 K than at 295 K is likely due to the freezing of both the Li^+ and ClO_4^- ions inside the PEO polymer. Thus they are no longer able to dynamically neutralize the charged impurities on or near the MoS_2 channel as the charged impurities (including those in the SO_2 dielectric) move and redistribute during the back gate voltage sweeps [114, 119]. The dramatic decrease of the mobility below the freezing temperature of Li^+ and ClO_4^- ions eliminates the possibility of overestimating the mobility in PE covered MoS_2 devices due to the dielectric-media-induced capacitance increase. To further rule out the possibility of PE induced capacitance increase as a major cause of the observed mobility increase, we also estimated the back gate capacitance with PE from the drain-source current versus PE-gate voltage (I_{ds}-V_{tg}) measured at different V_{bg} values as shown in Figure 5.3d. When V_{bg} is changed by 40 V, the I_{ds}- V_{tg} curve shifts by 0.7-0.8 V along the V_{tg} axis. Assuming that the PE-gate capacitance (C_{tg}) is ~ 10^{-6} F/cm^2 [112], the back gate capacitance with PE is estimated to be ~ 10^{-8} F/cm^2 (based on $C_{bg} = \Delta V_{tg}/\Delta V_{bg} \times C_{tg}$) consistent with the C_{bg} value without PE, suggesting that the PE does not substantially influence the back gate capacitance.

5.3.3 Gate efficiency improvement

In addition to serving as a contact-barrier reducer and channel-mobility booster, the PE can also be used as a gate material to substantially improve the gate efficiency by taking advantage of the large EDL capacitance at the PE/MoS_2 interface. In order to avoid chemically induced sample degradation, the applied PE-gate voltage was limited to a conservative range, in which the leak current was maintained below 200 pA. The Raman spectra of the single layer MoS_2 before adding the PE and after removing the PE (upon completion of all electrical measurements) are nearly identical, excluding the possibility of electrochemically induced sample degradation. Figure 5.4b shows the transfer characteristic of device B (the same device as in Figure 5.3c) measured in the PE-gate configuration. The overall PE-gate dependence of the drain-source current closely resemble those reported in reference [108], where 30 nm of HfO_2 was used as the top-gate dielectric. The transfer characteristics remain essentially unchanged at different gate voltage sweeping rates. For a drain-source voltage of 300 mV, a current on-off ratio of 10^6 is reached for $-2 < V_{tg} < 0.5$V, and a subthreshold swing (S) of ~ 62 mV/decade is obtained. This S value is notably smaller than the S = 74 mV/decade reported in reference [108], and approaches the theoretical limit of 60 mV/decade, indicating that the gate efficiency of our PE-gated MoS_2 device is close to 1. Such large gate efficiency can be attributed to the large EDL capacitance of the PE. The near ideal subthreshold swing along with the strongly linear dependence of I_{ds} on V_{ds} at various top-gate voltages (Figure 4b inset) further suggests that the PE reduces the Schottky barriers to nearly ohmic [120].

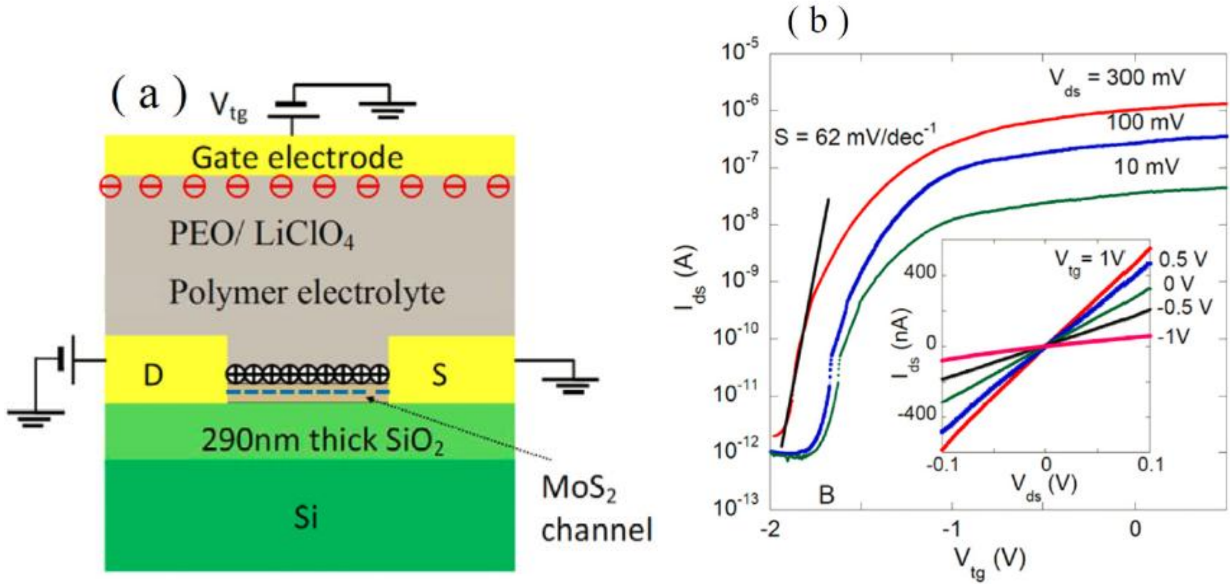

Figure 5.4 (a) A schematic illustration of the working principle of PE-gated MoS_2 FETs. (b) Drain-source current versus PE-gate voltage of a Monolayer MoS_2 FET device (device B) measured at different drain-source voltages. The inset shows the current-voltage characteristics at different PE gate voltages.

5.4 Summary

The high mobility and high gate-efficiency monolayer MoS_2 FETs by simply adding PEO/$LiClO_4$ PE on top of the devices were fabricated. A channel-length dependent study of the device characteristics suggests that the over 10^3 time mobility increase upon adding the PE is due partially to the reduction of contact resistance and partially to the enhancement of channel mobility by the PE. We have also demonstrated excellent device performance with a nearly ideal subthreshhold swing (~ 60 mV/decade at room temperature) and an on/off ratio of 10^6 in PE-gated devices.

CHAPTER 6

AMBIPOLAR FIELD EFFECT TRANSISTORS OF ATOMICALLY THIN MoS_2 WITH IONIC LIQUID

6.1 Introduction

As described in chapter 5, MoS_2 has a bandgap that changes from an indirect gap of ~ 1.3 eV in bulk (or many-layer films) to a direct gap of ~1.8 eV in a monolayer of S-Mo-S [103, 121]. Similar to graphene, atomic layers of S-Mo-S unites can also be extracted from bulk MoS_2 crystals by a mechanical cleavage technique due to relatively weak van der Waals interactions between the layers [104]. The recent experimental demonstration of a reasonably high mobility (over 200 $cm^2V^{-1}S^{-1}$ in monolayer and over 500 $cm^2V^{-1}S^{-1}$ in a ~ 15 nm-thick flake of MoS_2), very high ON-OFF current ratio (10^8) and good subthreshold swing (74 mV/decade), in conjunction with the mechanical flexibility of MoS_2 thin films, opens up the possibility of high-performance and low-power flexible electronics [5, 108, 115]. In addition to conventional field-effect transistors (FETs), MoS_2 can also be used in various other applications such as energy harvesting [122, 123] and optoelectronics [113, 124]. One particularly attractive optoelectronic application of MoS_2 is to fabricate light emitting diodes with monolayer MoS_2 p-n junctions, which requires both n- and p-type field-effect doping. As an n-type semiconductor with a relatively large bandgap, it is rather challenging to induce holes by an electric field in MoS_2. Zhang *et. al.* have recently demonstrated ambipolar behavior in ion-liquid (IL) gated MoS_2 thin flakes (> 10 nm thick) by taking advantage of the extremely large electric double layer (EDL)

capacitance at the MoS_2/IL interface [125]. While this is a significant achievement, the observed On-Off ratio is less than 10^3 and the subthreshold swing is far from ideal, primarily due to the relatively large OFF-current passing through the interior of the crystal beneath the channel surface. To the best of our knowledge, ambipolar behavior in few-layer (1-3 layers) MoS_2 devices has not been reported.

In this work, the first realization of few-layer MoS_2 ambipolar FETs using an IL gate was reported. A record high On-Off ratio of greater than 10^6 for hole transport is observed in our bilayer MoS_2 device; while that for electrons is over 10^7 , close to the values reported in MoS_2 devices with a high-κ gate medium [108, 115]. A nearly ideal gate-channel coupling is also achieved in the IL-gate MoS_2 devices with the subthreshold swing approaching the theoretical limit for MOSFETs (47mV/dec at 230 K). Furthermore, the scaled transconductance of our devices exceeds the highest value in conventional top-gated MoS_2 FETs to date [108, 115].

6.2 Experimental details

Few-layer MoS_2 flakes were produced by repeated splitting of MoS_2 crystals by a mechanical cleavage method, and subsequently transferred to degenerately doped silicon substrates covered with a 290 nm-thick thermal oxide layer [1, 104]. An optical microscope was used to identify few-layer (1-3 layers) MoS_2 samples, which were further characterized by non-contact mode atomic force microscopy (AFM). A thickness of 0.6 - 0.8, 1.3 - 1.5, and 1.9 -2.1 nm measured by AFM is associated to monolayer, bilayer and trilayer, respectively. FET devices of few-layer MoS_2 were fabricated using standard electron beam lithography and electron beam deposition of 5 nm of Ti and 50 nm of Au [7]. A small droplet of IL named

DEME-TFSI (Sigma Aldrich 727679) was applied onto the devices, covering the MoS_2 and the IL-gate electrode that was simultaneously patterned on the substrate along with the drain and source electrodes [9].

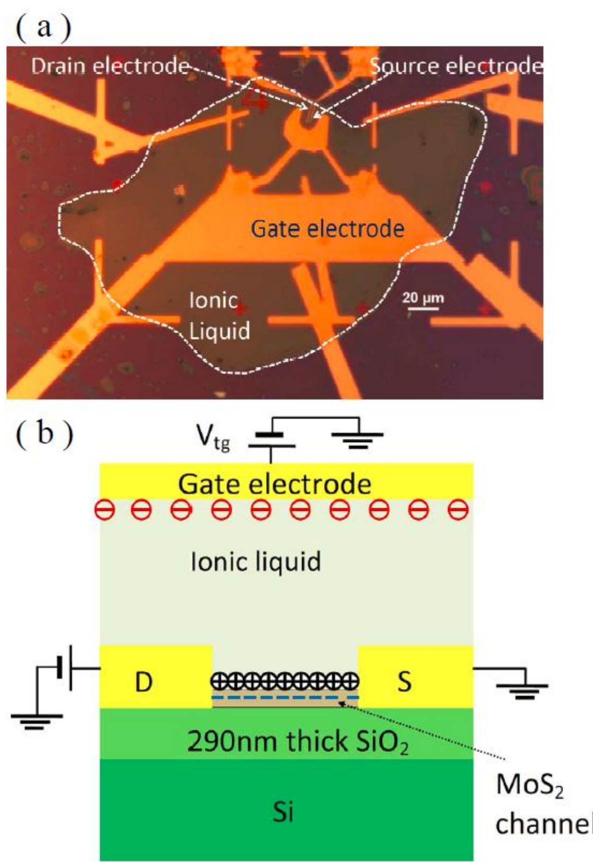

Figure 6.1 IL- gated MoS_2 FETs. (a) Optical micrograph of an actual device. The contour of the IL drop covering the MoS_2 channel and the in-plane gate-electrode is marked by white dotted lines. The white scale bar is 20 μm. (b) A schematic illustration of the working principle of IL-gated MoS_2 FETs.

Figure 6.1(a) shows a micrograph of a typical IL-gated MoS_2 device. Electrical properties of the devices were measured by a Keithley 4200 semiconductor parameter analyzer

in a Lakeshore Cryogenic probe station after dehydrating the IL in vacuum (~1 $\times 10^{-6}$ Torr) for 48 hours. Thoroughly removing the remaining moisture prevents the formation of chemically reactive protons and hydroxyls by the electrolysis of water. All measurements on IL-gated devices were carried out at 230 K to further reduce the possibility of any chemical reaction between IL and MoS_2 [125]. As schematically shown in figure 1b, when a positive (negative) voltage is applied to the IL-gate-electrode near the device channel, negative (positive) and positive (negative) ions in the IL accumulate on the gate electrode and MoS_2 channel, respectively, forming EDLs at their interfaces with the IL [112].

6.3 Results and discussions

6.3.1 Ambipolar behavior with ionic liquid

We have measured the device characteristics of several bilayer and trilayer MoS_2 FETs and consistently observed ambiplar behavior with high On-Off ratios. Figure 6.2 shows the transfer characteristics of a typical IL-gated bilayer MoS_2 ambipolar FET with a channel width of W =1.6 μm and a channel length of L = 1.0 nm. For a drain-source voltage of 1V, the On/Off ratio for the hole channel is over 10^6, the highest value reported for hole transport in MoS_2 FETs, while that for the electron channel exceeds 10^7 comparing well with MoS_2 devices using HfO_2 and Al_2O_3 gate dielectrics (Figure 6.2a) [108, 115, 125]. The significantly higher ON-Off ratio in our bilayer MoS_2 device in comparison with IL-gated many-layer MoS_2 devices can be attributed partially to the reduced channel thickness and partially to the increase band gap (from ~ 1.3 eV in bulk or many-layers to ~ 1.6 eV in bilayer MoS_2) [121, 125]. The slightly lower On/Off ratio in the hole channel than in the electron channel is likely caused by the higher

Schottky barrier for holes than for electrons. From the transfer characteristics, a subthreshold swing of S = d (log I_{ds})/dV_{tg} ~ 47 mV/decade can be deduced. This value approaches the theoretical limit for MOSFETs as determined by $S = (kT/e)$ ln10 at T = 230 K (k is the Boltzmann constant), indicating that the gate efficiency of our IL-gated MoS_2 device is close to 1 primarily due to the large capacitance of the EDL. The transfer curves are also highly reproducible indicating that the present device accumulates charge only electrostatically. In addition, the gate-source current remains nearly constant and low (~ 100 pA) for the measured IL-gate range of -3.5 to 1 V, further ruling out the possibility of ionic charge transfer or any chemical reactions at the MoS_2/IL interface [126].

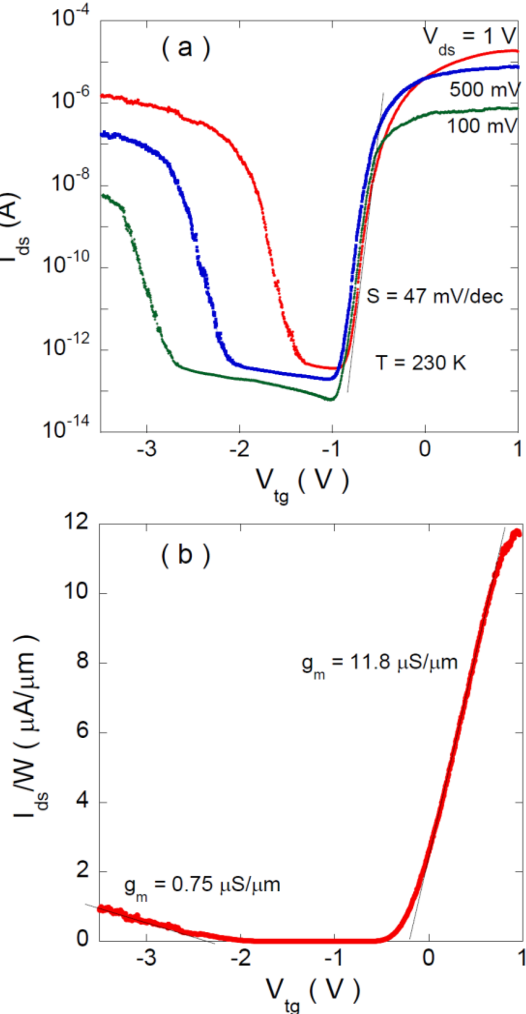

Figure 6.2 Transfer characteristics of a bilayer MoS_2 IL-gated FET (W= 1.6 μm and L = 1 μm). (a) Logarithmic plot of drain-source current versus IL-gate voltage measured at various drain-source voltages and T= 230 K. (b) Linear plot of the scaled drain-source as a function gate voltage for V_{ds} = 1 V.

As shown in Figure 6.2b, the maximal scaled On-current (defined as I_{ds}/W) at V_{ds} = 1V and V_{tg} = 1 is 11.8 μA/ μm, several times higher than that of the top-gated monolayer MoS_2 FETs with HfO_2 gate dielectric [108] and two orders of magnitude higher than that of MoS_2 thin-flake devices with Al_2O_3 gate dielectric [115]. The higher scaled On-current in our bilayer MoS_2 device can be at least partially attributed to the self-aligned IL-gate structure in contrast to the

conventional non-self-aligned top-gate structure. The former modulates the carrier density in the entire channel, while the latter only modulates the part of the channel directly beneath. The scaled transconductance defined as $g_m = 1/W \times dI_{ds}/dV_{tg}$, is ~ 11.8 μS/ μm at V_{ds} = 1 V, an order of magnitude higher than in top-gated monolayer MoS_2 devices (1μS/ μm) [108]. Such a high scaled transconductance can be attributed to the high capacitance of the EDL at the MoS_2/IL interface in addition to the self-aligned IL-gate structure. The field-effect mobility estimated from the scaled transconductance of the device using the formula $\mu = L \times g_m / (C_{tg} V_{ds})$ is ~1.5 $cm^2V^{-1}S^{-1}$ and ~ 0.15 $cm^2V^{-1}S^{-1}$ for electrons and holes, respectively. Here the EDL capacitance, C_{tg}, is assumed to be 7.2 $\mu C/cm^2$ and 4.7 $\mu C/cm^2$ for electron and holes, respectively based on reference [125]. It is worth noting that the mobility values derived here are the lower limit due to the non-negligible contact resistance and the possible overestimate of the EDL capacitance. In particular, the substantially lower mobility for holes than for electrons is mostly likely due to the higher contact barrier for holes than for electrons. The EDL capacitance consists of the electrostatic (C_e) capacitance and quantum capacitance (C_q) of the MoS_2 channel connected in series ($1/C_{tg} = 1/C_e + 1/C_q$). Since the electrostatic capacitance of the EDL for DEME-TFSI IL is extremely high (can reach as high as 100 $\mu C/cm^2$), the total EDL capacitance of MoS_2 FETs (*e.g.* 7.2 $\mu C/cm^2$ for electrons in IL-gated many-layer MoS_2) is likely dominated by C_q [127]. The quantum capacitance in our bilayer MoS_2 may be lower than in the many-layer MoS_2 in reference [103, 125]. Therefore, the actual mobility in our bilayer MoS_2 device is likely significantly higher. However, more accurate value of the EDL capacitance will be needed for calculating the field-effect mobility in our MoS_2 devices, which is beyond the scope of this work.

6.3.2 I_{ds} *vs.* V_{ds} characteristics

Figure 6.3 shows a comparison of the output characteristics of the same device measured in both the back-gate configuration (before depositing IL) and IL top-gate configuration. As shown in Figure 6.3a, the I_{ds} versus V_{ds} at various back-gate voltages before depositing IL are non-linear suggesting the presence of significant Schottky barrier without IL. After depositing the IL, the drain-source current versus drain-source voltage (I_{ds} vs. V_{ds}) curves for the electron channel become nearly linear at low bias voltages and start to saturate at higher bias voltages (Figure 6.3b). In addition, the overall current also increases by more than an order of magnitude. Both changes suggest that the contacts become more Ohmic after depositing the IL onto the device. A likely scenario is that the adsorption of the IL at or near the channel-metal contacts changes the metal work function and thus modulates the barriers for charge carriers [120]. In addition, the contact barrier should also become more transparent as the depletion layer width decreases due to the highly efficient band bending induced by the EDL [128].

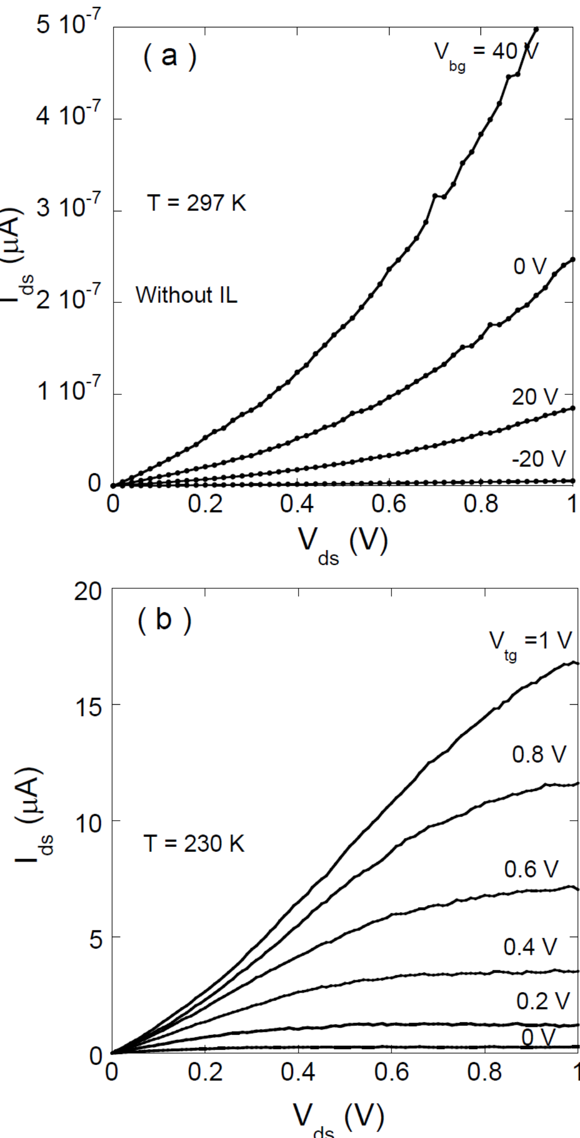

Figure 6.3 Comparison of the output characteristics of the same bilayer MoS_2 device in Figure 6.2 before and after depositing IL. (a) I_{ds} vs. V_{ds} with back-gate voltage stepped from 40 to -20 V before depositing the IL drop. (b) I_{ds} vs. V_{ds} by stepping the IL-gate voltage from 1 to 0 V.

6.4 Summary

In conclusion, we fabricated ambipolar few-layer MoS_2 FETs with excellent device characteristics using an IL as the gate material. In particular, the On/Off ratio in our bilayer MoS_2 devices exceeds 10^7 for electrons and 10^6 for holes demonstrating orders of magnitude improvement over many-layer MoS_2 devices reported in reference [125]. Near ideal switching and high scaled transconductance are also achieved in our devices due to the very large EDL capacitance at the interface of the gate material and MoS_2 channel. This work may pave the way for further studies into the physics and application of the ambipolar transport of atomically thin MoS_2 such as light emitting p-n junctions and extremely low-power inter-band tunnel FETs in monolayer MoS_2.

CHAPTER 7

CONCLUSION

The main theme of this work is focused on how to create the adequate energy gap together with fundamental study of physical properties for graphene and graphene nanoribbon using semiconductor processing techniques, which expectedly can be applicable to electronic devices. By utilizing the same techniques developed in this work, other 2D materials can be extensively explored in the future. As described in the previous chapters, graphene is a promising material with respect to stiffness, mobility and other properties to be a candidate of substituting the current Si-based semiconductor technology, but no gap. A great deal of effort was put into this study to engineer the energy gap, which was literally corresponding to the intrinsic bandgap for graphene nanoribbon. Besides, 2D materials were also investigated at the same time to figure out the fundamental physical properties and dig out which one will be best candidate for next generation of applications.

Therefore, the electrical transport measurements on a suspended ultra-low-disorder graphene nanoribbon (GNR) with nearly atomically smooth edges that revealed a high mobility exceeding 3000 cm^2 V^{-1} s^{-1} and an intrinsic bandgap was reported in this study. The experimentally derived bandgap is in *quantitative* agreement with the results of our electronic-structure calculations on chiral GNRs with comparable width taking into account the electron-electron interactions, indicating that the origin of the bandgap in non-armchair GNRs is partially due to the magnetic zigzag edges. In addition, suspended few layer (1-3 layers) graphene

nanoribbon field effect transistors from unzipped multiwall carbon nanotubes have been fabricated. Electrical transport measurements show that current-annealing effectively removes the impurities on the suspended graphene nanoribbons, uncovering the intrinsic ambipolar transfer characteristic of graphene. Further increasing the annealing current creates a narrow constriction in the ribbon, leading to the formation of a large band-gap and subsequent high on/off ratio (which can exceed 10^4). Such fabricated devices are thermally and mechanically stable: repeated thermal cycling has little effect on their electrical properties. This work shows for the first time that ambipolar field effect characteristics and high on/off ratios at room temperature can be achieved in relatively wide graphene nanoribbon (15 nm ~50 nm) by controlled current annealing.

Moreover, a simple one-stage solution-based method was developed to produce graphene nanoribbons by sonicating graphite powder in organic solutions with polymer surfactant. The graphene nanoribbons were deposited on silicon substrate, and characterized by Raman spectroscopy and atomic force microscopy. Single-layer and few-layer graphene nanoribbons with a width ranging from sub-10 nm to tens of nm and length ranging from hundreds of nm to 1 μm were routinely observed. Electrical transport properties of individual graphene nanoribbons were measured in both the back-gate and polymer-electrolyte top-gate configurations. The mobility of the graphene nanoribbons was found to be over an order of magnitude higher when measured in the latter than in the former configuration (without the polymer electrolyte), which can be attributed to the screening of the charged impurities by the counter-ions in the polymer electrolyte. This finding suggests that the charge transport in these solution-produced graphene nanoribbons is largely limited by charged impurity scattering.

We also report electrical characterization of monolayer molybdenum disulfide (MoS_2) devices using a thin layer of polymer electrolyte consisting of poly (ethylene oxide) (PEO) and lithium perchlorate ($LiClO_4$) as both a contact-barrier reducer and channel mobility booster. We find that bare MoS_2 devices (without polymer electrolyte) fabricated on Si/SiO_2 have low channel mobility and large contact resistance, both of which severely limit the field-effect mobility of the devices. A thin layer of PEO/$LiClO_4$ deposited on top of the devices not only substantially reduces the contact resistance but also boost the channel mobility, leading up to three-orders-of-magnitude enhancement of the field-effect mobility of the device. When the polymer electrolyte is used as a gate medium, the MoS_2 field-effect transistors exhibit excellent device characteristics such as a near ideal subthreshold swing and an on/off ratio of 10^6 as a result of the strong gate-channel coupling. In addition, the ambipolar field-effect transistors of atomically thin MoS_2 with an ionic liquid gate were realized in this study. A record high On/Off current ratio greater than 10^6 is achieved for hole transport in a bilayer MoS_2 transistor, while that for electron transport exceeds 10^7. The scaled transconductance of the device reaches 11.8 μS/μm at a drain-source voltage of 1V, which is an order of magnitude large than that observed in MoS_2 transistors with a high-κ top-gate dielectric. A near ideal subthreshold swing of 47mV/dec at 230 K is also achieved in the bilayer MoS_2 device.

Actually, the mobility and bandgap are the most important two key indicators corresponding to the impurities and edge structure in graphene nanoribbon. The gap opens in graphene nanoribbon, which is inversely proportional to the ribbon width. The attempts have been conducted for electrical property associated with the observation of edge structure by using TEM and STM/STS. Unfortunately, these trials might not turn out very successful due to the

difficulties of sample preparation encountered in this work as detail shown in the appendix A. For example, the sample needs to be conducting and ultraclean when measuring STM/STS at Oak Ridge National Laboratory. Similarly, it is also difficult to transfer the GNRs to Cu grid, making it unattainable to observe the edge structure through TEM. How to make the TEM or STM/STS sample of GNRs for observation correlated with electrical properties leaves a tough issue for studying graphene nanoribbons in the future. Some additional characterization work done in this study will be shown in the appendix B. In addition, the 2D materials beyond graphene are now attracting more interests in the world. Which one will be the candidate for next generation of electronics? It still needs a great myriad of research and study for unveiling their fundamental physical properties and applications.

APPENDIX A

There are still some challenges and issues with respect to the device fabrication. To complete the GNRs and other 2D materials devices before electric measurement, there are several processes involved here, including GNRs synthesis, electron beam lithography, metal deposition, HF etching for suspension, thermal annealing, and so on. Each process has its own uniqueness which sometimes the difficulties and issues are generated associated with the operation and even the equipment itself. Some problems are commonly encountered in doing general experiment, but some are not easily being solved during processing. It is worth pointing out some issues existing in this work, which needs much time to figure out and definitely affects the final results. The process of electron beam lithography and HF etching for GNRs suspension are the most critical in fabricating GNR-FET devices. In the mean time, thermal annealing process is considered as tortuous one to cause the high failure of suspended devices. Over 50% survived rate can be reached to have GNR-FET devices ready for further measurement after thermal annealing when each process runs smoothly without any anomaly or miss operation.

A.1 Sample preparation

In order to have excellent devices for studying physical properties, it is important to get the good samples through feasible processes in the beginning. Sample preparation plays a critical role in studying fundamental physics no matter it is related to devices fabrication or characterization aspects. For example, if there were no good graphene nanoribbon samples produced by appropriate approach with expected width 10~30 nm, it definitely would not have

chances to probe the intrinsic physical properties. Similarly, it would not have good SEM/TEM images if sample was not prepared adequately for observation. In the following sections, the sample preparation for graphene nanoribbons and single layer of MoS_2 will be described in more details. Besides, the transfer of CVD grown MoS_2 on sapphire to Si/SiO_2 substrate will be shown in this section.

A.1.1 Graphene nanoribbons

The GNRs used in this study are synthesized by unzipping high quality multiwall carbon nanotubes following a method developed by Dai's group [23]. First, the multiwall carbon nanotubes were calcined in the furnace at 500^0 C for 2 hours to remove the impurities without oxidizing the sidewalls. Then, the GNRs were produced by sonicating mildly-oxidized multiwall carbon nanotubes (MWNT) in a 1,2-dichloroethane (DCE) solution of poly(m-phenylenevinylene-co 2, 5-diy octocy- p-phenylenevinglene) (PmPV), where the PmPV is used as a surfactant to stabilize the unzipped GNRs in solution. The solution was then centrifuged at 15000 rpm (Fisher Scientific Marathon 26kmr centrifuge) for 1 hr to remove aggregates and some of the remaining MWNTs; and a supernatant containing nanoribbons and remaining MWCTs was obtained. Sometimes, the supernatant has to be split into 6 small tubes one more time to get higher yield GNRs with less CNTs. Next, the GNR samples from the supernatant were deposited on degenerately doped Si substrates with 290 nm of thermal oxide, and subsequently non-contact mode AFM (Park System XE-70) was used to locate individual GNRs with respect to the prefabricated Au alignment marks and to characterize their thickness, width and length. The GNRs produced from this method mostly consist of 1-3 layers. Figure A.1

shows the chemical solutions after sonication and centrifuge, followed by the Si substrate soaking in the solution for 30 min. Then, the high quality GNRs with a range of 10~50 nm wide can be identified under AFM scanning as shown in the images.

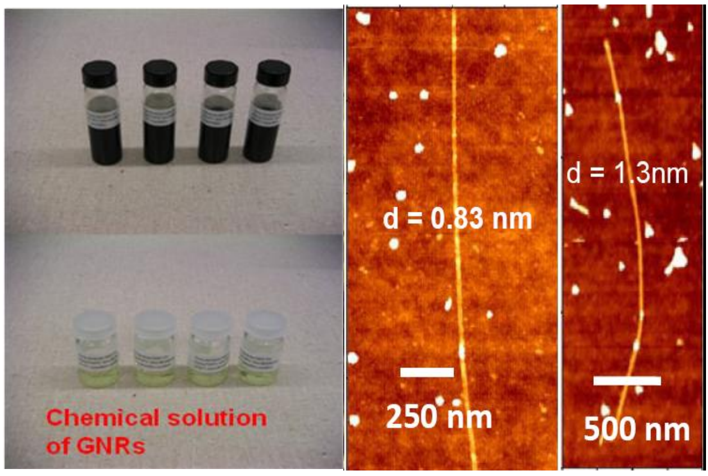

Figure A.1 The left pictures indicate the chemical solution of GNRs after sonication and centrifuge. On the right are the AFM images illustrating the GNRs on Si/SiO_2 substrate.

A.1.2 MoS_2 monolayer/multilayer

Similar to graphene, monolayer MoS_2 flakes were produced by repeated splitting of MoS_2 crystals by a mechanical cleavage method using adhesive blue tape, and subsequently transferred to degenerately doped silicon substrates covered with a 290 nm-thick thermal oxide layer [1, 104]. An optical microscope was used to identify monolayer (and few-layer) MoS_2 samples, which were further characterized by non-contact mode atomic force microscopy (AFM). Figure A.2 shows the optical micrograph corresponding to an atomic force microscopy (AFM) image of a typical monolayer MoS_2. From the average scan of AFM image {Figure A.2

(b)}, we estimate that the MoS_2 sample is ~ 0.8 nm thick, corresponding to a single layer [106, 108].

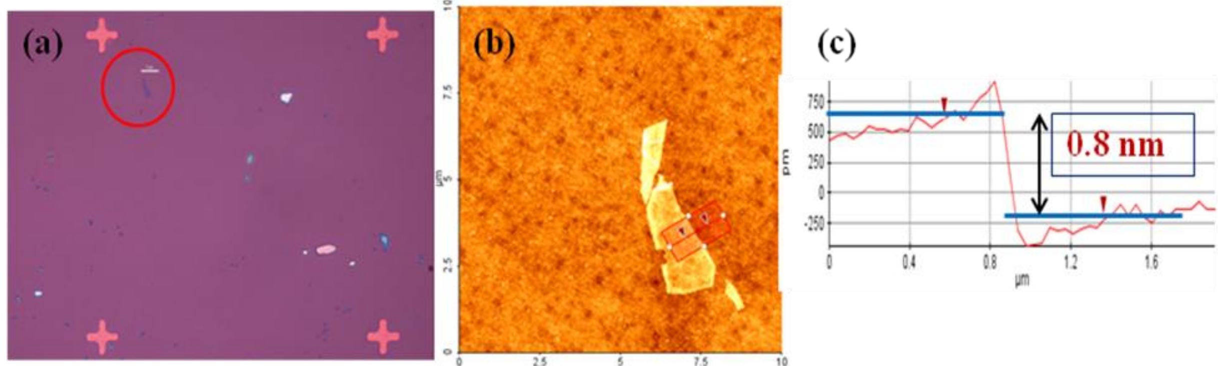

Figure A.2 (a) The micrograph shows MoS_2 flake is identified by optical microscope with light blue color. (b), (c) AFM scanning further verifies the dimensions of this flake with the thickness ~0.8 nm as monolayer of MoS_2.

A.1.3 CVD grown MoS_2

In order to have larger area materials on the substrate for application except the mechanical exfoliation from crystals, several research groups has started growing 2D materials on certain substrates using chemical approach (CVD) just like CVD grown graphene. However, unlike CVD graphene is grown on transition metals like Cu or Ni, which can be easily etched off the metals underneath and transferred to Si/SiO_2 substrate, though there is still some treatment needed to have high quality graphene. The MoS_2 grows on insulating sapphire substrate, making it difficult to fabricate the devices for measuring the electrical properties using standard e-beam lithography. Several attempts have been done for having electrodes directly on the sapphire substrate using e-beam lithography, including sandwich approach (PMMA + Au + HSQ) or Ar plasma etching. However, it did not show the positive electrical results, possibly caused by the

randomly selected area which had not been covered by MoS_2 film. This could be verified in AFM images with non-uniform MoS_2 on the substrate.

Therefore, transferring CVD grown MoS_2 onto Si/SiO_2 substrate will be the feasible way followed by subsequent current processes to be able to fabricate the devices. Followed by the transfer process developed by other group, a layer of PMMA was coated on the CVD grown MoS_2 and baked for 10 minutes at 100^0C. Then, this substrate would be placed into prepared 2M NaOH solution for 20 minutes at 95^0C. The thermal release tape was cut to fit the substrate and pressed the tape on the substrate using an eraser. Slightly and slowly peeled off the thermal release tape from the substrate and rinsed with water. Next, this tape was put on Si/SiO_2 substrate, and used the same skill as previous one. Finally, the thermal release tape could be easily removed at 100^0C and MoS_2 single layer or multi-layer would be remained on Si/SiO_2 substrate.

A.2 E-beam lithography

Except photo lithography most used widely in semiconductor industry, there were several lithography methods developed in the past few decades such as X-ray lithography, ion beam lithography and electron beam lithography (e-beam). Since the diffraction limit has been an issue for photo lithography in current semiconductor technology node down below 90 nm, an alternative approach has been always sought as a substitute. E-beam lithography seems to provide appropriate way using electron as a source for making smaller feature size structures regarding feasibility and resolution. Although slow speed and little costly are the drawbacks for e-beam lithography system, it has already been commonly used in writing masks for the use of

photo lithography in semiconductor industry. In this study, e-beam lithography plays a critical part for making devices no matter in GNRs or 2D materials.

It is necessary to fabricate the electrodes connected to samples for further electrical measurements, which the standard e-beam lithography is used in this study including SEM (Hitachi S-2400) with 25kV and Nano Pattern Generating System (NPGS) software to control the electron beam. The configuration of whole system is shown in Figure A.3 (left). NPGS software is used for designing the required nano-patterns (electrodes) and controlling the e-beam to write the patterns as shown in Figure A.3 (right). Several factors determine the high resolution written patterns including SEM, the skill of operating SEM and e-beam resist. Definitely, the resolution of written patterns depends on how well the SEM system is being used. In other words, the better resolution the SEM is, the sharper the written patterns obtain. Another key factor to acquire the high resolution written patterns is the skill of operating SEM system. For example, the experienced people should be more reliable to get higher resolution of SEM for writing patterns.

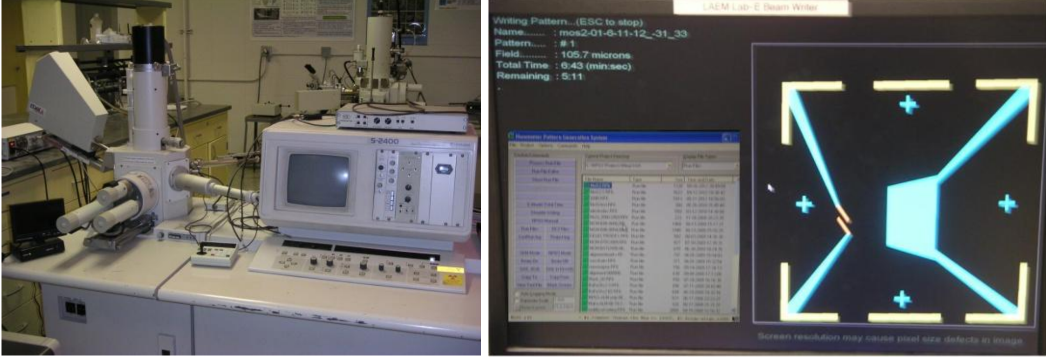

Figure A.3 The configuration of SEM (left) together with NPGS software (right) is used in this work, providing the standard e-beam lithography.

There are two types of the electron resist, positive and negative. Positive resist like polymethylmethacrylate (PMMA) is the most commonly used in e-beam lithography, which is easily removed in the solvent on the exposed areas due to broken cross link of e-beam exposure. Negative resist such as hydrogen silsesquioxane (HSQ) is sometimes used for the protective mask of written electrodes, which shows the opposite way in solvent. In this work, PMMA 495-A4, 950-A2 (different molecular weight) and HSQ are used as e-beam resists for e-beam lithography.

(I) PMMA resist

Firstly, PMMA spin-coated on the pre-soaked GNRs substrate or mechanically exfoliated MoS_2 substrate with the speed of 4000 rpm, followed by 180^0C baking on the hotplate for 5 min after coating of each type. The silver paint, acting as the focus point, has to be cautiously put on the side of mark where the samples are inside. Before doing electron beam lithography, the designed electrodes have to be completely finished and run through off-line of NPGS Designcad software to avoid any error during writing. With careful handling and adjustment of focus and astigmatism for SEM, the designed patterns can be precisely written on the desired areas in required resolution. As mentioned in the previous section, being familiar with the operation of SEM would be one of the most important prerequisites to write the proper patterns for electrodes. The parameters such as dose and current, of course, are critical to write the required patterns. Based on the repeated testing of thickness for PMMA~260 nm with two layers (495A4 and 950 A2), the current keeps around 11.0 pA to write narrower electrodes and the doses are set to be 15nC for line and 260uC/cm^2 for area, respectively. Subsequently followed by developing process using the mixture chemicals of MIBK and MEK with the ratio 30:1 for 70 sec, the

micrographs show the electrodes after developing in Figure A.4 for GNR (a) and MoS_2 (b) samples, respectively.

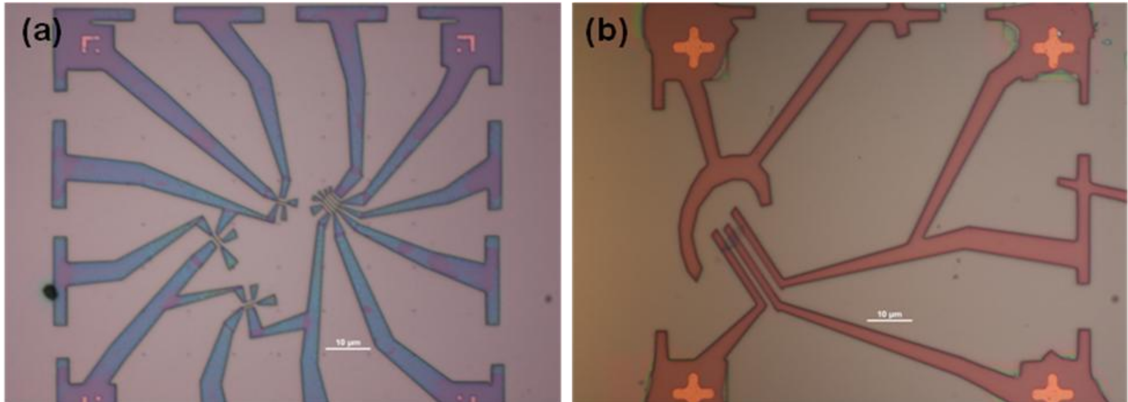

Figure A.4 The electrodes pattern after developing process for (a) GNR and (b) MoS_2 under 1K magnification of optical microscope.

In addition, the adjustment of maximum filament current in S-2400 SEM system is also important to have big enough current writing large patterns and avoid current instability during writing. Focus adjustment on Au particles up to 200K magnification is needed for writing narrower electrodes like GNR samples. The skills of fast adjustment for focus on substrate and reduction of scanning frequency on the samples would be necessary to avoid excessive exposure and guarantee high quality of the patterns. Nevertheless, the more effort had been put in, the higher quality could be gained.

(II) HSQ resist

The HSQ, a negative tone resist, has low viscosity opposite to PMMA and diluted with MIBK. The same procedures as PMMA coating, the speed would be set at 4000 rpm for spin coater, followed by 80^0C baking for 10 minutes with 2% and 6% HSQ, respectively. The area doses ranging from 200uC/cm^2 to 1000uC/cm^2 have been tested for 6% concentration HSQ. It

turned out good patterns with the dose only below 300uC/cm^2. Other testing results for 2% concentration HSQ with different doses for line and area were shown in the following Table A.1. The best condition was then selected as the base line for on-going experiment. In order to develop HSQ after e-beam lithography, CD-26 was used for 30 sec together with few seconds sonication if spread-out occurred sometimes due to step height between patterns or overdosing. The resolution of using HSQ may be not as high as using PMMA due to electron scattering showing more significant in HSQ resist.

←	2% HSQ Area dose	2% HSQ Line dose	→
300 uC/cm^2	Not good	Good	3 nC spacing 200 nm
350 uC/cm^2	OK	Good	4nC spacing 200 nm
400 uC/cm^2	Good	Good	5 nC spacing 200 nm

Table A.1 The testing results of 2% concentration HSQ with different doses for line and area.

In order to go further step for the process consideration as a shadow mask, O_2 plasma treatment with 100W power and 30 sccm flow rate has been implemented on HSQ testing substrate. Unfortunately, the PMMA underneath HSQ collapsed to substrate due to over etching during plasma treatment. Besides, Ar plasma treatment with the same parameters is sometimes used to get rid of the layers like graphene or MoS_2 on substrate. Another intention of using HSQ is to apply to the insulating substrate like sapphire as a shadow mask for defining the active area.

One of approaches is having three layers on the top of substrate as PMMA + Au + HSQ configuration, where Au acts as the conducting layer for e-beam lithography.

A.3 Metal deposition

To have good contacts with GNR and MoS_2 samples, thermal evaporation with one layer of Cr and Au was used to fabricate the devices. The whole set-up of metal deposition is shown as Figure A.5, including chamber, diffusion pump and thickness monitoring of crystal. The principle is using heat generated by large current flowing through the metals, evaporating a thin layer metal atom onto sample surface in high vacuum with thickness monitored by crystal precisely. Some parameters and operation skills are also crucial to this process. For example, the pressure needs to be lower than $2x10^{-6}$ torr for starting deposition process and it will not be up to $5x10^{-6}$ torr during Au deposition. The deposition rates were set to be 0.2Å /s and 1.0Å/s for Cr and Au, respectively. Normally, the required thicknesses of Cr and Au are 0.5 nm and 50 nm in this work. Most of GNR devices were done metal deposition in this tool. In order to make good contact between Cr and sample, Ar gas purge will be conducted before pumping down the chamber to possibly get rid of oxidation of Cr rod.

Figure A.5 The setup of metal thermal evaporator includes chamber, diffusion pump and thickness monitor of crystal.

Actually, this equipment is pumped down to the required pressure using mechanical pump together with diffusion pump. Whenever the liquid nitrogen is used, the pumping efficiency of diffusion pump will be improved from 4 hours to 2 hours. In addition, cleaning up the chamber and sample holder using IPA or acetone after single use definitely increases the pumping speed. It is also necessary to notice the life time of crystal, which is critical to monitor the deposition rate and thickness. Figure A.6 is the schematic diagrams to illustrate the integrated processes with respect to electron beam lithography and metal deposition. In addition, the written electrodes are shown in the bottom after lift-off process using acetone combined with few seconds sonication.

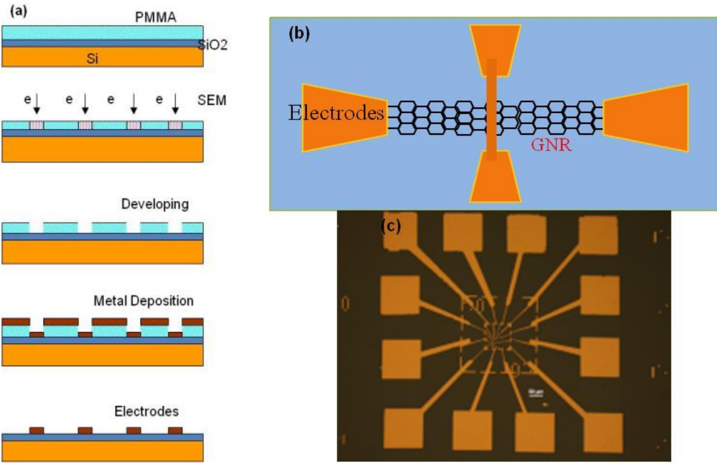

Figure A.6 The schematic diagrams show the integrated processes with electron beam lithography and metal deposition. (a) Starting the coating of PMMA to lift-off process. (b) The schematic top view shows the metal contacts with GNRs. (c) The actual electrodes picture ready for electrical measurement.

Alternatively, a layer of Ti was used as adhesion metal before Au deposition due to Cr generating higher contact resistance in GNR devices possibly caused by oxidation during

deposition or subsequent processing like annealing. The metal deposition was switched to e-beam evaporator not only because of its efficiency, but also its selection of diverse metals. Most of MoS_2 samples were done with a layer of Ti (5 nm, rate 1Å/s) and a layer of Au (50 nm, rate 1Å/s), respectively. Some GNR devices were done metal deposition using this tool as well with Ti (1 nm, rate 1Å/s) and Au (50 nm, rate 1Å/s) combination. The basic principle of e-beam evaporator is similar to that of thermal evaporator except using e-beam with proper frequency and current to hit the targets and get the metal evaporated. It turned out the adhesion of using Ti showing more robust than using Cr for electrical measurement.

A.4 Problems and issues

The most common issue occurred in the electron beam lithography process was the smeared pattern, which could possibly be induced by overdose due to defocus of electron beam or wrong thickness of PMMA. To avoid these problems, careful handling with PMMA coating (both 495A4 and 950A2) at the speed 4000 rpm and being aware of valid date for these chemicals are crucial. In the mean time, putting silver paint around the side of designed pattern which will be written by electron beam is also important. When using SEM (Hitachi S-2400), the focus and astigmatism have to be adjusted to the optimal condition on gold standard sample. Figure A.7 shows the comparison between clear and unclear written patterns by electron beam lithography. In fact, the subsequent processes depend on how good the written pattern is. For example, metal deposition will follow the topography produced by electron beam lithography. Lift-off and etching processes will also rely on the good pattern generated by e-beam lithography.

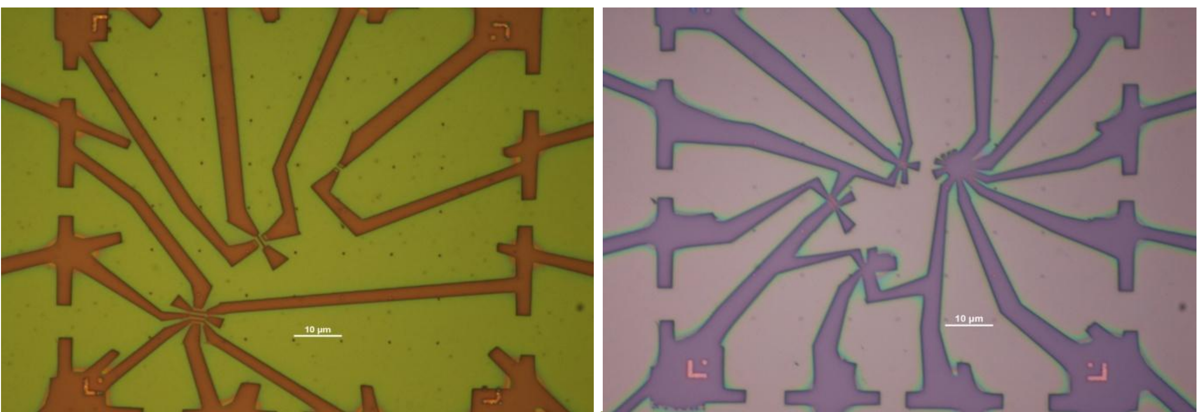

Figure A.7 The comparison between clear (left) and unclear (right) patterns produced by electron beam lithography.

Another issue generated in this process was concerned about the movement of SEM system. Actually, the SEM had been moved to different places twice due to building reconstruction, and the interference pattern occurred in alignment imaging after each movement possibly caused by the bad BNC connection with imaging after movement, leading to the written patterns as rough edges together with those unknown signals. It really took some time to get it fixed after repeated testing and still found no reason. Figure A.8 shows the AFM images of same testing pattern (wheel) before and after SEM moving, clearly indicates the interference wiggling lines appears in the right image which obviously affects the performance of electron beam writing. In the mean time, it provides a good opportunity to verify what could be wrong if the written patterns turned out unsuccessful, and notice the important maintenance of the tool as a good condition.

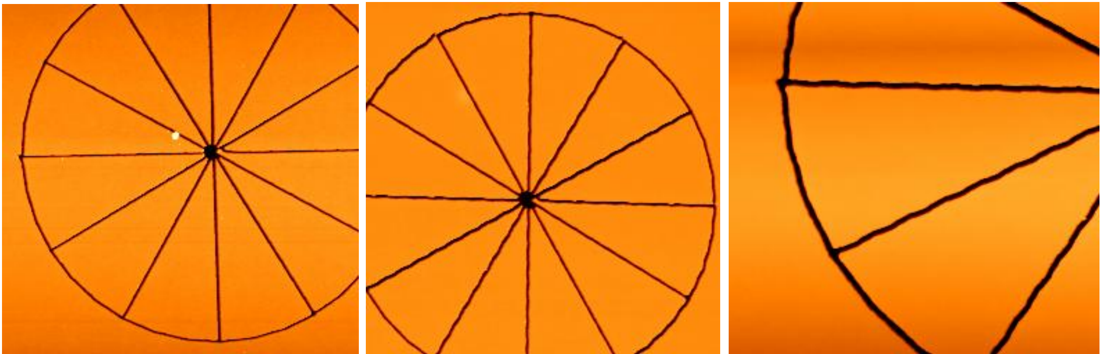

Figure A.8 AFM images show the performance of electron beam writing before and after SEM moving. Left image illustrates clear wheel pattern before moving. Middle image indicates the interference wiggling lines after moving, and zoom in image on the right shows obvious interference from the middle image.

A.5 Etching and annealing processes

Once the FET devices have been fabricated throughout the previous processes, the next harsh process gets into etching by using hydrofluoric acid (HF). Suspension of the GNRs in FET devices is achieved by placing a small drop of 1:6 buffered HF on top of the GNR device for 90 s to etch away approximately 150 nm of the SiO_2 underneath the ribbons [26, 27]. After wet etching, the device was transferred to hot isopropyl alcohol (which has low surface tension) and let try on a 120°C hot plate. Figure A.9 shows a schematic diagram and the atomic force microscopy (AFM) image of a typical suspended GNR device. The line profile of the suspended GNR is shown in Figure A.9 (down), indicating that the ribbon is suspended ~150 nm above the surface of the remaining SiO_2 without noticeable sagging.

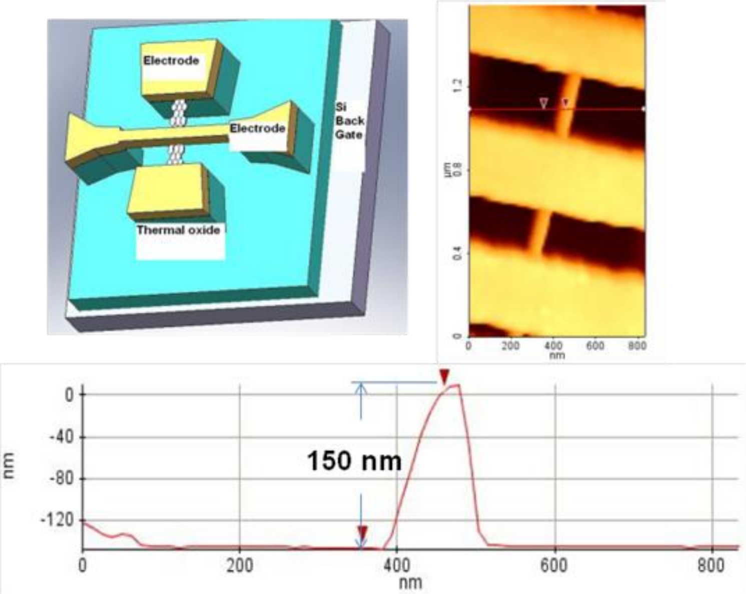

Figure A.9 (left) Schematic illustration of a GNR-FET consisting of a suspended GNR and the contact electrodes. (right) AFM image shows a GNR suspended by Au electrodes. (down) Line-profile of the AFM image in (right) reveals that the GNR is suspended ~150 nm above the substrate.

Etching process for suspension of GNRs devices by using hydrofluoride acid (HF) in the whole fabrication is the harshest one due to GNRs in aqueous solution. It also depends on the pattern design with respect to the channel length and width. For instance, it was found that the longer GNRs above 600 nm would not easily survive after etching process due to the surface tension when dried and suspended for GNRs. In order to overcome the surface tension between liquid and vapor phases, critical point dryer (CPD) has been considered to be used for preventing the devices from sagging. The model SAMDRI PVT 3D critical point dryer from tousimis was used in this work. The principle of using CPD is to preserve the structure from damaging when doing sample preparation in the environment of liquid-vapor coexistence, especially widely used in biological samples. Most of liquids such as methanol or ethanol have their well defined critical points, which can be used to replace water with specific pressure and temperature at

constant volume. At the critical point, the density of liquid and gas phase is equal; without liquid-gas boundary. Therefore, the dried sample can be preserved without structural damage due to surface tension after liquid-gas transition. Actually, the GNR sample was immersed in ethanol and substituted with LCO_2 under the pressure. The LCO_2 would be converted to gas phase at the critical point in high pressure chamber and removed at the temperature above 31^0C. However, there were always oily spots found after critical point drying no matter LCO_2 or filter had been changed, which seriously affected the following electric measurement. Figure A.10 shows the pictures before and after critical point drying, indicating the oily material attached around the electrodes on the right.

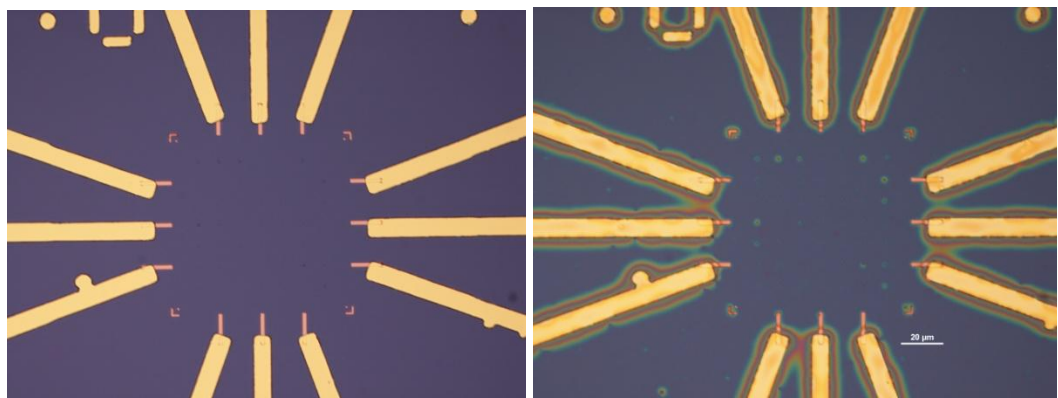

Figure A.10 The pictures show the situation before and after critical point drying. (Left) has clean surface before critical point drying. (Right) has oily material around the electrodes and spots in the center area.

Although the oily spots could possibly get improved by changing O ring of the chamber, it would not be helpful in our case if the surface tension was not the main cause to break down the GNRs. Recent results showed the GNRs bending down to the substrate after suspension using direct etching without critical point drying, which was not actually broken. That would leave this issue open, leading to the proper equipment to be considered in this process. Based on

the survival rate after suspension using direct etching, the humidity was taken into account for conducting this process in the beginning. In other words, the higher humidity (above 60%) the surrounding is, the larger survival rate (> 80%) the GNR has after suspension. However, this is just statistical data without theoretical verification if it favors high humidity during the liquid-vapor phase transition to reduce the surface tension when drying. Nevertheless, this process has been testing almost 100% survival rate after direct etching simply increases the temperature to boil the liquid IPA and blows it dry, according to the recent results. This is possibly caused by the less surface tension in hot IPA than that of in cold or warm IPA when experiencing liquid-vapor transition.

After successful suspension, the devices are annealed in vacuum at 600^0C for 10 minutes to clean the suspended ribbons and improve the electrical contacts before transferred to a Lakeshore Cryogenics vacuum probe station for further removing adsorbed impurities by current annealing and subsequent transport measurements in high vacuum. The residual impurities on GNRs are gradually removed by repeatedly passing a large current through the ribbon; the final amount of impurities of the GNRs depends both on initial amount and the degree of current annealing. In fact, thermal annealing is one of the tortuous processes after suspension of GNR devices. The annealing tool (Ulvac Mila 5000) with program setting used in this study is shown in Figure A.11.

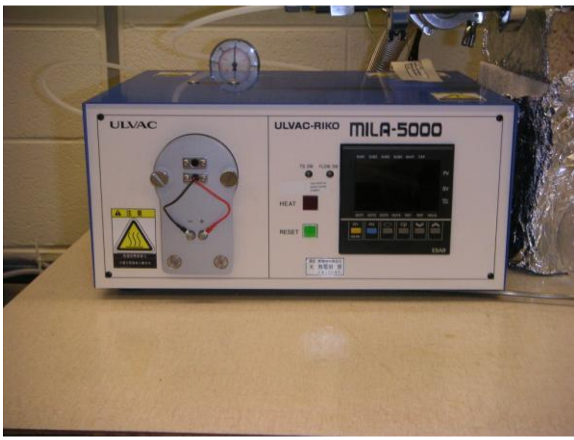

Figure A.11 The annealing tool (Ulvac Mila-5000) with program setting was used to remove the impurities and improve the contact resistance after GNRs suspension.

Due to the thermal expansion and comprise between GNRs and electrodes, it is also easy to break the GNRs in this process. Actually, nearly 50% devices will be useless after thermal annealing. However, it is necessary to do this process for improving the contact between GNRs and electrodes. The following Table A.2 shows the statistics of survived rate after etching and annealing for our GNRs devices.

Device Name	**Processes before Metal Evaporation**	**Metal (Cr/Au) Evaporation**	**Pre-annealing before suspension**	**Etching/ Suspension**	**Post-Annealing after suspension**	**Results**
9-9-10 no.10 - 8.1mg PmPv son45m cent60m s30m	Same as before	Cr0.3nm(rate 0.2A/S) Au35nm(rate 1.0A/S)	No	Etching by using old hot plate	600C Annealing (rate 3m)	Electric-50% good, put into chamber for further measurement
9-9-10 no.11 - 8.1mg PmPv	Same as before-	Cr0.3nm(rate 0.2A/S)	No	Etching by using	600C Annealing	50% good in chamber

son45m cent60m s30m	new pattern	Au35nm(rate 1.0A/S)		old hot plate	(rate 3m)	R3C1 showed strong temp. dependence at 77K
10-26-10 no.28 - 8.1mg PmPv son45m cent60m s30m	Same as before	Cr0.3nm(rate 0.2A/S) Au35nm(rate 1.0A/S)	No	Etching by using old hot plate	600C Annealing (rate 3m)	5/7 after annealing, Electrical Good, R5C0 good
10-26-10 no.30 - 8.1mg PmPV son45m cent60m s30m	Same as before	Cr0.3nm(rate 0.2A/S) Au35nm(rate 1.0A/S)	N/A	Etching by using old hot plate	600C Annealing (rate 3m)	3/5 survived after suspension
10-26-10 no.19 - 8.1mg PmPV son45m cent60m s30m	Same as before	Cr0.3nm(rate 0.2A/S) Au35nm(rate 1.0A/S)	N/A	Etching by using old hot plate	600C Annealing (rate 3m)	3/4 survived after suspension
10-26-10 no.23 - 8.1mg PmPV son45m cent60m s30m	Same as before	Cr0.3nm(rate 0.2A/S) Au35nm(rate 1.0A/S)	No	Etching by using old hot plate	600C Annealing (rate 3m)	3/6 survived after annealing
10-26-10 no.21 - 8.1mg PmPv son45m cent60m s30m	Same as before	Cr0.3nm(rate 0.2A/S) Au35nm(rate 1.0A/S)	No	Etching by using old hot plate	600C Annealing (rate 3m)	4/6 survived after suspension, all failed after annealing
2-11-11 no.1 - 8.1mg PmPv son45m cent60m s30m	Same as before	Cr0.3nm(rate 0.2A/S) Au35nm(rate 1.0A/S)	No	Etching by using old hot plate	600C Annealing (rate 3m)	5/7 survived after suspension
9-9-10 no.13 -	Same as	Cr0.3nm(rate	No	Etching	600C	6/6

8.1mg PmPv son45m cent60m s60m	before	0.2A/S) Au35nm(rate 1.0A/S)		by using old hot plate	Annealing (rate 3m)	suspension, 4/6 annealing
4-20-11 no.6 - 8.1mg PmPv son45m cent60m s30m	3 bottles plus filter twice	Cr0.3nm(rate 0.2A/S) Au35nm(rate 1.0A/S)	No	Etching by using old hot plate	600C Annealing (rate 3m)	8/11 after suspension, 6/11 after annealing
4-20-11 no.8 - 8.1mg PmPv son45m cent60m s30m	3 bottles plus filter twice	Cr0.3nm(rate 0.2A/S) Au35nm(rate 1.0A/S)	No	Etching by using old hot plate	600C Annealing (rate 3m)	8/11 after suspension, 6/11 after annealing

Table A.2 It shows the survived rate around 50% after harsh processes such as etching and annealing in our GNRs devices.

APPENDIX B

Several characterization tools have been used in this study such as atomic force microscope (AFM) and scanning electron microscope (SEM) to characterize the length, width and thickness of GNRs and MoS_2. A semiconductor parameter analyzer (Keithley 4200) was used to measure the characteristics of GNR and MoS_2 FET devices for $4.3 < T < 300$ K. Other tools like transmission electron microscope (TEM), scanning tunneling microscope (STM) were used to characterize the edge structure of GNRs and lattice constants of 2D materials. In addition, Raman spectrometer was used to characterize the properties of these materials as well regarding characteristic molecular vibration modes.

B.1 AFM characterization

Atomic force microscope is a powerful tool being extensively used in nano-scale size materials nowadays due to its resolution down to sub Å scale and precise measurement. Like other characterization tools are having their expansion and limitation, commercial AFM has been specifically developed to be applicable to many research fields using atomic force between tip and substrate. The non-contact mode AFM (Park System XE-70) as shown in Figure B.1 was used to locate individual GNRs and MoS_2 in this study with respect to the prefabricated Au alignment marks and to characterize their thickness, width and length as demonstrated in the previous section. The GNRs characterized by AFM mostly consist of 1-3 layers and 1~5 layers for MoS_2 flakes.

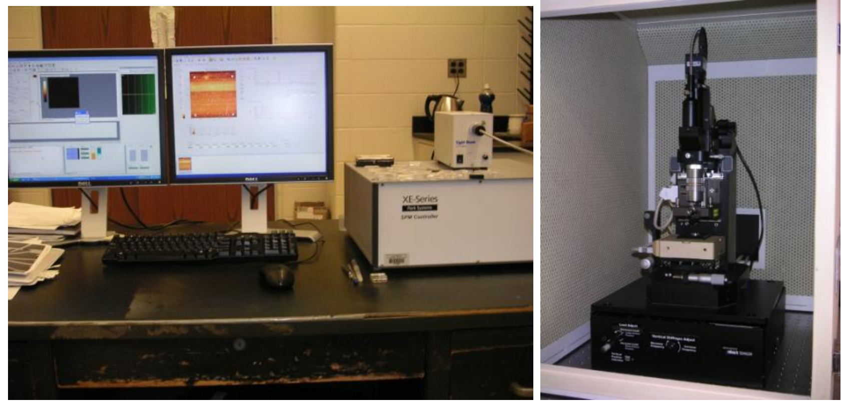

Figure B.1 The configuration of AFM (park XE-70) is used in this study, consisting of the software (left) and the optical mocrscope and X-Y scanner as the main body (right).

The benefit from park system (X-70) is the separation X-Y scanner and Z movement, which the position sensitive photo detector (PSPD) will not fluctuate too much as the tip moving up and down. The PSPD stays more stable than others when scanning the samples. Of course, the scanning images depend on the quality of the AFM tip as well. Some images occur during the scanning such as smearing, double image or extra lines, indicating the actions need to be taken, which either check the vibration of stage or replace the tip. Normally, the tip can be auto approaching to the sample surface once focus on the surface is done. Before approaching, the resonant frequency of tip has to be checked to assure the proper settings of drive and set point. The parameters of scan rate and Z servo gain were set at 0.5 Hz and 8, respectively. In order to obtain the good image, some skills of operation and patience are needed due to the slow through put for AFM scanning.

B.2 SEM/TEM characterization

Scanning electron microscope (SEM) and transmission electron microscope (TEM) are the most important two characterization tools in the study of nano scale materials. By using the

electron gun, the electrons are generated and accelerated in the SEM system through the column with high voltge~30 KV and coils inside, providing the interaction between electrons and sample surface with secondary electrons to investigate the morphology of the sample. Other signals from backscattered electrons and inelastic scattering like X-ray radiation from inner orbits are widely used for characterizing the grain size and chemical elements. Similar to SEM, TEM also uses the high energy electrons to hit the sample, but higher accelerating voltage ~200 KV to let the electrons penetrate the sample. The wavelength of electrons in TEM system can be reached to sub Ǻ by increasing the accelerating voltage to overcome the diffraction limit of visible light source, providing the ability to probe the nano structures or defects of the materials. In addition, the bright field image (BF) from non-scattered electron beam and dark field image from scattered non-central electron beam provide the detail information of lattice structure in nano scale materials. Figure B.2 shows the SEM (JOEL 7600F) and TEM (JOEL 2010) used in this work.

Figure B.2 The SEM (JOEL 7600F)-left and TEM (JOEL 2010)-right were used for characterizing the nano structure and chemical elements of materials.

From the experimental results shown in the previous chapter, the intrinsic bandgaps are possibly corresponding to the edge structures of GNRs. To verify the agreement between

theoretic modeling and experimental results, the measured devices were put into SEM for imaging from 25K~100K in magnification as shown in Figure B.3. The dimension of GNR of SEM images was observed around 28 nm in width. However, it did not give enough information about the situation of GNR edges.

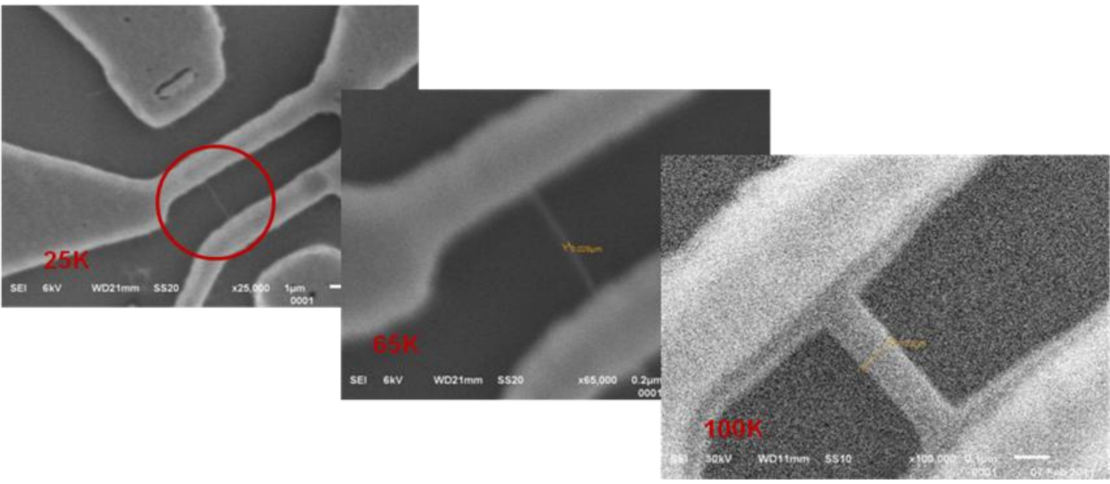

Figure B.3 The SEM images (25K~100K) show the dimension of measured device around 28 nm in width.

However, the resolution will depend on the SEM tool used for imaging. The following images as shown in Figure B.4 were taken from ZEISS-MERLIN with the magnification up to 1000K for GNRs. It is shown more clear images and easier to determine the width of GNRs around 20 nm, which is what we expected to have. Unfortunately, it is still not possible to gain the information of edge structure just by using SEM imaging.

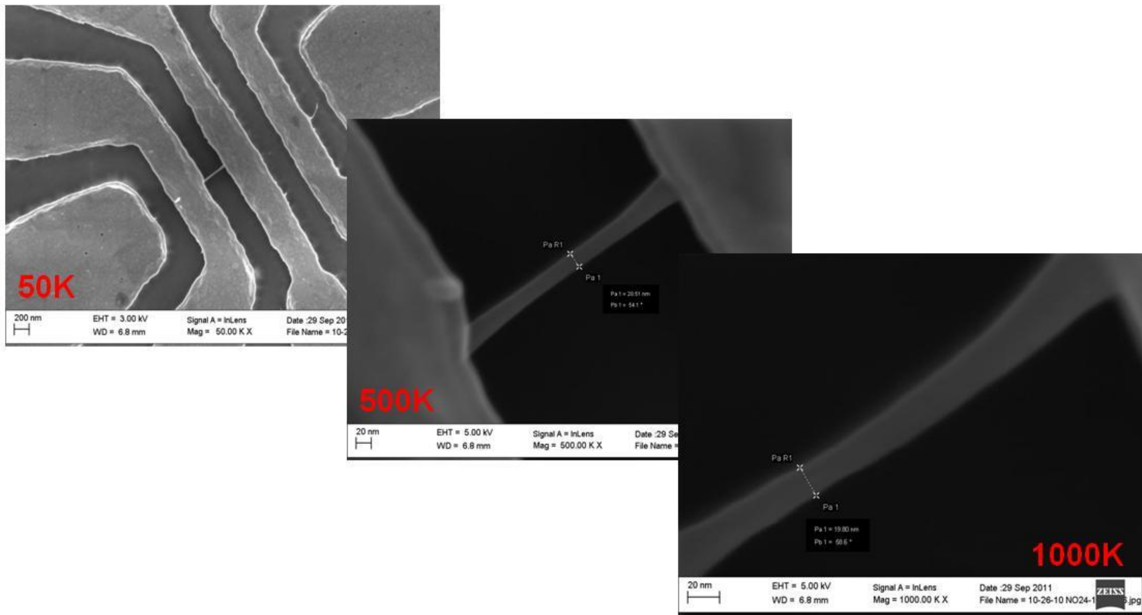

Figure B.4 The GNRs images were taken from ZEISS-MERLIN with magnification up to 1000K, indicating the width of GNRs ~20 nm.

Therefore, the real image of the edge structure has to be carried out by other effective tools than just by the topography of SEM. The candidates of observation tools would be selected as TEM or STM to have atomic resolution due to the possible GNR orientations created during synthesis. However, sample preparation for TEM observation is critical and important, suggesting that the traditional methods of triad pod or focus ion beam (FIB) for TEM samples may not be applicable to GNRs devices. The suspended GNRs may turn out to be too fragile to survive the transfer process for TEM images. In this unlikely scenario, we will fabricate FETs on a section of a several micro-long GNR and suspend only the active device area, while leaving the rest of the GNR supported by the substrate. This design will allow us to correlate the edge structure of the substrate-supported portion of the GNR with the electrical properties of the suspended GNR-FET. The second alternative is to focus on GNR-FETs with shorter suspended regions, which appeared to be more robust in the preliminary study. The third alternative is to

fabricate a metal grid on top of the GNR-FET devices using a shadow mask, cleave the substrate close to the metal grid, and etch away the substrate beneath the metal grid to suspend the GNR-FET devices from the Si substrate [131].

In order to have GNRs transferred to Cu grid or TEM holder for TEM observation, three approaches have been conducted in this work by using HF etching [129] plus thermal release tape, NaOH etching [130] plus HF etching and TMAH etching [131] plus HF etching to verify the best way of having good TEM samples. In the mean time, three steps have been considered to transfer the GNR to Cu grid, including i) the possibility of large electrodes transfer, ii) the possibility of real electrodes transfer and iii) the final stage of the possibility for GNRs transfer. The method of using TMAH and HF etching seems promising to have good TEM samples of GNR fitting in TEM holder for further observation.

(I) HF Etching +Thermal Release Tape

The large electrodes have been fabricated in the first trial to see the possibility of pattern transfer to Cu grid. Figure B.5 shows the large electrodes and Cu grid attached on it by dropping some PMMA around the corner.

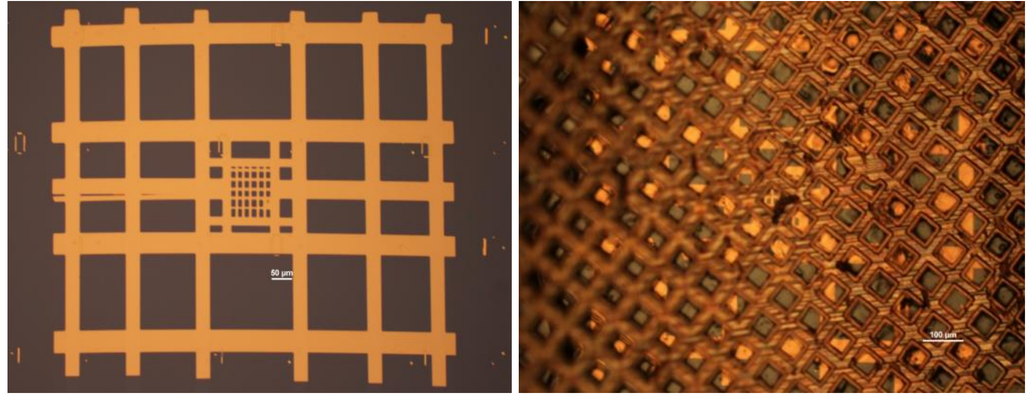

Figure B.5 The large electrodes were fabricated by standard E-beam lithography on the left and Cu grid was attached on the top by dropping some PMMA on the corner shown on the right.

Then drop HF on the large electrodes to etch away Si/SiO_2 for 1.5 hours as shown in the Figure B.6 on the left, which most of the electrodes had been peeled off. In order to transfer the pattern to Cu grid, the thermal release tape was applied to another pattern shown in the middle of Figure B.6 at the temperature 90^0C. However, the pattern did not transfer to Cu grid completely on the right in Figure B.6.

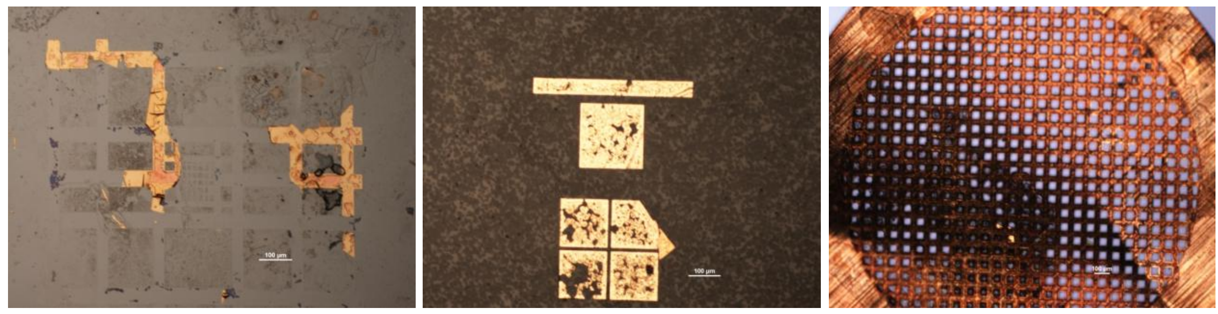

Figure B.6 Most of the large electrodes were peeled off on the left, and the pattern in the middle did not transfer to Cu grid completely shown on the right.

(II) NaOH + HF Etching

Another approach was to coat a layer of PMMA on the electrodes and put it into NaOH solution at the temperature 90^0C followed by HF etching. The purpose of using this method was to etch away Si/SiO_2 quickly and had the electrodes adhered on PMMA, which could form a sturdy layer and be transferred to Cu grid easily. Figure B.7 shows the results for 20 minutes etching, which gives non-flat and non-complete pattern on PMMA. Therefore, this approach seems not promising.

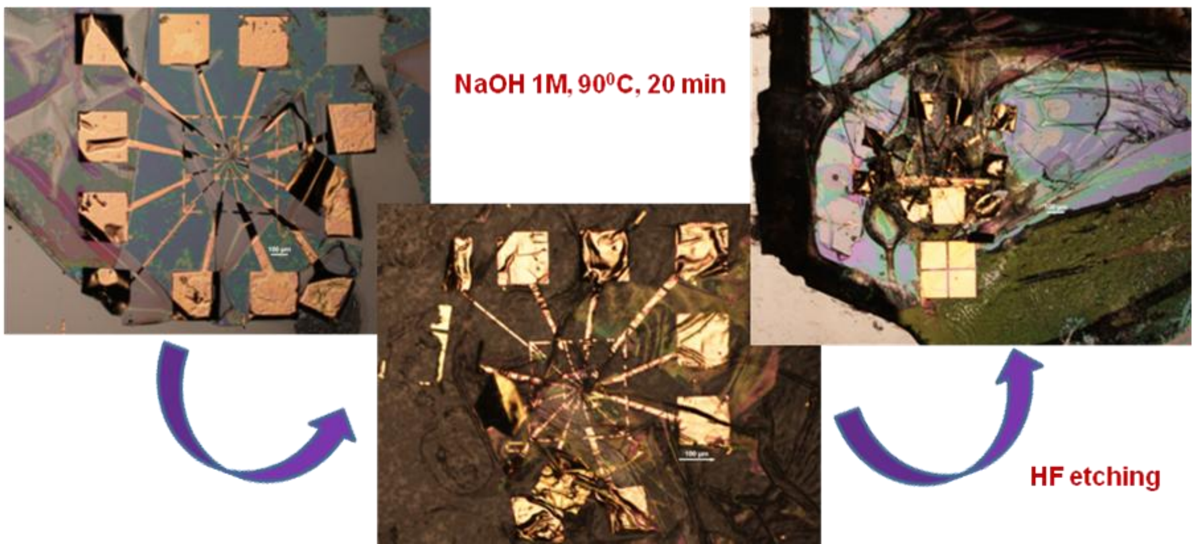

Figure B.7 The pattern does not completely adhere on PMMA and this approach seems not promising.

(III) TMAH + HF Etching

The purpose of using TMAH was to utilize the advantage of different etching rates for Si and SiO_2. First cut the edge close to the target, then put it into TMAH solution at the temperature 70^0C for 1 hour shown in Figure B.8. The Si substrate had almost been etched to the target line followed by HF etching to get rid of SiO_2. There were still electrodes suspended and survived, which could put into TEM holder directly for observation if there were GNRs in the electrodes. This approach seems to be very promising, giving the possibility for further TEM observation.

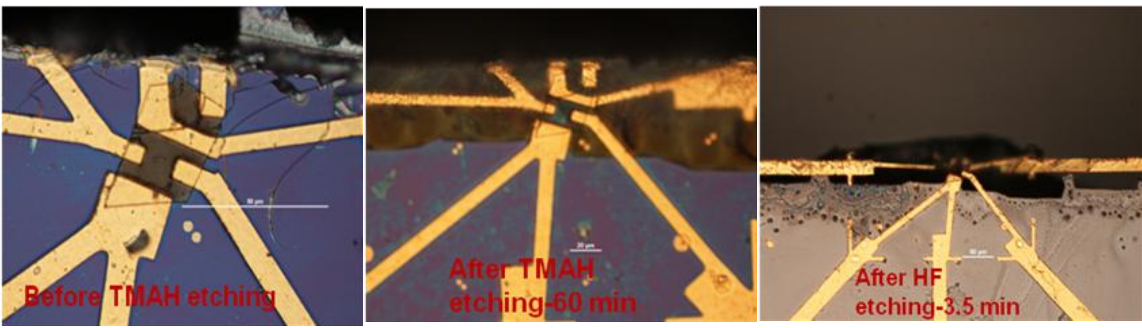

Figure B.8 There were some electrodes suspended and survived using TMAH and HF etching, giving the possibility for TEM observation.

Except the TEM preparation for GNRs, another TEM sample preparation for TiS_2 has been carried out using traditional method. In order to verify the composition and structure of TiS_2 material, a piece of flake was first mounted on the SEM holder to conduct energy dispersive spectrum (EDS) using JOEL 7600F SEM as shown in Figure B.9, illustrating the Ti and S peak with the atomic ratio 1:2, which was actually the composition of TiS_2 material.

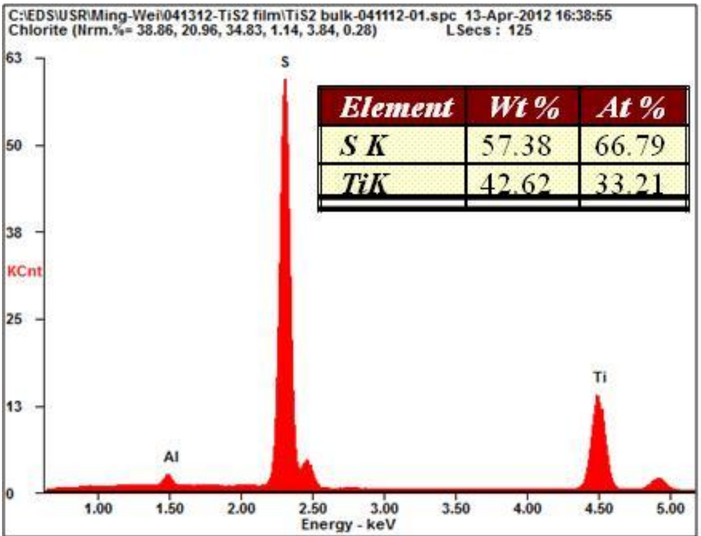

Figure B.9 The EDS spectrum shows the composition of TiS_2 film.

Next, another piece flake of TiS_2 was mounted on the TEM Cu grid without carbon film with proper ratio of epoxy to have ion milled to less than 100 nm thick for TEM observation.

Figure B.10 (a) shows the HR-TEM image, indicating the single crystal structure of TiS_2. In order to identify the exact structure of TiS_2, the selected area diffraction (SAD) as shown in the Figure B.10 (b) has been carried out for calculating the lattice constants of TiS_2.

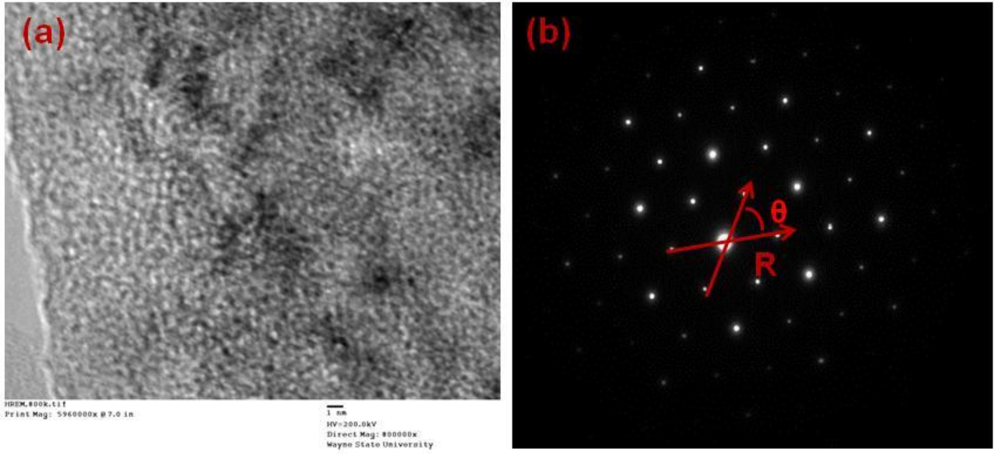

Figure B.10 The HRTEM image (a) and diffraction pattern using SAD (b) for 2-D material TiS_2, showing the lattice constant 3.397 Å after calculation.

According to the formula (B.1) shown below, where *R* and *d* are the radius of ring and distance of lattice plane in diffraction pattern, and *L* and *λ* are the camera length of TEM and wavelength of electron, respectively.

$$Rd = L\lambda \tag{B.1}$$

The first step is to calculate the $L\lambda$ using the diffraction pattern of standard sample like steel as 117.57 or this value can be obtained for *L* with magnification and for *λ* with accelerating voltage. Then second step is to measure the radius *R*~40 pixels from the diffraction pattern above and calculate *d*=2.939 Å, which quite matches the value 2.9418 Å listed in the table from the diffraction data of X-ray for TiS_2, indicating the plane [1, 0, 0] obtained from diffraction pattern.

In that case, the lattice constants are a=b=3.397Å for TiS_2 hexagonal structure, which is consistent with the value shown in the literature.

B.3 Electrical property measurement

As the devices had been fabricated, they would be measured at ambient probe station first regarding *I-V* curve for resistance. If the devices turned out to be good as reasonable range of resistance 10^4~10^5 Ω for GNRs and 10^7~10^9Ω for MoS_2, then they would be put into chamber in vacuum surroundings for further measurements. The equipment for measuring electrical properties corresponding to resistance, gate dependence and *I-V* characteristic curve is shown in the Figure B.11, including the high vacuum chamber (10^{-6} torr) of probe station with four probes inside (Lakeshore Cryogenics) and Keithley 4200 semiconductor parameter analyzer.

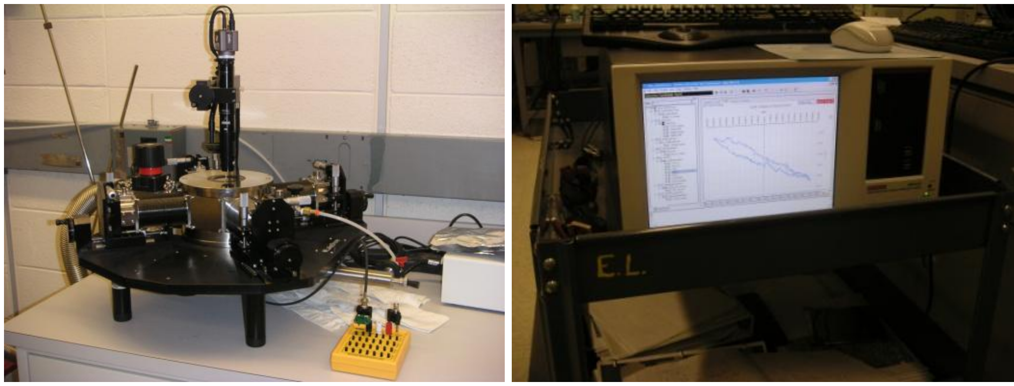

Figure B.11 The high vacuum probe station (Lakeshore Crygenics)-(left) and Keithley 4200 semiconductor parameter analyzer-(right) are used in this work.

Once the samples were determined to put into vacuum chamber, several things had to be carefully aware of. First, the probe tips are fragile and must be very cautiously handled during opening the chamber, trying not to touch the tips by extracting them from the center of the stage as far as possible. Next, the chamber stage has to be wiped out very clean to pump down to 10^{-6}

torr and get rid of any humidity or moisture as possible. In order to get good contact between substrate and stage, little vacuum grease for thermal contact and carbon tape for electrical contact will be applied to the samples. Check the connection of the probe tips before close the chamber and ready for pumping down by turbo pump.

As described in the previous chapter, the back-gate voltage would be applied to measure gate dependence as well as the top-gate configuration with placing polymer electrolyte or ionic liquid on the top of electrodes. The back-gate voltage was usually applied at the range *-15V~15V* for GNR devices to prevent them from collapsing, while the applied voltage could be increased to *-80V~80V* for the MoS_2 devices without suspension. The following Figure B.12 shows the typical gate dependence measurements for GNR and MoS_2, respectively.

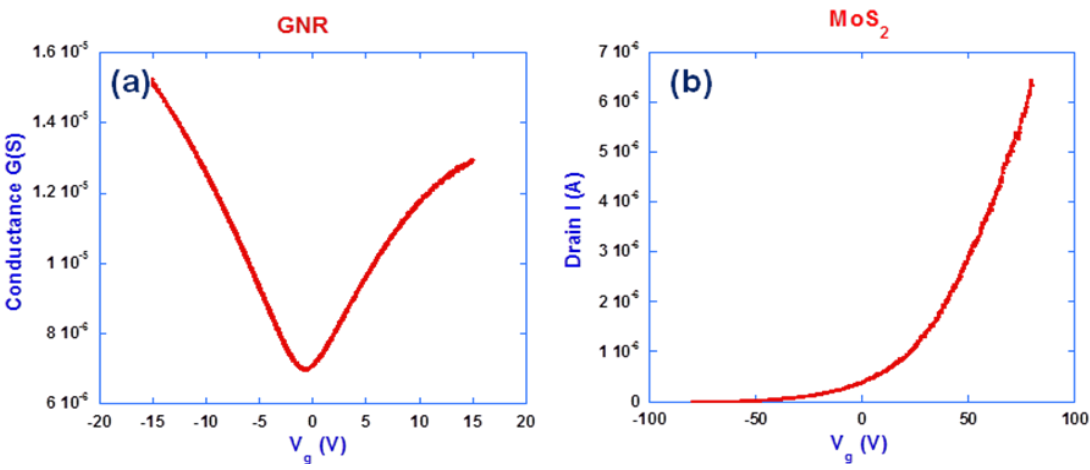

Figure B.12 (a)The gate dependence measurement V_g versus Conductance for GNR, and (b) the gate dependence measurement V_g versus drain current for MoS_2.

Actually, a series of measurements would be done if the device showed strong gate dependence result at ambient measurement. For example, the temperature dependence would be

carried out using liquid nitrogen or liquid helium, providing the data to calculate the mobility, contact resistance and other electrical characteristics as a function of temperature. The typical *I-V* curve would also be measured to see the ohmic contact with every single temperature point, especially for MoS_2 measurement due to contact issue between sample and deposited metals (normally Ti/Au). For GNR devices, the following two methods were conducted to measure the coulomb blockade or coulomb diamond generated by current annealing due to narrow channel similar to single electron transistor.

(I) DC measurement

In order to obtain the coulomb diamond with respect to the narrow constriction caused by current annealing, DC measurement for *I-V* curve with varying gate voltage must be set small enough to plot the graph. In other words, the coulomb diamond will not be able to see if the energy gap is not big enough, even cooling down to 4.2K using liquid helium. Sometimes, the system is not able to take so many data points, which contradicts our needs and we have to comprise between the data point and time consuming. Several attempts to measure the diamond had been done during this work. However, it is not every single trial acquiring the information for us to calculate the bandgap due to the static damage or fragility of GNR itself in these circumstances. A successful measurement of the coulomb diamond using DC measurement at 200K was shown in chapter 3, leading to the bandgap around 700 meV consistent with the value calculated from thermal energy gap. In addition, the software Origin was used to plot the coulomb diamond.

(II) AC measurement

AC measurement is a direct method of measuring *dI/dV* versus gate voltage (V_g) using lock-in amplifier setup shown in the Figure B.13 for plotting the coulomb diamond when cooling down to 4.2K. Before the leads connecting the sample, the lock-in has to set at 0 to avoid any damage of sample. Once connected, AC of lock-in amplifier will be set at 1V, which is 1 mV due to the divider. The sensitivity of current pre-amplifier was usually set at 10^{-7}/volt and 100~500 mV would be set for the sensitivity of lock-in amplifier referred to the measured drain current from DC measurement. The range of bias voltage and gate voltage also has to be referred to the DC measurement data as well. One thing is worth pointing out, which is the connection of back-gate voltage as ground to ground from the volt meter to probe station.

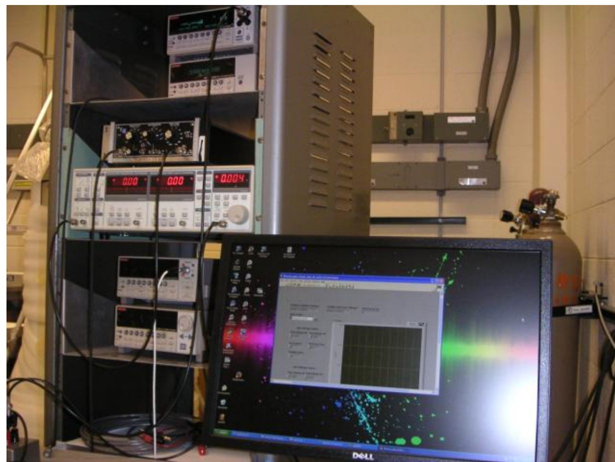

Figure B.13 The AC measurement setup includes lock-in amplifier, current pre-amplifier, volt and current meters together with Labview software to control the system.

As stated in the previous section, the survival rate was not high enough to do this measurement. Nevertheless, a successful measurement at 4.2K was shown the gap size around 100 meV in chapter 2, which was quite consistent with the value calculated from thermal activation energy of low disorder GNR.

B.4 Raman spectroscopy measurement

Raman scattering, an inelastic scattering, has been now widely used in characterization for materials with respect to the characteristic molecular vibration. In contrast to elastic scattering called Reyleigh scattering, Raman spectroscopy related to this inelastic scattering provides the fingerprint to identify the unknown materials. The Raman shift in $cm^{-1}$is the measure of the change in wavelength of scattered photons with respect to the incident photons based on the following equation (B.2), where h is the Planck constant, λ_s and λ_i are the wavelengths of scattered and incident photons, respectively.

$$\Delta E = h(\frac{1}{\lambda s} - \frac{1}{\lambda i}) \tag{B.2}$$

If the energy of scattered photons is less than that of incident photons, this process is known as Stokes scattering. While the energy of scattered photons is larger than that of incident photons, this process is called anti-Stokes scatteing. The Raman spectroscopy used in this study shown as Figure B.14 includes Jobin–Yvon Horiba Triax 550 spectrometer, a liquid-nitrogen cooled charge-coupled device (CCD) detector, an Olympus model BX41 microscope with a 100 × objective, and a Modu-Laser (Stellar-Pro-L) Argon-ion laser operating at 514.5 nm. The laser spot size was ~ 1 μm in diameter and the laser power at the sample was maintained at low level (~ 200 μW) to avoid any heating effect.

Figure B.14 The Raman spectroscopy was used in this study, including Jobin–Yvon Horiba Triax 550 spectrometer, a liquid-nitrogen cooled charge-coupled device (CCD) detector, an Olympus model BX41 microscope with a 100 × objective, and a Modu-Laser (Stellar-Pro-L) Argon-ion laser operating at 514.5 nm.

The parameters such as exposure time and frequency were normally set at 20 sec and 5 sc for most of our samples. The following Figure B.15 shows the typical Raman spectra for MoS_2 material and CVD grown graphene, indicating the characteristic peaks related to crystal structure for MoS_2 and D/G peak ratio with respect to impurity level for graphene, respectively.

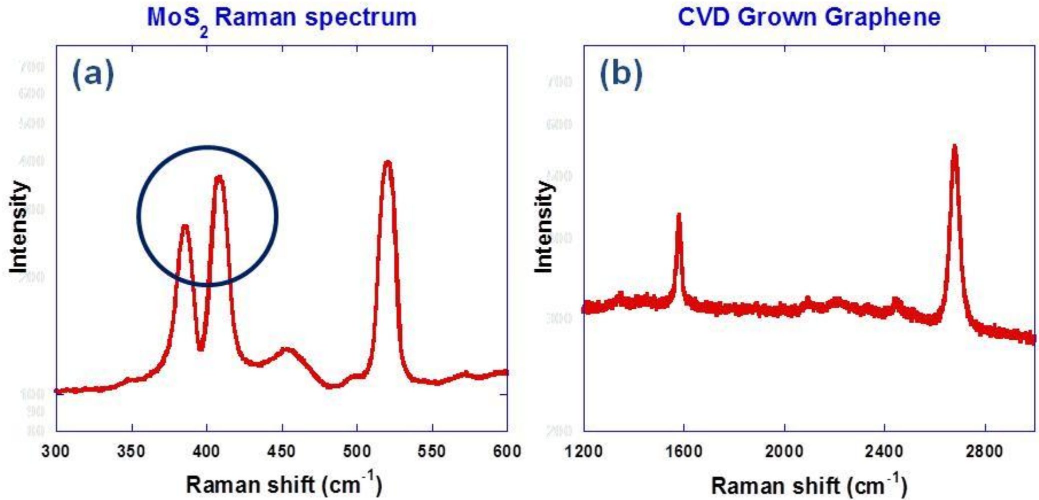

Figure B.15 The characteristic peaks of Raman spetra for (a) MoS_2 and (b) CVD grown graphene, indicating the crystal structure and impurity level for these two materials, respectively.

B.5 XRD measurement

X-ray diffraction (XRD) is commonly used nowaday to investigate the structure, phase transition and lattice constants of bulk or thin film materials. The wavelength of X-ray is comparable to the spacing of lattice, making it a suitable tool to probe the structures of crystals. The Rigaku RU 2000 X-ray powder diffractometer with wavelength 1.5418Å was used to characterize the structures of our 2D materials in this study. The monochromatic and collimated X-ray hits the sample at an angle θ to the plane of the sample and diffracts from the plane according to Bragg's law shown below.

$$2d \sin\theta = n\lambda \tag{B.3}$$

where d is the spacing of the crystal lattice, λ the wavelength of X-ray and n the order of diffraction. Once the X-ray spectrum came out, the characteristic peaks of measured materials could be identified when comparing the fingerprints in the data file. The following Figure B.16 shows the characteristic X-ray spectrum of TiS_2 to verify the phase of this material, indicating the peaks of pure TiS_2 combining with little oxidation of TiO_2. Therefore, XRD is a powerful tool to indentify the structure of crystal, even unknown materials.

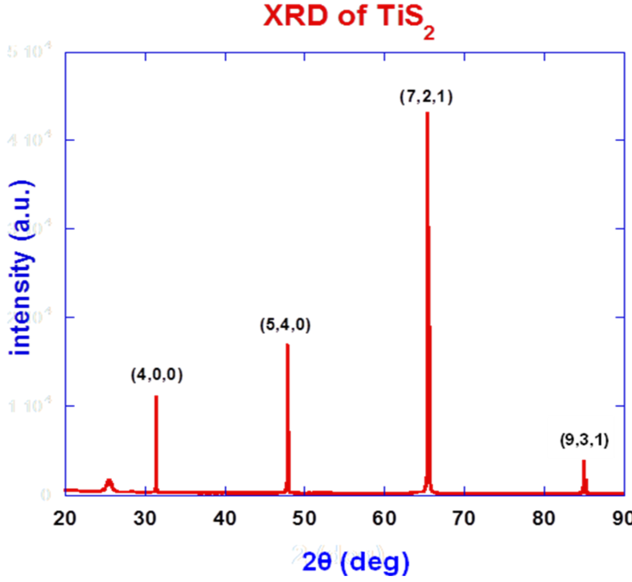

Figure B.16 The XRD spectrum of 2D material TiS_2 using diffractometer indicates the pure TiS_2 characterisitc peaks together with little oxidation of TiO_2 peak.

B.6 STM measurement

As mentioned in the beginning, scanning tunneling microscope (STM) or scanning tunneling spectroscopy (STS) is one of the characterization tools to probe the edge structure and crystallography of GNRs. By means of the unique measurement of STM/STS through tunneling current between tip and sample surface, the correlation between the electrical properties of GNR-FETs with the atomic structure and crystallographic orientation of GNR edges and the detail band structure (e.g. the intrinsic bandgap) can expectedly be established. Low temperature STM is capable of resolving the atomic structure at the GNR edges and measuring the local electronic structure of GNRs.

A unique quadraprobe STM system to perform combined STM/STS and electrical transport/transport spectroscopy measurements in ultrahigh vacuum was used in this work and in collaboration with Dr. An-Ping Li at Oak Ridge National Laboratory (ORNL). The quadraprobe STM system includes a high-resolution FESEM and four independently controllable STM probes [155]. Since STM imaging of GNR edges requires conductive substrates, it may prove extremely challenging to carry out STM/STS studies on suspended GNRs. On the other hand, fabrication of GNR-FETs requires insulating substrates. However, in order to correlate the electronic and edge structures (as determined by STS/STM) with the device characteristics of GNR-FETs (transport properties), it is necessary to carry out both STS/STM and transport measurements on the same GNRs. To resolve this apparent controversy, GNRs were deposited partially on conducting substrate for STS/STM and partially on insulting substrate for GNR-FET device fabrication and transport measurement. To achieve this goal, large area graphene sheets produced by CVD were deposited on SiO_2 substrate to form conducting patches before depositing GNRs from a GNR solution. The STM/STS measurement had been conducted at low temperatures, trying to obtain *dI/dV* differential conductance of GNRs. However, the bandgap could not be obviously obtained possibly due to the leakage current for unclean sample.

BIBLIOGRAPHY

[1] K. S. Novoselov, A. K. Geim, S. V. Morozov, D. Jiang, Y. Zhang, S. V. Dubonos, I. V. Grigorieva, and A. A. Firsov, 'Electric Field in Atomically Thin Carbon Films', *Science,* 306 (2004), 666-69

[2] A. K. Geim, and K. S. Novoselov, 'The Rise of Graphene', *Nature Materials,* 6 (2007), 183-91.

[3] A. K. Geim, 'Graphene: Status and Prospects', *Science,* 324 (2009), 1530-34.

[4] Matthew J. Allen, Vincent C. Tung, and Richard B. Kaner, 'Honeycomb Carbon: A Review of Graphene', *Chemical Reviews,* 110 (2009), 132-45.

[5] Jacopo Brivio, Duncan T. L. Alexander, and Andras Kis, 'Ripples and Layers in Ultrathin MoS_2 Membranes', *Nano Letters,* 11 (2011), 5148-53.

[6] K. S. Novoselov, A. K. Geim, S. V. Morozov, D. Jiang, M. I. Katsnelson, I. V. Grigorieva, S. V. Dubonos, and A. A. Firsov, 'Two-Dimensional Gas of Massless Dirac Fermions in Graphene', *Nature,* 438 (2005), 197-200.

[7] Ming-Wei Lin, Cheng Ling, Luis A. Agapito, Nicholas Kioussis, Yiyang Zhang, Mark Ming-Cheng Cheng, Wei L. Wang, Efthimios Kaxiras, and Zhixian Zhou, 'Approaching the Intrinsic Band Gap in Suspended High-Mobility Graphene Nanoribbons', *Physical Review B,* 84 (2011), 125411.

[8] Ming-Wei Lin, Cheng Ling, Yiyang Zhang, Hyeun Joong Yoon, Mark Ming-Cheng Cheng, Luis A Agapito, Nicholas Kioussis, Noppi Widjaja, and Zhixian Zhou, 'Room-Temperature High on/off Ratio in Suspended Graphene Nanoribbon Field-Effect Transistors', *Nanotechnology,* 22 (2011), 265201.

[9] Cheng Ling, Gabriel Setzler, Ming-Wei Lin, Kulwinder Singh Dhindsa, Jin Jin, Hyeun Joong Yoon, Seung Soo Kim, Mark Ming-Cheng Cheng, Noppi Widjaja, and Zhixian Zhou, 'Electrical Transport Properties of Graphene Nanoribbons Produced from Sonicating Graphite in Solution', *Nanotechnology,* 22 (2011), 325201.

[10] Ming-Wei Lin, Lezhang Liu, Qing Lan, Xuebin Tan, Kulwinder S Dhindsa, Peng Zeng, Vaman M Naik, Mark Ming-Cheng Cheng, and Zhixian Zhou, 'Mobility Enhancement and Highly Efficient Gating of Monolayer MoS_2 Transistors with Polymer Electrolyte', *Journal of Physics D: Applied Physics,* 45 (2012), 345102.

[11] Y. Zhang, T. T. Tang, C. Girit, Z. Hao, M. C. Martin, A. Zettl, M. F. Crommie, Y. R. Shen, and F. Wang, 'Direct Observation of a Widely Tunable Bandgap in Bilayer Graphene', *Nature,* 459 (2009), 820-23.

[12] F. Guinea, M. I. Katsnelson, and A. K. Geim, 'Energy Gaps and a Zero-Field Quantum Hall Effect in Graphene by Strain Engineering', *Nature Physics,* 6 (2010), 30-33.

[13] S. H. Cheng, K. Zou, F. Okino, H. R. Gutierrez, A. Gupta, N. Shen, P. C. Eklund, J. O. Sofo, and J. Zhu, 'Reversible Fluorination of Graphene: Evidence of a Two-Dimensional Wide Bandgap Semiconductor', *Physical Review B,* 81 (2010), 205435.

[14] Luis A. Agapito, and Nicholas Kioussis, '“Seamless” Graphene Interconnects for the Prospect of All-Carbon Spin-Polarized Field-Effect Transistors', *The Journal of Physical Chemistry C,* 115 (2011), 2874-79.

[15] Young-Woo Son, Marvin L. Cohen, and Steven G. Louie, 'Energy Gaps in Graphene Nanoribbons', *Physical Review Letters,* 97 (2006), 216803.

[16] Melinda Y. Han, Barbaros Özyilmaz, Yuanbo Zhang, and Philip Kim, 'Energy Band-Gap Engineering of Graphene Nanoribbons', *Physical Review Letters,* 98 (2007), 206805.

[17] Z. Chen, Y. M. Lin, M. J. Rooks, and P. Avouris, 'Graphene Nano-Ribbon Electronics', *Physica E: Low-Dimensional Systems and Nanostructures,* 40 (2007), 228-32.

[18] S. Adam, S. Cho, M. S. Fuhrer, and S. Das Sarma, 'Density Inhomogeneity Driven Percolation Metal-Insulator Transition and Dimensional Crossover in Graphene Nanoribbons', *Physical Review Letters,* 101 (2008), 046404.

[19] M. Evaldsson, I. V. Zozoulenko, Hengyi Xu, and T. Heinzel, 'Edge-Disorder-Induced Anderson Localization and Conduction Gap in Graphene Nanoribbons', *Physical Review B,* 78 (2008), 161407.

[20] F. Sols, F. Guinea, and A. H. Castro Neto, 'Coulomb Blockade in Graphene Nanoribbons', *Physical Review Letters,* 99 (2007), 166803.

[21] Melinda Y. Han, Juliana C. Brant, and Philip Kim, 'Electron Transport in Disordered Graphene Nanoribbons', *Physical Review Letters,* 104 (2010), 056801.

[22] Patrick Gallagher, Kathryn Todd, and David Goldhaber-Gordon, 'Disorder-Induced Gap Behavior in Graphene Nanoribbons', *Physical Review B,* 81 (2010), 115409.

[23] L. Jiao, X. Wang, G. Diankov, H. Wang, and H. Dai, 'Facile Synthesis of High-Quality Graphene Nanoribbons', *Nature Nanotechnology,* 5 (2010), 321-25.

[24] T. Shimizu, J. Haruyama, D. C. Marcano, D. V. Kosinkin, J. M. Tour, K. Hirose, and K. Suenaga, 'Large Intrinsic Energy Bandgaps in Annealed Nanotube-Derived Graphene Nanoribbons', *Nature Nanotechnology,* 6 (2011), 45-50.

[25] J. B. Oostinga, H. B. Heersche, X. Liu, A. F. Morpurgo, and L. M. K. Vandersypen, 'Gate-Induced Insulating State in Bilayer Graphene Devices', *Nature Materials,* 7 (2008), 151-57.

[26] K. I. Bolotin, K. J. Sikes, Z. Jiang, M. Klima, G. Fudenberg, J. Hone, P. Kim, and H. L. Stormer, 'Ultrahigh Electron Mobility in Suspended Graphene', *Solid State Communications,* 146 (2008), 351-55.

[27] X. Du, I. Skachko, A. Barker, and E. Y. Andrei, 'Approaching Ballistic Transport in Suspended Graphene', *Nature Nanotechnology,* 3 (2008), 491-95.

[28] Miriam Moreno-Moreno, Andrés Castellanos-Gomez, Gabino Rubio-Bollinger, Julio Gomez-Herrero, and Nicolás Agraït, 'Ultralong Natural Graphene Nanoribbons and Their Electrical Conductivity', *Small,* 5 (2009), 924-27.

[29] Lei Liao, Jingwei Bai, Yongquan Qu, Yung-chen Lin, Yujing Li, Yu Huang, and Xiangfeng Duan, 'High-K Oxide Nanoribbons as Gate Dielectrics for High Mobility Top-Gated Graphene Transistors', *Proceedings of the National Academy of Sciences,* 107 (2010), 6711-15.

[30] C. Lian, K. Tahy, T. Fang, G. Li, H. G. Xing, and D. Jena, 'Quantum Transport in Graphene Nanoribbons Patterned by Metal Masks', *Applied Physics Letters,* 96 (2010).

[31] K. I. Bolotin, K. J. Sikes, J. Hone, H. L. Stormer, and P. Kim, 'Temperature-Dependent Transport in Suspended Graphene', *Physical Review Letters,* 101 (2008), 096802.

[32] S. Kim, J. Nah, I. Jo, D. Shahrjerdi, L. Colombo, Z. Yao, E. Tutuc, and S. K. Banerjee, 'Realization of a High Mobility Dual-Gated Graphene Field-Effect Transistor with Al_2O_3 Dielectric', *Applied Physics Letters,* 94 (2009).

[33] E. J. H. Lee, K. Balasubramanian, R. T. Weitz, M. Burghard, and K. Kern, 'Contact and Edge Effects in Graphene Devices', *Nature Nanotechnology,* 3 (2008), 486-90.

[34] S. Russo, M. F. Craciun, M. Yamamoto, A. F. Morpurgo, and S. Tarucha, 'Contact Resistance in Graphene-Based Devices', *Physica E: Low-dimensional Systems and Nanostructures,* 42 (2010), 677-79.

[35] Tian Fang, Aniruddha Konar, Huili Xing, and Debdeep Jena, 'Mobility in Semiconducting Graphene Nanoribbons: Phonon, Impurity, and Edge Roughness Scattering', *Physical Review B,* 78 (2008), 205403.

[36] Priscilla Kailian Ang, Shuai Wang, Qiaoliang Bao, John T. L. Thong, and Kian Ping Loh, 'High-Throughput Synthesis of Graphene by Intercalation−Exfoliation of Graphite Oxide and Study of Ionic Screening in Graphene Transistor', *ACS Nano,* 3 (2009), 3587-94.

[37] Oded Hod, Verónica Barone, Juan E. Peralta, and Gustavo E. Scuseria, 'Enhanced Half-Metallicity in Edge-Oxidized Zigzag Graphene Nanoribbons', *Nano Letters,* 7 (2007), 2295-99.

[38] C. Tao, L. Jiao, O. V. Yazyev, Y. C. Chen, J. Feng, X. Zhang, R. B. Capaz, J. M. Tour, A. Zettl, S. G. Louie, H. Dai, and M. F. Crommie, 'Spatially Resolving Edge States of Chiral Graphene Nanoribbons', *Nature Physics,* 7 (2011), 616-20.

[39] J. H. Chen, C. Jang, S. Adam, M. S. Fuhrer, E. D. Williams, and M. Ishigami, 'Charged-Impurity Scattering in Graphene', *Nature Physics,* 4 (2008), 377-81.

[40] L. Pisani, J. A. Chan, B. Montanari, and N. M. Harrison, 'Electronic Structure and Magnetic Properties of Graphitic Ribbons', *Physical Review B,* 75 (2007), 064418.

[41] Luis A. Agapito, and Nicholas Kioussis, '"Seamless" Graphene Interconnects for the Prospect of All-Carbon Spin-Polarized Field-Effect Transistors', *The Journal of Physical Chemistry C,* 115 (2011), 2874-79.

[42] Y. Hancock, A. Uppstu, K. Saloriutta, A. Harju, and M. J. Puska, 'Generalized Tight-Binding Transport Model for Graphene Nanoribbon-Based Systems', *Physical Review B,* 81 (2010), 245402.

[43] J. Fernández-Rossier, and J. J. Palacios, 'Magnetism in Graphene Nanoislands', *Physical Review Letters,* 99 (2007), 177204.

[44] Wei L. Wang, Sheng Meng, and Efthimios Kaxiras, 'Graphene Nanoflakes with Large Spin', *Nano Letters,* 8 (2007), 241-45.

[45] M. Wimmer, A. R. Akhmerov, and F. Guinea, 'Robustness of Edge States in Graphene Quantum Dots', *Physical Review B,* 82 (2010), 045409.

[46] J. Jiang, W. Lu, and J. Bernholc, 'Edge States and Optical Transition Energies in Carbon Nanoribbons', *Physical Review Letters,* 101 (2008), 246803.

[47] Roland Gillen, and John Robertson, 'The Screened-Exchange Approximation as Alternative Method for Dft Calculations on Graphene Structures', *physica status solidi (b),* 247 (2010), 2945-48.

[48] Roland Gillen, and John Robertson, 'Density Functional Theory Screened-Exchange Approach for Investigating Electronical Properties of Graphene-Related Materials', *Physical Review B,* 82 (2010), 125406.

[49] Li Yang, Cheol-Hwan Park, Young-Woo Son, Marvin L. Cohen, and Steven G. Louie, 'Quasiparticle Energies and Band Gaps in Graphene Nanoribbons', *Physical Review Letters,* 99 (2007), 186801.

[50] J. Heyd, G. E. Scuseria, and M. Ernzerhof, 'Hybrid Functionals Based on a Screened Coulomb Potential', *Journal of Chemical Physics,* 118 (2003), 8207-15.

[51] Verónica Barone, Oded Hod, and Gustavo E. Scuseria, 'Electronic Structure and Stability of Semiconducting Graphene Nanoribbons', *Nano Letters,* 6 (2006), 2748-54.

[52] Adarsh Sagar, Eduardo J. H. Lee, Kannan Balasubramanian, Marko Burghard, and Klaus Kern, 'Effect of Stacking Order on the Electric-Field Induced Carrier Modulation in Graphene Bilayers', *Nano Letters,* 9 (2009), 3124-28.

[53] Yang Lu, and Jing Guo, 'Band Gap of Strained Graphene Nanoribbons', *Nano Research,* 3 (2010), 189-99.

[54] Claire Berger, Zhimin Song, Xuebin Li, Xiaosong Wu, Nate Brown, Cécile Naud, Didier Mayou, Tianbo Li, Joanna Hass, Alexei N. Marchenkov, Edward H. Conrad, Phillip N. First, and Walt A. de Heer, 'Electronic Confinement and Coherence in Patterned Epitaxial Graphene', *Science,* 312 (2006), 1191-96.

[55] Xiaolin Li, Xinran Wang, Li Zhang, Sangwon Lee, and Hongjie Dai, 'Chemically Derived, Ultrasmooth Graphene Nanoribbon Semiconductors', *Science,* 319 (2008), 1229-32.

[56] Zhong-Shuai Wu, Wencai Ren, Libo Gao, Bilu Liu, Jinping Zhao, and Hui-Ming Cheng, 'Efficient Synthesis of Graphene Nanoribbons Sonochemically Cut from Graphene Sheets', *Nano Research,* 3 (2010), 16-22.

[57] Sujit S. Datta, Douglas R. Strachan, Samuel M. Khamis, and A. T. Charlie Johnson, 'Crystallographic Etching of Few-Layer Graphene', *Nano Letters,* 8 (2008), 1912-15.

[58] Lijie Ci, Zhiping Xu, Lili Wang, Wei Gao, Feng Ding, Kevin Kelly, Boris Yakobson, and Pulickel Ajayan, 'Controlled Nanocutting of Graphene', *Nano Research,* 1 (2008), 116-22.

[59] L. Tapasztó, G. Dobrik, P. Lambin, and L. P. Biró, 'Tailoring the Atomic Structure of Graphene Nanoribbons by Scanning Tunnelling Microscope Lithography', *Nature Nanotechnology,* 3 (2008), 397-401.

[60] Jingwei Bai, Xiangfeng Duan, and Yu Huang, 'Rational Fabrication of Graphene Nanoribbons Using a Nanowire Etch Mask', *Nano Letters,* 9 (2009), 2083-87.

[61] D. V. Kosynkin, A. L. Higginbotham, A. Sinitskii, J. R. Lomeda, A. Dimiev, B. K. Price, and J. M. Tour, 'Longitudinal Unzipping of Carbon Nanotubes to Form Graphene Nanoribbons', *Nature,* 458 (2009), 872-76.

[62] L. Jiao, L. Zhang, X. Wang, G. Diankov, and H. Dai, 'Narrow Graphene Nanoribbons from Carbon Nanotubes', *Nature,* 458 (2009), 877-80.

[63] Xinran Wang, Yijian Ouyang, Xiaolin Li, Hailiang Wang, Jing Guo, and Hongjie Dai, 'Room-Temperature All-Semiconducting Sub-10-Nm Graphene Nanoribbon Field-Effect Transistors', *Physical Review Letters,* 100 (2008), 206803.

[64] Fengnian Xia, Damon B. Farmer, Yu-ming Lin, and Phaedon Avouris, 'Graphene Field-Effect Transistors with High on/Off Current Ratio and Large Transport Band Gap at Room Temperature', *Nano Letters,* 10 (2010), 715-18.

[65] L. A. Ponomarenko, F. Schedin, M. I. Katsnelson, R. Yang, E. W. Hill, K. S. Novoselov, and A. K. Geim, 'Chaotic Dirac Billiard in Graphene Quantum Dots', *Science,* 320 (2008), 356-58.

[66] R. Murali, Y. Yang, K. Brenner, T. Beck, and J. D. Meindl, 'Breakdown Current Density of Graphene Nanoribbons', *Applied Physics Letters,* 94 (2009).

[67] Yu-Ming Lin, Vasili Perebeinos, Zhihong Chen, and Phaedon Avouris, 'Electrical Observation of Subband Formation in Graphene Nanoribbons', *Physical Review B,* 78 (2008), 161409.

[68] Xiaoting Jia, Mario Hofmann, Vincent Meunier, Bobby G. Sumpter, Jessica Campos-Delgado, José Manuel Romo-Herrera, Hyungbin Son, Ya-Ping Hsieh, Alfonso Reina, Jing Kong, Mauricio Terrones, and Mildred S. Dresselhaus, 'Controlled Formation of Sharp Zigzag and Armchair Edges in Graphitic Nanoribbons', *Science,* 323 (2009), 1701-05.

[69] Chunxiao Cong, Ting Yu, and Haomin Wang, 'Raman Study on the G Mode of Graphene for Determination of Edge Orientation', *ACS Nano,* 4 (2010), 3175-80.

[70] Wencai Ren, Riichiro Saito, Libo Gao, Fawei Zheng, Zhongshuai Wu, Bilu Liu, Masaru Furukawa, Jinping Zhao, Zongping Chen, and Hui-Ming Cheng, 'Edge Phonon State of Mono- and Few-Layer Graphene Nanoribbons Observed by Surface and Interference Co-Enhanced Raman Spectroscopy', *Physical Review B,* 81 (2010), 035412.

[71] C. Casiraghi, A. Hartschuh, H. Qian, S. Piscanec, C. Georgi, A. Fasoli, K. S. Novoselov, D. M. Basko, and A. C. Ferrari, 'Raman Spectroscopy of Graphene Edges', *Nano Letters,* 9 (2009), 1433-41.

[72] M. Begliarbekov, O. Sul, S. Kalliakos, E. H. Yang, and S. Strauf, 'Determination of Edge Purity in Bilayer Graphene Using M-Raman Spectroscopy', *Applied Physics Letters,* 97 (2010).

[73] Çağlar Ö. Girit, Jannik C. Meyer, Rolf Erni, Marta D. Rossell, C. Kisielowski, Li Yang, Cheol-Hwan Park, M. F. Crommie, Marvin L. Cohen, Steven G. Louie, and A. Zettl, 'Graphene at the Edge: Stability and Dynamics', *Science,* 323 (2009), 1705-08.

[74] J. Moser, A. Verdaguer, D. Jiḿnez, A. Barreiro, and A. Bachtold, 'The Environment of Graphene Probed by Electrostatic Force Microscopy', *Applied Physics Letters,* 92 (2008).

[75] Yaping Dan, Ye Lu, Nicholas J. Kybert, Zhengtang Luo, and A. T. Charlie Johnson, 'Intrinsic Response of Graphene Vapor Sensors', *Nano Letters,* 9 (2009), 1472-75.

[76] Patrick Gallagher, Kathryn Todd, and David Goldhaber-Gordon, 'Disorder-Induced Gap Behavior in Graphene Nanoribbons', *Physical Review B,* 81 (2010), 115409.

[77] M. Evaldsson, I. V. Zozoulenko, Hengyi Xu, and T. Heinzel, 'Edge-Disorder-Induced Anderson Localization and Conduction Gap in Graphene Nanoribbons', *Physical Review B,* 78 (2008), 161407.

[78] Liming Xie, Liying Jiao, and Hongjie Dai, 'Selective Etching of Graphene Edges by Hydrogen Plasma', *Journal of the American Chemical Society,* 132 (2010), 14751-53.

[79] Ye Lu, Brett Goldsmith, Douglas R. Strachan, Jong Hsien Lim, Zhengtang Luo, and A. T. Charlie Johnson, 'High-on/Off-Ratio Graphene Nanoconstriction Field-Effect Transistor', *Small,* 6 (2010), 2748-54.

[80] D. Li, M. B. Müller, S. Gilje, R. B. Kaner, and G. G. Wallace, 'Processable Aqueous Dispersions of Graphene Nanosheets', *Nature Nanotechnology,* 3 (2008), 101-05.

[81] Y. Hernandez, V. Nicolosi, M. Lotya, F. M. Blighe, Z. Sun, S. De, I. T. McGovern, B. Holland, M. Byrne, Y. K. Gun'ko, J. J. Boland, P. Niraj, G. Duesberg, S. Krishnamurthy, R. Goodhue, J. Hutchison, V. Scardaci, A. C. Ferrari, and J. N. Coleman, 'High-Yield Production of Graphene by Liquid-Phase Exfoliation of Graphite', *Nature Nanotechnology,* 3 (2008), 563-68.

[82] S. Park, and R. S. Ruoff, 'Chemical Methods for the Production of Graphenes', *Nature nanotechnology,* 4 (2009), 217-24.

[83] Scott Gilje, Song Han, Minsheng Wang, Kang L. Wang, and Richard B. Kaner, 'A Chemical Route to Graphene for Device Applications', *Nano Letters,* 7 (2007), 3394-98.

[84] Alan B. Kaiser, Cristina Gómez-Navarro, Ravi S. Sundaram, Marko Burghard, and Klaus Kern, 'Electrical Conduction Mechanism in Chemically Derived Graphene Monolayers', *Nano Letters,* 9 (2009), 1787-92.

[85] Zhong-Shuai Wu, Wencai Ren, Libo Gao, Jinping Zhao, Zongping Chen, Bilu Liu, Daiming Tang, Bing Yu, Chuanbin Jiang, and Hui-Ming Cheng, 'Synthesis of Graphene Sheets with High Electrical Conductivity and Good Thermal Stability by Hydrogen Arc Discharge Exfoliation', *ACS Nano,* 3 (2009), 411-17.

[86] Umar Khan, Arlene O'Neill, Mustafa Lotya, Sukanta De, and Jonathan N. Coleman, 'High-Concentration Solvent Exfoliation of Graphene', *Small,* 6 (2010), 864-71.

[87] Arlene O’Neill, Umar Khan, Peter N. Nirmalraj, John Boland, and Jonathan N. Coleman, 'Graphene Dispersion and Exfoliation in Low Boiling Point Solvents', *The Journal of Physical Chemistry C,* 115 (2011), 5422-28.

[88] Aravind Vijayaraghavan, Calogero Sciascia, Simone Dehm, Antonio Lombardo, Alessandro Bonetti, Andrea C. Ferrari, and Ralph Krupke, 'Dielectrophoretic Assembly of High-Density Arrays of Individual Graphene Devices for Rapid Screening', *ACS Nano,* 3 (2009), 1729-34.

[89] Cristina Gómez-Navarro, R. Thomas Weitz, Alexander M. Bittner, Matteo Scolari, Alf Mews, Marko Burghard, and Klaus Kern, 'Electronic Transport Properties of Individual Chemically Reduced Graphene Oxide Sheets', *Nano Letters,* 7 (2007), 3499-503.

[90] R. H. Savage, and D. L. Schaefer, 'Vapor Lubrication of Graphite Sliding Contacts', *Journal of Applied Physics,* 27 (1956), 136-38.

[91] R.D. Arnell, and D.G. Teer, 'Lattice Parameters of Graphite in Relation to Friction and Wear', *Journal Name: Nature (London), 218: 1155-6(June 22, 1968).; Other Information: Orig. Receipt Date: 31-DEC-68; Bib. Info. Source: UK (United Kingdom (sent to DOE from))* (1968), Medium: X

[92] B. K. Yen, B. E. Schwickert, and M. F. Toney, 'Origin of Low-Friction Behavior in Graphite Investigated by Surface X-Ray Diffraction', *Applied Physics Letters,* 84 (2004), 4702-04.

[93] Cristina Gómez-Navarro, R. Thomas Weitz, Alexander M. Bittner, Matteo Scolari, Alf Mews, Marko Burghard, and Klaus Kern, 'Electronic Transport Properties of Individual Chemically Reduced Graphene Oxide Sheets', *Nano Letters,* 9 (2009), 2206-06.

[94] Yu-Ming Lin, and Phaedon Avouris, 'Strong Suppression of Electrical Noise in Bilayer Graphene Nanodevices', *Nano Letters,* 8 (2008), 2119-25.

[95] Chenguang Lu, Qiang Fu, Shaoming Huang, and Jie Liu, 'Polymer Electrolyte-Gated Carbon Nanotube Field-Effect Transistor', *Nano Letters,* 4 (2004), 623-27.

[96] A. Pachoud, M. Jaiswal, P. K. Ang, K. P. Loh, and B. Özyilmaz, 'Graphene Transport at High Carrier Densities Using a Polymer Electrolyte Gate', *EPL (Europhysics Letters),* 92 (2010), 27001.

[97] S. Kim, J. Nah, I. Jo, D. Shahrjerdi, L. Colombo, Z. Yao, E. Tutuc, and S. K. Banerjee, 'Realization of a High Mobility Dual-Gated Graphene Field-Effect Transistor with Al_2O_3 Dielectric', *Applied Physics Letters,* 94 (2009).

[98] E. H. Hwang, S. Adam, and S. Das Sarma, 'Carrier Transport in Two-Dimensional Graphene Layers', *Physical Review Letters,* 98 (2007), 186806.

[99] J. H. Chen, C. Jang, S. Xiao, M. Ishigami, and M. S. Fuhrer, 'Intrinsic and Extrinsic Performance Limits of Graphene Devices on SiO_2', *Nature Nanotechnology,* 3 (2008), 206-09.

[100] A. Das, S. Pisana, B. Chakraborty, S. Piscanec, S. K. Saha, U. V. Waghmare, K. S. Novoselov, H. R. Krishnamurthy, A. K. Geim, A. C. Ferrari, and A. K. Sood, 'Monitoring Dopants by Raman Scattering in an Electrochemically Top-Gated Graphene Transistor', *Nature Nanotechnology,* 3 (2008), 210-15.

[101] Fang Chen, Jilin Xia, and Nongjian Tao, 'Ionic Screening of Charged-Impurity Scattering in Graphene', *Nano Letters,* 9 (2009), 1621-25.

[102] C. R. Dean, A. F. Young, I. Meric, C. Lee, L. Wang, S. Sorgenfrei, K. Watanabe, T. Taniguchi, P. Kim, K. L. Shepard, and J. Hone, 'Boron Nitride Substrates for High-Quality Graphene Electronics', *Nature Nanotechnology,* 5 (2010), 722-26.

[103] Youngki Yoon, Kartik Ganapathi, and Sayeef Salahuddin, 'How Good Can Monolayer MoS_2 Transistors Be?', *Nano Letters,* 11 (2011), 3768-73.

[104] K. S. Novoselov, D. Jiang, F. Schedin, T. J. Booth, V. V. Khotkevich, S. V. Morozov, and A. K. Geim, 'Two-Dimensional Atomic Crystals', *Proceedings of the National Academy of Sciences of the United States of America,* 102 (2005), 10451-53.

[105] Subhamoy Ghatak, Atindra Nath Pal, and Arindam Ghosh, 'Nature of Electronic States in Atomically Thin MoS_2 Field-Effect Transistors', *ACS Nano,* 5 (2011), 7707-12.

[106] Hai Li, Zongyou Yin, Qiyuan He, Hong Li, Xiao Huang, Gang Lu, Derrick Wen Hui Fam, Alfred Iing Yoong Tok, Qing Zhang, and Hua Zhang, 'Fabrication of Single- and Multilayer MoS_2 Film-Based Field-Effect Transistors for Sensing No at Room Temperature', *Small,* 8 (2012), 63-67.

[107] R. Fivaz, and E. Mooser, 'Mobility of Charge Carriers in Semiconducting Layer Structures', *Physical Review,* 163 (1967), 743-55.

[108] B. Radisavljevic, A. Radenovic, J. Brivio, V. Giacometti, and A. Kis, 'Single-Layer MoS_2 Transistors', *Nature Nanotechnology,* 6 (2011), 147-50.

[109] Kangho Lee, Hye-Young Kim, Mustafa Lotya, Jonathan N. Coleman, Gyu-Tae Kim, and Georg S. Duesberg, 'Electrical Characteristics of Molybdenum Disulfide Flakes Produced by Liquid Exfoliation', *Advanced Materials,* 23 (2011), 4178-82.

[110] Shuai Wang, Priscilla Kailian Ang, Ziqian Wang, Ai Ling Lena Tang, John T. L. Thong, and Kian Ping Loh, 'High Mobility, Printable, and Solution-Processed Graphene Electronics', *Nano Letters,* 10 (2009), 92-98.

[111] Changgu Lee, Hugen Yan, Louis E. Brus, Tony F. Heinz, James Hone, and Sunmin Ryu, 'Anomalous Lattice Vibrations of Single- and Few-Layer MoS_2', *ACS Nano,* 4 (2010), 2695-700.

[112] A. Pachoud, M. Jaiswal, P. K. Ang, K. P. Loh, and B. Özyilmaz, 'Graphene Transport at High Carrier Densities Using a Polymer Electrolyte Gate', *EPL,* 92 (2010), 27001.

[113] Zongyou Yin, Hai Li, Hong Li, Lin Jiang, Yumeng Shi, Yinghui Sun, Gang Lu, Qing Zhang, Xiaodong Chen, and Hua Zhang, 'Single-Layer MoS_2 Phototransistors', *ACS Nano,* 6 (2011), 74-80.

[114] Jun Yan, and Michael S. Fuhrer, 'Correlated Charged Impurity Scattering in Graphene', *Physical Review Letters,* 107 (2011), 206601.

[115] Liu Han, and P. D. Ye, 'MoS2 Dual-Gate MOSFET with Atomic-Layer-Deposited Al_2O_3 as Top-Gate Dielectric', *Electron Device Letters, IEEE,* 33 (2012), 546-48.

[116] B. K. Kim, J. J. Kim, H. M. So, K. J. Kong, H. Chang, J. O. Lee, and N. Park, 'Carbon Nanotube Diode Fabricated by Contact Engineering with Self-Assembled Molecules', *Applied Physics Letters,* 89 (2006).

[117] J. L. Xia, F. Chen, P. Wiktor, D. K. Ferry, and N. J. Tao, 'Effect of Top Dielectric Medium on Gate Capacitance of Graphene Field Effect Transistors: Implications in Mobility Measurements and Sensor Applications', *Nano Letters,* 10 (2010), 5060-64.

[118] Fang Chen, Jilin Xia, David K. Ferry, and Nongjian Tao, 'Dielectric Screening Enhanced Performance in Graphene FET', *Nano Letters,* 9 (2009), 2571-74.

[119] Jérôme Lambert, Grégoire de Loubens, Claudine Guthmann, Michel Saint-Jean, and Thierry Mélin, 'Dispersive Charge Transport Along the Surface of an Insulating Layer Observed by Electrostatic Force Microscopy', *Physical Review B,* 71 (2005), 155418.

[120] Giles P. Siddons, David Merchin, Ju Hee Back, Jae Kyeong Jeong, and Moonsub Shim, 'Highly Efficient Gating and Doping of Carbon Nanotubes with Polymer Electrolytes', *Nano Letters,* 4 (2004), 927-31.

[121] Kin Fai Mak, Changgu Lee, James Hone, Jie Shan, and Tony F. Heinz, 'Atomically Thin MoS_2: A New Direct-Gap Semiconductor', *Physical Review Letters,* 105 (2010), 136805.

[122] E. Gourmelon, O. Lignier, H. Hadouda, G. Couturier, J. C. Bernède, J. Tedd, J. Pouzet, and J. Salardenne, 'MS_2 (M = W, Mo) Photosensitive Thin Films for Solar Cells', *Solar Energy Materials and Solar Cells,* 46 (1997), 115-21.

[123] Xu Zong, Hongjian Yan, Guopeng Wu, Guijun Ma, Fuyu Wen, Lu Wang, and Can Li, 'Enhancement of Photocatalytic H_2 Evolution on Cds by Loading MoS_2 as Cocatalyst under Visible Light Irradiation', *Journal of the American Chemical Society,* 130 (2008), 7176-77.

[124] T. Takahashi, T. Takenobu, J. Takeya, and Y. Iwasa, 'Ambipolar Light-Emitting Transistors of a Tetracene Single Crystal', *Advanced Functional Materials,* 17 (2007), 1623-28.

[125] Yijin Zhang, Jianting Ye, Yusuke Matsuhashi, and Yoshihiro Iwasa, 'Ambipolar MoS_2 Thin Flake Transistors', *Nano Letters,* 12 (2012), 1136-40.

[126] J. Takeya, K. Yamada, K. Hara, K. Shigeto, K. Tsukagoshi, S. Ikehata, and Y. Aoyagi, 'High-Density Electrostatic Carrier Doping in Organic Single-Crystal Transistors with Polymer Gel Electrolyte', *Applied Physics Letters,* 88 (2006).

[127] Hongtao Yuan, Hidekazu Shimotani, Atsushi Tsukazaki, Akira Ohtomo, Masashi Kawasaki, and Yoshihiro Iwasa, 'Hydrogenation-Induced Surface Polarity Recognition and Proton Memory Behavior at Protic-Ionic-Liquid/Oxide Electric-Double-Layer Interfaces', *Journal of the American Chemical Society,* 132 (2010), 6672-78.

[128] Taner Ozel, Anshu Gaur, John A. Rogers, and Moonsub Shim, 'Polymer Electrolyte Gating of Carbon Nanotube Network Transistors', *Nano Letters,* 5 (2005), 905-11.

[129] W. Regan, N. Alem, B. Alemán, B. Geng, Ç Girit, L. Maserati, F. Wang, M. Crommie, and A. Zettl, 'A Direct Transfer of Layer-Area Graphene', *Applied Physics Letters,* 96 (2010).

[130] Alfonso Reina, Hyungbin Son, Liying Jiao, Ben Fan, Mildred S. Dresselhaus, ZhongFan Liu, and Jing Kong, 'Transferring and Identification of Single- and Few-Layer Graphene on Arbitrary Substrates', *The Journal of Physical Chemistry C,* 112 (2008), 17741-44.

[131] J. C. Meyer, A. K. Geim, M. I. Katsnelson, K. S. Novoselov, T. J. Booth, and S. Roth, 'The Structure of Suspended Graphene Sheets', *Nature,* 446 (2007), 60-63.

[132] Xinran Wang, Xiaolin Li, Li Zhang, Youngki Yoon, Peter K. Weber, Hailiang Wang, Jing Guo, and Hongjie Dai, 'N-Doping of Graphene through Electrothermal Reactions with Ammonia', *Science,* 324 (2009), 768-71.

[133] N. Tombros, C. Jozsa, M. Popinciuc, H. T. Jonkman, and B. J. Van Wees, 'Electronic Spin Transport and Spin Precession in Single Graphene Layers at Room Temperature', *Nature,* 448 (2007), 571-74.

[134] S. Cho, Y. F. Chen, and M. S. Fuhrer, 'Gate-Tunable Graphene Spin Valve', *Applied Physics Letters,* 91 (2007).

[135] F. Schedin, A. K. Geim, S. V. Morozov, E. W. Hill, P. Blake, M. I. Katsnelson, and K. S. Novoselov, 'Detection of Individual Gas Molecules Adsorbed on Graphene', *Nature Materials,* 6 (2007), 652-55.

[136] Yasuhide Ohno, Kenzo Maehashi, Yusuke Yamashiro, and Kazuhiko Matsumoto, 'Electrolyte-Gated Graphene Field-Effect Transistors for Detecting Ph and Protein Adsorption', *Nano Letters,* 9 (2009), 3318-22.

[137] Zengguang Cheng, Qiang Li, Zhongjun Li, Qiaoyu Zhou, and Ying Fang, 'Suspended Graphene Sensors with Improved Signal and Reduced Noise', *Nano Letters,* 10 (2010), 1864-68.

[138] Tzahi Cohen-Karni, Quan Qing, Qiang Li, Ying Fang, and Charles M. Lieber, 'Graphene and Nanowire Transistors for Cellular Interfaces and Electrical Recording', *Nano Letters,* 10 (2010), 1098-102.

[139] J. Scott Bunch, Arend M. van der Zande, Scott S. Verbridge, Ian W. Frank, David M. Tanenbaum, Jeevak M. Parpia, Harold G. Craighead, and Paul L. McEuen, 'Electromechanical Resonators from Graphene Sheets', *Science,* 315 (2007), 490-93.

[140] Meryl D. Stoller, Sungjin Park, Yanwu Zhu, Jinho An, and Rodney S. Ruoff, 'Graphene-Based Ultracapacitors', *Nano Letters,* 8 (2008), 3498-502.

[141] A. F. Young, and P. Kim, 'Quantum Interference and Klein Tunnelling in Graphene Heterojunctions', *Nature Physics,* 5 (2009), 222-26.

[142] Y. Zhang, V. W. Brar, F. Wang, C. Girit, Y. Yayon, M. Panlasigui, A. Zettl, and M. F. Crommie, 'Giant Phonon-Induced Conductance in Scanning Tunnelling Spectroscopy of Gate-Tunable Graphene', *Nature Physics,* 4 (2008), 627-30.

[143] J. Martin, N. Akerman, G. Ulbricht, T. Lohmann, J. H. Smet, K. Von Klitzing, and A. Yacoby, 'Observation of Electron-Hole Puddles in Graphene Using a Scanning Single-Electron Transistor', *Nature Physics,* 4 (2008), 144-48.

[144] S. Y. Zhou, G. H. Gweon, A. V. Fedorov, P. N. First, W. A. De Heer, D. H. Lee, F. Guinea, A. H. Castro Neto, and A. Lanzara, 'Substrate-Induced Bandgap Opening in Epitaxial Graphene', *Nature Materials,* 6 (2007), 770-75.

[145] E. H. Hwang, S. Adam, and S. Das Sarma, 'Carrier Transport in Two-Dimensional Graphene Layers', *Physical Review Letters,* 98 (2007), 186806.

[146] K. S. Novoselov, Z. Jiang, Y. Zhang, S. V. Morozov, H. L. Stormer, U. Zeitler, J. C. Maan, G. S. Boebinger, P. Kim, and A. K. Geim, 'Room-Temperature Quantum Hall Effect in Graphene', *Science,* 315 (2007), 1379.

[147] David L. Miller, Kevin D. Kubista, Gregory M. Rutter, Ming Ruan, Walt A. de Heer, Phillip N. First, and Joseph A. Stroscio, 'Observing the Quantization of Zero Mass Carriers in Graphene', *Science,* 324 (2009), 924-27.

[148] K. I. Bolotin, F. Ghahari, M. D. Shulman, H. L. Stormer, and P. Kim, 'Observation of the Fractional Quantum Hall Effect in Graphene', *Nature,* 462 (2009), 196-99.

[149] X. Du, I. Skachko, F. Duerr, A. Luican, and E. Y. Andrei, 'Fractional Quantum Hall Effect and Insulating Phase of Dirac Electrons in Graphene', *Nature,* 462 (2009), 192-95.

[150] T. Dürkop, S. A. Getty, Enrique Cobas, and M. S. Fuhrer, 'Extraordinary Mobility in Semiconducting Carbon Nanotubes', *Nano Letters,* 4 (2003), 35-39.

[151] Benjamin Krauss, Péter Nemes-Incze, Viera Skakalova, László P. Biro, Klaus von Klitzing, and Jurgen H. Smet, 'Raman Scattering at Pure Graphene Zigzag Edges', *Nano Letters,* 10 (2010), 4544-48.

[152] J. Bai, X. Zhong, S. Jiang, Y. Huang, and X. Duan, 'Graphene Nanomesh', *Nature Nanotechnology,* 5 (2010), 190-94.

[153] W. Regan, N. Alem, B. Alemán, B. Geng, Ç Girit, L. Maserati, F. Wang, M. Crommie, and A. Zettl, 'A Direct Transfer of Layer-Area Graphene', *Applied Physics Letters,* 96 (2010).

[154] J. C. Meyer, A. K. Geim, M. I. Katsnelson, K. S. Novoselov, T. J. Booth, and S. Roth, 'The Structure of Suspended Graphene Sheets', *Nature,* 446 (2007), 60-63.

[155] T. H. Kim, Z. Wang, J. F. Wendelken, H. H. Weitering, W. Li, and A. P. Li, 'A Cryogenic Quadraprobe Scanning Tunneling Microscope System with Fabrication Capability for Nanotransport Research', *Review of Scientific Instruments,* 78 (2007).

[156] Yousuke Kobayashi, Koichi Kusakabe, Ken-ichi Fukui, and Toshiaki Enoki, 'STM/STS Observation of Peculiar Electronic States at Graphite Edges', *Physica E: Low-dimensional Systems and Nanostructures,* 34 (2006), 678-81.

[157] Masa Ishigami, J. H. Chen, W. G. Cullen, M. S. Fuhrer, and E. D. Williams, 'Atomic Structure of Graphene on SiO_2', *Nano Letters,* 7 (2007), 1643-48.

[158] Y. W. Son, M. L. Cohen, and S. G. Louie, 'Half-Metallic Graphene Nanoribbons', *Nature,* 444 (2006), 347-49.

[159] W. Y. Kim, and K. S. Kim, 'Prediction of Very Large Values of Magnetoresistance in a Graphene Nanoribbon Device', *Nature Nanotechnology,* 3 (2008), 408-12.

ABSTRACT

THE ELECTRICAL TRANSPORT STUDY OF GRAPHENE NANORIBBONS AND 2D MATERIALS BEYOND GRAPHENE

by

MING-WEI LIN

December 2012

Advisor: Dr. Zhixian Zhou

Major: Physics

Degree: Doctor of Philosophy

The electrical transport measurements on a suspended ultra-low-disorder graphene nanoribbon (GNR) with nearly atomically smooth edges that reveal a high mobility exceeding 3000 cm^2 V^{-1} s^{-1} and an intrinsic bandgap was reported in this study. The experimentally derived bandgap is in *quantitative* agreement with the results of our electronic-structure calculations on chiral GNRs with comparable width taking into account the electron-electron interactions, indicating that the origin of the bandgap in non-armchair GNRs is partially due to the magnetic zigzag edges. In addition, electrical transport measurements show that current-annealing effectively removes the impurities on the suspended graphene nanoribbons, uncovering the intrinsic ambipolar transfer characteristic of graphene. Further increasing the annealing current creates a narrow constriction in the ribbon, leading to the formation of a large band-gap and subsequent high on/off ratio (which can exceed 10^4). This work shows for the first time that

ambipolar field effect characteristics and high on/off ratios at room temperature can be achieved in relatively wide graphene nanoribbon (15 nm ~50 nm) by controlled current annealing.

Moreover, a simple one-stage solution-based method was developed to produce graphene nanoribbons by sonicating graphite powder in organic solutions with polymer surfactant. Single-layer and few-layer graphene nanoribbons with a width ranging from sub-10 nm to tens of nm and length ranging from hundreds of nm to 1 μm were routinely observed. Electrical transport properties of individual graphene nanoribbons were measured in both the back-gate and polymer-electrolyte top-gate configurations. The mobility of the graphene nanoribbons was found to be over an order of magnitude higher when measured in the latter than in the former configuration (without the polymer electrolyte), which can be attributed to the screening of the charged impurities by the counter-ions in the polymer electrolyte. This finding suggests that the charge transport in these solution-produced graphene nanoribbons is largely limited by charged impurity scattering.

We also report electrical characterization of monolayer molybdenum disulfide (MoS_2) devices using a thin layer of polymer electrolyte consisting of poly (ethylene oxide) (PEO) and lithium perchlorate ($LiClO_4$) as both a contact-barrier reducer and channel mobility booster. We find that bare MoS_2 devices (without polymer electrolyte) fabricated on Si/SiO_2 have low channel mobility and large contact resistance, both of which severely limit the field-effect mobility of the devices. A thin layer of PEO/ $LiClO_4$ deposited on top of the devices not only substantially reduces the contact resistance but also boost the channel mobility, leading up to three-orders-of-magnitude enhancement of the field-effect mobility of the device. When the polymer electrolyte is used as a gate medium, the MoS_2 field-effect transistors exhibit excellent

device characteristics such as a near ideal subthreshold swing and an on/off ratio of 10^6 as a result of the strong gate-channel coupling. In addition, the ambipolar field-effect transistors of atomically thin MoS_2 with an ionic liquid gate were realized in this study. A record high On-Off current ratio greater than 10^6 is achieved for hole transport in a bilayer MoS_2 transistor, while that for electron transport exceeds 10^7. The scaled transconductance of the device reaches 11.8 μS/μm at a drain-source voltage of 1V, which is an order of magnitude large than that observed in MoS_2 transistors with a high-κ top-gate dielectric. A near ideal subthreshold swing of 47mV/dec at 230 K is also achieved in the bilayer MoS_2 device.

AUTOBIOGRAPHICAL STATEMENT

MING-WEI LIN

Education:

2009~2012 Ph.D. Wayne State University, Detroit, Michigan

1993~1995 M.A. State University of New York at Buffalo, Buffalo, New York

1982~1987 B.S. National Kaohsiung Normal University, Kaohsiung, Taiwan

Honor/Award:

- The best posters awards in AVS meeting, May 2011.
- Knoller Endowment Scholarship, 2012.

Presentation:

→APS March Meeting 2011, Dallas, Texas

Lin, M. W.; Ling, C.; Agapito, L. A.; Kioussis, N.; Zhang, Y.Y.; Cheng, M. M. C.; Wang, W. L.; Kaxiras, E. and Zhou, Z. X.; "Approaching the intrinsic bandgap in suspended high-mobility graphene nanoribbons".

→APS March Meeting 2012, Boston, Massachusetts

Lin, M. W.; Agapito, L. A.; Kioussis, N.; Dhindsa, S. K.; Liu, L. Z.; Lan, Q.; Cheng, M. M. C.; Wang, W. L.; Kaxiras, E. and Zhou, Z. X.; "The electrical transport study of suspended graphene nanoribbons".

Selected publications:

[1] ***Lin, M. W.***; Liu, L. Z.; Lan, Q.; Tan, X. B.; Dhindsa, K. S.; Zeng, P.; Naik, V. M.; Cheng, M. M. C.; Zhou, Z. X.; "Mobility enhancement and highly efficient gating of monolayer MoS_2 transistors with polymer electrolyte", ***J. of Phys. D: Appl. Phys.*** 45, 345102, 2012.
[2] ***Lin, M. W.***; Ling, C.; Agapito, L. A.; Kioussis, N.; Zhang, Y.Y.; Cheng, M. M. C.; Wang, W. L.; Kaxiras, E. and Zhou, Z. X.; "Approaching the intrinsic bandgap in suspended high-mobility graphene nanoribbons", ***Phys. Rev. B*** 84, 125411, 2011.
[3] ***Lin, M. W.;*** Ling, C.; Zhang, Y. Y.; Yoon, H. J.; Cheng, M. M. C.; Agapito, L. A.; Kioussis, N.; Widjaja, N. and Zhou, Z. X.; "Room-temperature high on*/off ratio in* suspended graphene nanoribbon field-effect transistors", ***Nanotechnology*** 22, 265201, 2011.
[4] Ling, C.; Setzler, G.; ***Lin, M. W.;*** Dhindsa, K. S.; Jin, J.; Yoon, H. J.; Kim, S. S.; Cheng, M. M. C.; Widjaja, N. and Zhou, Z. X.; "Electrical transport properties of graphene nanoribbons produced from sonicating graphite in solution", ***Nanotechnology*** 22, 325201, 2011.